



**NAVAL  
POSTGRADUATE  
SCHOOL**

**MONTEREY, CALIFORNIA**

**THESIS**

**THE POTENTIAL OBSERVATION NETWORK DESIGN  
WITH MESOSCALE ENSEMBLE SENSITIVITIES  
IN COMPLEX TERRAIN**

by

Kenneth H. Chilcoat

March 2012

Thesis Advisor:

Second Reader:

Joshua P. Hacker

James D. Doyle

**Approved for public release; distribution is unlimited**

THIS PAGE INTENTIONALLY LEFT BLANK

**REPORT DOCUMENTATION PAGE**
*Form Approved OMB No. 0704-0188*

Public reporting burden for this collection of information is estimated to average 1 hour per response, including the time for reviewing instruction, searching existing data sources, gathering and maintaining the data needed, and completing and reviewing the collection of information. Send comments regarding this burden estimate or any other aspect of this collection of information, including suggestions for reducing this burden, to Washington Headquarters Services, Directorate for Information Operations and Reports, 1215 Jefferson Davis Highway, Suite 1204, Arlington, VA 22202-4302, and to the Office of Management and Budget, Paperwork Reduction Project (0704-0188) Washington DC 20503.

<b>1. AGENCY USE ONLY (Leave blank)</b>	<b>2. REPORT DATE</b> March 2012	<b>3. REPORT TYPE AND DATES COVERED</b> Master's Thesis
<b>4. TITLE AND SUBTITLE</b> The Potential Observation Network Design with Mesoscale Ensemble Sensitivities in Complex Terrain		<b>5. FUNDING NUMBERS</b>
<b>6. AUTHOR(S)</b> Kenneth H. Chilcoat		
<b>7. PERFORMING ORGANIZATION NAME(S) AND ADDRESS(ES)</b> Naval Postgraduate School Monterey, CA 93943-5000		<b>8. PERFORMING ORGANIZATION REPORT NUMBER</b>
<b>9. SPONSORING /MONITORING AGENCY NAME(S) AND ADDRESS(ES)</b> N/A		<b>10. SPONSORING/MONITORING AGENCY REPORT NUMBER</b>
<b>11. SUPPLEMENTARY NOTES</b> The views expressed in this thesis are those of the author and do not reflect the official policy or position of the Department of Defense or the U.S. Government. IRB Protocol number _____ N/A _____.		
<b>12a. DISTRIBUTION / AVAILABILITY STATEMENT</b> Approved for public release; distribution is unlimited		<b>12b. DISTRIBUTION CODE</b>

**13. ABSTRACT (maximum 200 words)**

Observation network design requires some framework for sensitivity studies. The goal is to place observations where they will reduce forecast error the most. We use uncertainty estimates from our best forecast models as an indicator of forecast error. The first step is then to find initial-state perturbations that reduce forecast uncertainty by minimizing a user-dependent norm. Adjoint models have helped meet this challenge for decades. More recently, ensemble sensitivities have emerged as a powerful alternative to adjoint models. Under the conditions of Gaussian statistics and an infinite ensemble, lagged covariances from an ensemble can be used equivalently to an adjoint model to give the least-squares minimization of a given cost function. One practical advantage is that costly development and maintenance of tangent linear and adjoint models are avoided. Ensemble sensitivities have been shown to be an effective alternative to adjoint models. They have been used successfully to diagnose predictors of forecast error in synoptic storms, extratropical transition and developing hurricanes. Because they rely on lagged covariances from a finite-sized ensemble, they are subject to sampling error and spurious covariances. However, their efficacy for high-resolution forecasts in mountainous environments has not been thoroughly explored. We present results from experiments designed to establish the potential for ensemble sensitivity computations with a high resolution mesoscale model (grid spacing 4 km) in complex terrain. Using the Weather Research and Forecast (WRF) model and the Data Assimilation Research Testbed (DART) we compute sensitivities with cost functions defined to emphasize parameters affecting fog forecasting in the boundary layer. High sensitivities are interpreted as indicating low predictability for forecasting in the mountains. Results from convergence studies reveal the ensemble sizes needed to robustly estimate the sensitivities. We comment on the implications of results for observation placement and on the expected impact of model inadequacy.

<b>14. SUBJECT TERMS</b> Mesoscale Ensemble Sensitivity Analysis, Ensemble Sensitivities, Mesoscale Forecast Sensitivities, Observation Network Design, ESA		<b>15. NUMBER OF PAGES</b> 103
<b>16. PRICE CODE</b>		
<b>17. SECURITY CLASSIFICATION OF REPORT</b> Unclassified	<b>18. SECURITY CLASSIFICATION OF THIS PAGE</b> Unclassified	<b>19. SECURITY CLASSIFICATION OF ABSTRACT</b> Unclassified
		<b>20. LIMITATION OF ABSTRACT</b> UU

THIS PAGE INTENTIONALLY LEFT BLANK

**Approved for public release; distribution is unlimited**

**THE POTENTIAL OBSERVATION NETWORK DESIGN WITH MESOSCALE  
ENSEMBLE SENSITIVITIES IN COMPLEX TERRAIN**

Kenneth H. Chilcoat  
Captain, United States Air Force  
B.S., Pennsylvania State University, 2003

Submitted in partial fulfillment of the  
requirements for the degree of

**MASTER OF SCIENCE IN METEOROLOGY**

from the

**NAVAL POSTGRADUATE SCHOOL**  
**March 2012**

Author: Kenneth H. Chilcoat

Approved by: Joshua P. Hacker  
Thesis Advisor

James D. Doyle  
Second Reader

Wendell Nuss  
Chair, Department of Meteorology

THIS PAGE INTENTIONALLY LEFT BLANK

## ABSTRACT

Observation network design requires some framework for sensitivity studies. The goal is to place observations where they will reduce forecast error the most. We use uncertainty estimates from our best forecast models as an indicator of forecast error. The first step is then to find initial-state perturbations that reduce forecast uncertainty by minimizing a user-dependent norm. Adjoint models have helped meet this challenge for decades. More recently, ensemble sensitivities have emerged as a powerful alternative to adjoint models. Under the conditions of Gaussian statistics and an infinite ensemble, lagged covariances from an ensemble can be used equivalently to an adjoint model to give the least-squares minimization of a given cost function. One practical advantage is that costly development and maintenance of tangent linear and adjoint models are avoided. Ensemble sensitivities have been shown to be an effective alternative to adjoint models. They have been used successfully to diagnose predictors of forecast error in synoptic storms, extratropical transition and developing hurricanes. Because they rely on lagged covariances from a finite-sized ensemble, they are subject to sampling error and spurious covariances. However, their efficacy for high-resolution forecasts in mountainous environments has not been thoroughly explored. We present results from experiments designed to establish the potential for ensemble sensitivity computations with a high resolution mesoscale model (grid spacing 4 km) in complex terrain. Using the Weather Research and Forecast (WRF) model and the Data Assimilation Research Testbed (DART) we compute sensitivities with cost functions defined to emphasize parameters affecting fog forecasting in the boundary layer. High sensitivities are interpreted as indicating low predictability for forecasting in the mountains. Results from convergence studies reveal the ensemble sizes needed to robustly estimate the sensitivities. We comment on the implications of results for observation placement and on the expected impact of model inadequacy.

THIS PAGE INTENTIONALLY LEFT BLANK

## TABLE OF CONTENTS

I.	INTRODUCTION.....	1
A.	MOTIVATION .....	1
B.	PROBLEM STATEMENT .....	3
C.	RESEARCH OBJECTIVES .....	4
II.	BACKGROUND .....	7
A.	FORECAST SENSITIVITY .....	7
B.	ADJOINT SENSITIVITY .....	7
C.	ENSEMBLE SENSITIVITY .....	8
III.	DATA AND METHODOLOGY .....	11
A.	ESA CALCULATION.....	11
B.	ADDRESSING STATISTICAL SAMPLING ERROR .....	12
C.	MODEL SETUP.....	13
1.	Nesting Configuration .....	13
2.	Vertical Coordinate System .....	15
3.	Physics .....	16
4.	Data Assimilation Process .....	17
D.	OVERVIEW: SALT LAKE BASIN, UTAH.....	19
E.	SYNOPTIC SITUATION .....	23
1.	Soundings.....	23
2.	Overview .....	26
3.	Physical Interpretation.....	28
F.	DETERMINISTIC MODEL COMPARISON.....	29
G.	AFWA'S MEPS NON-PRECIPITATION VISIBILITY ALGORITHM.....	29
H.	PARAMETERS.....	30
IV.	RESULTS .....	31
A.	WRF ENSEMBLE PREDICTIONS .....	31
1.	MOISTURE.....	31
2.	WINDS .....	34
B.	CONCEPTUAL MODEL .....	38
C.	QUANTITATIVE ESA RESULTS .....	43
1.	ESA Results .....	44
a.	<i>U-Component Winds</i> .....	44
b.	<i>V-Component Winds</i> .....	46
2.	Wind Shift.....	48
3.	Statistical Linearity.....	49
a.	<i>Nine-Hour Forecast</i> .....	50
b.	<i>Twelve-Hour Forecast</i> .....	51
4.	Linear Correlation.....	52
D.	TESTING THE LINEARITY .....	54

1.	Testing the 1800 UTC 23 January Sensitivity-Analysis Predictions .....	54
2.	Testing the 1500 UTC 23 January Sensitivity-Analysis Predictions .....	60
3.	Sensitivity-Analysis Prediction conclusions.....	63
<b>E.</b>	<b>ENSEMBLE SIZE .....</b>	<b>63</b>
1.	Testing the Positive Sensitivities at a Single Point .....	64
2.	Testing the Negative Sensitivities at a Single Point.....	68
3.	Ensemble Size Summary .....	69
<b>V.</b>	<b>CONCLUSIONS AND FUTURE WORK .....</b>	<b>71</b>
A.	POTENTIAL NETWORK DESIGN .....	73
B.	USEFULNESS TO U.S. MILITARY .....	76
C.	FUTURE WORK.....	77
<b>LIST OF REFERENCES .....</b>		<b>79</b>
<b>INITIAL DISTRIBUTION LIST .....</b>		<b>83</b>

## LIST OF FIGURES

Figure 1.	MEPS 4-km nested grid of the probability of 2-meter visibility $\leq 1$ SM for Afghanistan and surrounding countries (From JAAWIN, <a href="https://weather.afwa.af.mil">https://weather.afwa.af.mil</a> ) .....	3
Figure 2.	Results of the ESA performed by Hakim and Torn (2008) showing that the sensitivity of 24-hr precipitation in a box over western Washington State is most sensitive to changes in SLP in the darkest regions west of the box (From Hakim and Torn 2008).....	9
Figure 3.	Nesting configuration used in the experiments. The outermost grid domain uses 36-km horizontal grid spacing, the middle domain uses 12-km horizontal grid spacing and the innermost domain uses 4-km horizontal grid spacing.....	14
Figure 4.	Innermost grid with 4-km resolution terrain (m). The star represents the SLC Region.....	15
Figure 5.	ARW Vertical coordinate system (From Skamarock et al. 2008). .....	16
Figure 6.	Assimilation Cycling. .....	18
Figure 7.	The WRF ensemble runs used for the project showing how overlapping forecasts can be used to determine how the model changes with a function of lead time. The figure also shows when the low-level wind shift occurred in the model. All runs end at 0600 UTC 24 January 2009 with the main focus on the fog event starting at the airport at 0000 UTC 24 January 2009.....	19
Figure 8.	Image showing the proximity of the GSL and the terrain surrounding the SLC International Airport (After Google Maps, <a href="http://maps.google.com">http://maps.google.com</a> ). ....	20
Figure 9.	Dense fog occurrences as a function of wind direction at SLC International Airport (From Slemmer 2004).....	22
Figure 10.	1200 UTC 23 January 2009 SLC profile showing the strong low-level inversion that was present the morning before the fog event. ....	24
Figure 11.	0000 UTC 24 January 2009 SLC profile showing the inversion had mixed out with the strong diurnal heating that occurred in the afternoon. ....	25
Figure 12.	1200 UTC 24 January 2009 SLC profile from the morning after the fog event showing a strong radiational inversion at the surface. ....	26
Figure 13.	Forecasted 2-meter $Q_v$ at the airport versus actual $Q_v$ from the observations at the airport. The black solid line represents the forecast initialized at 0600 UTC 23 January and the red dashed line represents the forecast initialized at 1800 UTC 23 January. The $Q_v$ recorded at the airport is represented by the blue dashed line. All forecasts end at 0600 UTC 24 January.....	32
Figure 14.	0-24hr EM $Q_v$ for the lowest model level from the ensemble initialized at 0600 UTC 23 January 2009. The brightest yellow colors indicate the highest $Q_v$ values.....	33
Figure 15.	Ensemble u-component winds at SLC international airport at 20 meters. The black solid line represents the forecast initialized at 0600 UTC 23	

January and the red dashed line represents the forecast initialized at 1800 UTC 23 January. All forecasts end at 0600 UTC 24 January.....	35
Figure 16. Ensemble v-component winds at SLC International Airport at 20 meters. The black solid line represents the forecast initialized at 0600 UTC 23 January and the red dashed line represents the forecast initialized at 1800 UTC 23 January. All forecasts end at 0600 UTC 24 January.....	36
Figure 17. Ensemble 10-meter wind direction compared to the actual wind direction at SLC International Airport. The black solid line represents the forecast initialized at 0600 UTC 23 January and the red dashed line represents the forecast initialized at 1800 UTC 23 January. All forecasts end at 0600 UTC 24 January. The blue dashed line represents the actual surface wind direction recorded at the airport.....	37
Figure 18. Ensemble 10-meter wind speed compared to the actual surface wind speed at SLC International Airport. The black solid line represents forecast initialized at 0600 UTC 23 January and the red dashed line represents the forecast initialized at 1800 UTC 23 January. All forecasts end at 0600 UTC 24 January. The blue dashed line represents the actual surface wind speed recorded at the airport.....	37
Figure 19. 1800 UTC 23 January 2009 analysis low-level wind direction at 20 meters. The chart is an EM of analyses for all 96-members. The colors correspond to the wind directions labeled at the bottom of the chart.....	38
Figure 20. Schematic interpretation of the 1800 UTC 23 January low-level wind flow that influenced the advection of moisture off the lake and into the SLC Basin (After Google Maps).....	39
Figure 21. Closer schematic interpretation of the 1800 UTC 23 January low-level wind flow that influenced the advection of moisture off the lake and into the SLC Basin (After Google Maps).....	40
Figure 22. Conceptual sensitivity field using 1800 UTC 23 January 2009 analysis u-component winds as the analysis state variable (x) and $Q_v$ at 0000 UTC 24 January 2009 as the forecast metric (J) for the box centered over the SLC airport (After Google Maps).....	41
Figure 23. Conceptual sensitivity field using 1800 UTC 23 January 2009 analysis v-component winds as the analysis state variable (x) and $Q_v$ at 0000 UTC 24 January 2009 as the forecast metric (J) for the box centered over the SLC International Airport (After Google Maps).....	42
Figure 24. Sensitivities (dJ/dx) using 1800 UTC 23 January u-component analysis winds ( $ms^{-1}$ ) (x) and forecasted $Q_v$ (J) ( $kg\ kg^{-1}$ ) valid at 0000 UTC 24 January. Units are $kg\ kg^{-1}\ per\ m\ s^{-1}$ .....	46
Figure 25. Sensitivities (dJ/dx) using 1800 UTC 23 January v-component analysis winds ( $ms^{-1}$ ) (x) and forecasted $Q_v$ (J) ( $kg\ kg^{-1}$ ) valid at 0000 UTC 24 January. Units are $kg\ kg^{-1}\ per\ m\ s^{-1}$ .....	47
Figure 26. Sensitivities (dJ/dx) using 1500 UTC 23 January u-component analysis winds ( $ms^{-1}$ ) (x) and forecasted $Q_v$ (J) ( $kg\ kg^{-1}$ ) valid at 0000 UTC 24 Jan 2009. Units are $kg\ kg^{-1}\ per\ m\ s^{-1}$ .....	49

Figure 27.	Sensitivities ( $dJ/dx$ ) using 1800 UTC 23 January u-component analysis winds ( $ms^{-1}$ ) (x) and forecasted $Q_v$ (J) ( $kg\ kg^{-1}$ ) valid at 0300 UTC 24 Jan 2009. Units are $kg\ kg^{-1}$ per $m\ s^{-1}$ .....	50
Figure 28.	Sensitivities ( $dJ/dx$ ) using 1800 UTC 23 January u-component analysis winds ( $ms^{-1}$ ) (x) and forecasted $Q_v$ (J) ( $kg\ kg^{-1}$ ) valid at 0300 UTC 24 Jan 2009. Units are $kg\ kg^{-1}$ per $m\ s^{-1}$ .....	51
Figure 29.	Scatterplot of 1800 UTC 23 January analysis u-component winds and forecasted $Q_v$ at the airport at 0000 UTC 24 January .....	53
Figure 30.	Scatterplot of 1800 UTC 23 January analysis u-component winds and forecasted $Q_v$ at the airport at 0300 UTC 24 January .....	53
Figure 31.	Scatterplot of 1800 UTC 23 January analysis u-component winds and forecasted $Q_v$ at the airport at 0600 UTC 24 January .....	54
Figure 32.	The $+1\sigma$ perturbation applied at $41.1^{\circ}N, -112.2^{\circ}E$ at the first $\eta$ -level in $m\ s^{-1}$ after being regressed throughout the model .....	56
Figure 33.	Changes to the u-component wind ( $m\ s^{-1}$ ) throughout the vertical at $41.1^{\circ}N, -112.2^{\circ}E$ after regressing a $+1\sigma$ perturbation at the surface.....	57
Figure 34.	Changes to temperature throughout the vertical at $41.1^{\circ}N, -112.2^{\circ}E$ after regressing a $+1\sigma$ perturbation in the u-component winds at the surface. The profile suggests a strengthened inversion.....	57
Figure 35.	Actual change in $Q_v$ versus predicted change in $Q_v$ for each $\alpha$ -value perturbation using the 1800 UTC 23 January analyses. The line represents a perfectly linear response.....	59
Figure 36.	Plot of actual $Q_v$ from the alpha perturbed ensembles (black line) versus the predicted $Q_v$ taken from the ESA results (dashed line) for 1800 UTC 23 January. Units are $kg\ kg^{-1}$ .....	60
Figure 37.	Actual change in $Q_v$ versus predicted change in $Q_v$ for each $\alpha$ -value perturbation using the 1500 UTC 23 January analyses. The line represents a perfectly linear response. Units are $kg\ kg^{-1}$ .....	62
Figure 38.	Plot of actual $Q_v$ from the alpha perturbed ensembles (black line) versus the predicted $Q_v$ taken from the ESA results (dashed line) for 1500 UTC 23 January. Units are $kg\ kg^{-1}$ .....	62
Figure 39.	Change in 1800 UTC 23 January sensitivities at “X” as the number of ensembles are reduced from 96 to 5 members.....	65
Figure 40.	Scatterplots of analysis u-component winds and forecasted $Q_v$ used in the ESA as the ensemble size is reduced from 96 down to 5 members. The x-axis represents the 1800 UTC 23 January analysis u-component winds at the “X” ( $41.1^{\circ}N, -112.2^{\circ}E$ ) and its associated forecasted $Q_v$ value six hours later valid 0000 UTC 24 January is plotted on the y-axis.....	66
Figure 41.	Chart of correlation in red and sensitivity in blue versus the number of ensemble members for a single point of positive sensitivities at $41.1^{\circ}N, -112.2^{\circ}E$ . The green bars are the high and low boundaries of the 95% confidence interval and represent the associated sampling error.....	67
Figure 42.	Chart of correlation in red and sensitivity in blue versus the number of ensemble members for a single point of negative sensitivities at $41.6^{\circ}N, -$	

113.2°E. The green bars are the high and low boundaries of the 95% confidence interval and represent the associated sampling error.....	68
Figure 43. Locations of the strong sensitivities that are considered important in forecasting the amount of moisture received at the SLC International Airport (After Google Maps, <a href="http://maps.google.com">http://maps.google.com</a> ). .....	75

## LIST OF TABLES

Table 1.	The approximate above ground level (AGL) height for first two $\eta$ -levels.....	16
Table 2.	Physics processes used in the WRF system.....	17
Table 3.	Climatology prepared from OCDS for the SLC International Airport, Manas Air Base, Bagram Air Base and the Kabul Airport.....	23

THIS PAGE INTENTIONALLY LEFT BLANK

## **LIST OF ACRONYMS AND ABBREVIATIONS**

AFWA – Air Force Weather Agency  
CAS – Close Air Support  
DART – Data Assimilation Research Test Bed  
EM – Ensemble Mean  
ESA – Ensemble Sensitivity Analysis  
GFS – Global Forecast System  
GSL – Great Salt Lake  
ISR – Intelligence Surveillance and Reconnaissance  
MEPS – Mesoscale Ensemble Prediction System  
MM5 – Mesoscale Model  
NARR – North America Regional Reanalysis  
NCAR – National Center for Atmospheric Research  
NWP – Numerical Weather Prediction  
OCDS – Operational Climatological Data Sets  
PCAP – Persistent Cold-Air Pool Study  
P-Value – Probability Value  
PWAT – Precipitable Water  
RH – Relative Humidity  
RPA – Remotely Piloted Aircraft  
RUC – Rapid Update Cycle  
SLC – Salt Lake City  
SLP – Sea Level Pressure  
SM – Statute Mile  
USAF – United States Air Force  
WS – Wind Speed

THIS PAGE INTENTIONALLY LEFT BLANK

## ACKNOWLEDGMENTS

I would like to thank my advisor, Dr. Josh Hacker of the Department of Meteorology, Naval Postgraduate School (NPS), for his tireless effort in helping in this project. I am continually amazed by his extensive knowledge in the field and his willingness to teach. I also want to thank my second reader, Dr. Jim Doyle of the Naval Research Laboratory, for taking the time out of his busy schedule to help in the project.

There are also other NPS facility and staff members who helped in this thesis. I want to say thank you to Mr. Bob Creasey for providing me extensive technical support and numerous meteorological explanations. I want to thank Professor Mary Jordan for taking the time to help with the MATLAB coding while teaching me at the same time. I want to say thanks to Maj Paul Homan, United States Air Force, for his widespread help throughout the project and, especially, for his work in the sensitivity-analysis predictions. I also want to thank Maj Bill Ryerson, United States Air Force, for sharing his knowledge of fog forecasting. In addition, I want to thank the entire Department of Meteorology staff, which encompasses of very impressive group of professors who are always willing to assist.

Finally, I want to thank my parents, my sister and all of my classmates for providing positive support through this entire schooling process.

THIS PAGE INTENTIONALLY LEFT BLANK

## I. INTRODUCTION

### A. MOTIVATION

Accurate weather forecasts have always been and will continue to be a key component in successful military operations. U.S. Armed Forces' forecasters and meteorologists rely heavily on numerical prediction models to generate operational forecasts with single deterministic models being the main toolset used. “In Numerical Weather Prediction (NWP) substantial progress has been made through the realization that the chaotic behavior of the atmosphere requires the replacement of single ‘deterministic’ forecast by ‘ensembles’ of forecasts” (Kalnay 2004). Recently, ensemble forecast systems have been introduced into the military’s forecasting structure. The U.S. Air Force (USAF) Weather Agency (AFWA) has been pursuing ensemble technology since 2007 (Hacker et al. 2011) in an effort to produce more accurate and reliable forecasts. Ensemble-based probability products are easily interpreted and can assist inexperienced forecasters in developing useful and meaningful probability forecasts that are briefed to planners and pilots. Global ensembles were the military’s original focus but much effort has been put forth in developing ensemble systems at higher resolution. AFWA’s short-range mesoscale ensemble prediction suite (MEPS) will soon be fully operational and will provide high resolution forecasts for specific operational restraints (fog, dust, winds, turbulence, etc.) in military domains.

U.S. military forces have become increasingly interested in improving weather forecasts in complex terrain, especially with the many recent operations in southwest Asia including Afghanistan. This rugged and mountainous country tests the skill of mesoscale numerical prediction models as over 49 percent of the country lies above 2,000 meters (Afghanistan Environment 2012). Surface and rawinsonde observations are scarce and inconsistent in Afghanistan making data assimilation schemes rely heavily on non-standard observations. This scarcity in data is considered in the design of the ensemble system used in this research.

Military techniques and styles of fighting in these regions frequently evolve as the scope of the war changes with time. In the past two decades, operations have changed from the weather-insensitive strategic bombing using GPS-guided bombs to air operations involving Close Air Support (CAS) and Intelligence Surveillance and Reconnaissance (ISR) missions. CAS and ISR missions are vital to the success of the war but both are highly sensitive to mesoscale weather phenomena in complex terrain including visibility restrictions, precipitation and winds. Remotely piloted vehicles (RPAs) provide both ISR and offensive capabilities and both have become progressively important in the war in Afghanistan. These weather-sensitive platforms have placed a strong emphasis on the accuracy of short-term mesoscale forecasts, especially in areas of complex terrain. Mesoscale ensemble systems have been introduced to mitigate the uncertainty of single deterministic forecasts in these regions and to help produce better operational forecasts. An example of one of the Air Force's MEPs products that will soon be operational to assist forecasters in Afghanistan is seen in Figure 1. Figure 1 represents the probability of 2-meter visibility less than or equal to 1 statute mile (SM) using a 10-member ensemble system with a 4-km nested grid centered over Afghanistan.

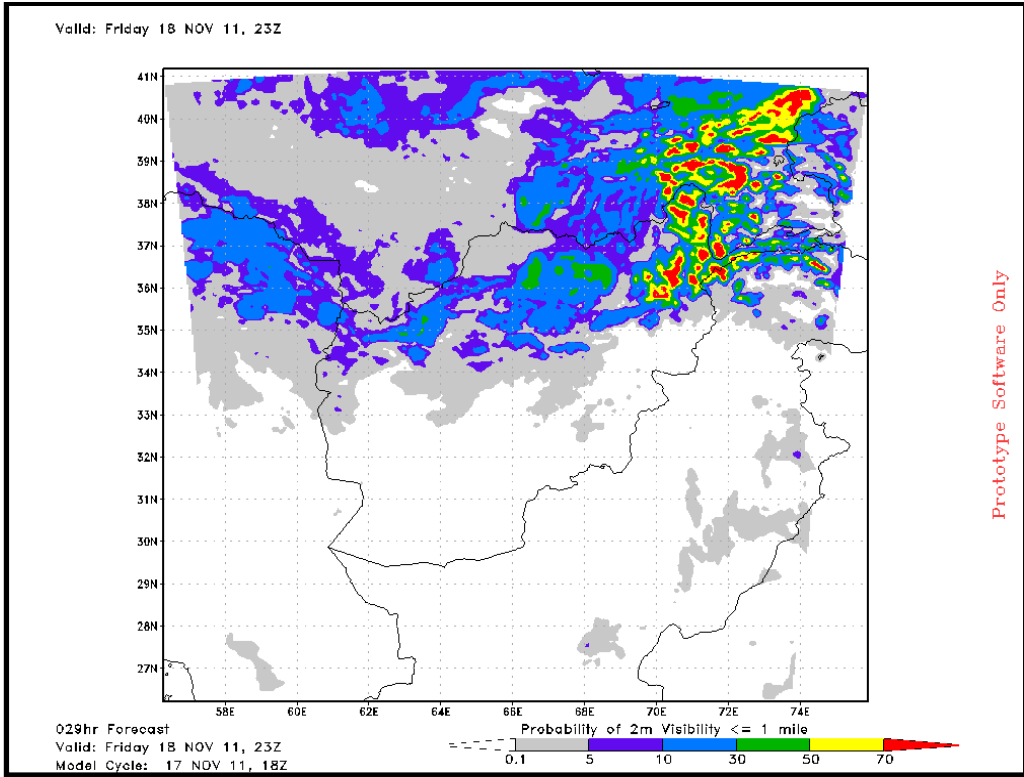


Figure 1. MEPS 4-km nested grid of the probability of 2-meter visibility  $\leq$  1 SM for Afghanistan and surrounding countries (From JAAWIN, <https://weather.afwa.af.mil>)

The primary goal of this thesis work is to better understand mesoscale forecast sensitivities on initial conditions using an ensemble system for a fog event in a region of mountainous terrain. This specific goal fits within the U.S. military's broad goal of improved mesoscale fog predictions in complex terrain. Any improvements in the predictability of forecasting fog will improve the effectiveness of military operations, especially in mountains regions.

## B. PROBLEM STATEMENT

Since 2007, ensemble sensitivities have been shown as an effective alternative to adjoint sensitivities (Ancell and Hakim 2007). More recent studies show that ensemble sensitivities can be used successfully to diagnose predictors of forecast error in synoptic storms (Torn and Hakim 2008), extratropical transition (Torn and Hakim 2009), and developing hurricanes (Torn 2010). These synoptic-scale ensemble sensitivity analyses

(ESAs) used ensemble systems with higher spatial resolution to diagnose the sensitivities of larger-scale synoptic features. However, little attention has been directed at determining the effectiveness of ensemble sensitivity in an environment dominated by mesoscale features, using a high resolution ensemble system. Having the capability to calculate and understand sensitivities in mesoscale environments may lead to the future development of more accurate forecasting and analysis tools to assist military forecasters.

Wintertime fog is common in areas of current military operations in the mountains of southwest Asia including Afghanistan, Pakistan and Kyrgyzstan. Fog commonly causes obstacles with military operations in these regions. Visibility restrictions due to fog and haze are often localized and are difficult to predict, especially in the mountains. After a wintertime deployment in Manas Air Base, Kyrgyzstan, one can easily attest to the difficultly of forecasting fog and how frequently it hinders operations. Fog can quickly develop and advect over Manas Air Base shutting down both flying and ground operations for hours to many days. AFWA has developed a series of ensemble-based forecasting tools to mitigate uncertainty associated with forecasting fog. Current AFWA ensemble-based visibility tools use precipitable water (PWAT), wind speed (WS) and relative humidity (RH) as the key predictors in their visibility algorithms for fog and haze. Applying these parameters in the sensitivity analysis could lead to a better understanding of predictability for forecasting visibility in areas of complex terrain, and could be used in future observation-network design to reduce fog forecasting uncertainty in these regions.

### **C. RESEARCH OBJECTIVES**

The primary objective of the project is to determine if a mesoscale ESA can provide useful data to determine the sensitivity of forecasted fog in complex terrain. The second objective is to determine if the sensitivities calculated could be used to reduce forecast uncertainty for a certain forecast metric, i.e., in future observation network design. Having the ability to estimate the impact the observation has on a certain forecast metric may prove to be useful for thinning observations in NWP analysis systems or to

provide real-time updates to the forecast metric for a certain sensitive location instead of waiting for the complete data assimilation and forecast process (Torn and Hakim 2008).

Some additional pieces needed to establish the viability of the ESA method used include the following:

1. Testing the linear statistics and drawing conclusions based on where and when the ESA breaks down. An objective in testing the statistical linearity is to determine how long the sensitivities can be approximated and when the statistical linearity is no longer valid.
2. Testing the linearity of the sensitivity-analysis predictions determined in the ESA. An objective in testing these linear approximations is to determine the model's inadequacies using the sensitivities calculated while determining if the linearity holds through time and different meteorological conditions.
3. Testing the ESA using a number of different ensemble sizes and drawing conclusions based on these convergence studies. A goal here is to provide a good estimation based on sampling errors on the number of ensemble members needed to produce skillful and robust sensitivities.

Finally, based on the results of the overall study, we provide recommendations on whether the ESA derived from a mesoscale ensemble system is a useful tool for improving mesoscale prediction in complex terrain for areas such as Afghanistan, Pakistan and Kyrgyzstan.

THIS PAGE INTENTIONALLY LEFT BLANK

## II. BACKGROUND

### A. FORECAST SENSITIVITY

Forecast sensitivity can be simply defined as determining how changes to the initial conditions affect the model forecast. The typical goal of sensitivity studies is to determine where to place or remove observations to reduce forecast errors. Since NWP models were first introduced they have been used to determine how impacts of perturbations in the initial conditions can affect forecast error and thus estimate sensitivity. To determine quantitatively the sensitivities of a forecast a mathematical model of the relationships is required (Errico 1997). Physically changing an initial condition in the analysis and determining how it affects the model forecast is the basis of estimating forecast sensitivity. Considered to be the brute force method of forecast sensitivity analysis this method is costly and timely. A more efficient and direct way is to use the model's adjoint (Errico 1997). Adjoint models have met the sensitivity analysis challenge for the past three decades but recently ensemble systems and statistics have been used.

### B. ADJOINT SENSITIVITY

Using the model's adjoint is the primary means of uncovering initial condition sensitivity. An adjoint propagates a model state backward along a tangent linear approximation of a forecast model trajectory. The adjoint and tangent linear models can therefore be used together to minimize a cost function defined by forecast uncertainty. When the adjoint is integrated backward in time it can lead to useful information including forecast sensitivities. Limitations to the adjoint model are mostly due to the approximation of the linear propagator (Errico 1997). Errico described that certain dynamical forecast situations will lead to better linear approximations whereas other situations will break down the approximations more quickly (1997). Overall, it is difficult to determine a general time limit for adjoint applications, but it has been estimated that with NWP models the linearization may remain valid for up to three days for synoptic-scale features (Errico 1997). This linear-approximation time limit could be

much shorter under moist-physics situations and in a mesoscale environment (Errico 1997). Besides the limitations associated with approximations to the linear propagator, another disadvantage to the adjoint method is that developing, maintaining and operating the adjoint can be computationally costly. Even within these limitations, adjoints have in the past successfully identified initial-time perturbations that yield to sensitivities in the forecast.

### C. ENSEMBLE SENSITIVITY

More recently, ensemble sensitivities have emerged as a powerful alternative to adjoint models (Ancell and Hakim 2007). Ensemble sensitivities were first proposed by Hakim and Torn (2008) when they performed an ensemble synoptic analysis using linear relationships and Gaussian statistics to an extratropical cyclone. Essentially, ensemble sensitivity is computed by linear regression of the analysis errors onto a given forecast metric (Ancell and Hakim 2007).

An ESA was formally tested and documented by Hakim and Torn (2008), who examined the linear relationship between forecast parameters of an extratropical cyclone off the West Coast and the initial state variables. Their goals were to (1) determine and illustrate how ensemble sensitivity can be easily used to determine climatological sensitivity for a particular forecast metric and (2) to test the accuracy of the ensemble sensitivity predictions of the impact of observations on a forecast metric (Hakim and Torn 2008). They found the climatological 24-hr sensitivity of the average surface pressure and precipitation over western Washington was most sensitive to changes in analysis sea-level pressure (SLP) in the regions west out over the ocean, gently tilting with height. Figure 2, an example of their results, is the sensitivity of 24-hr precipitation in a box in western Washington to analysis SLP throughout the domain. The darkest regions to the west of the box are the areas of maximum sensitivity.

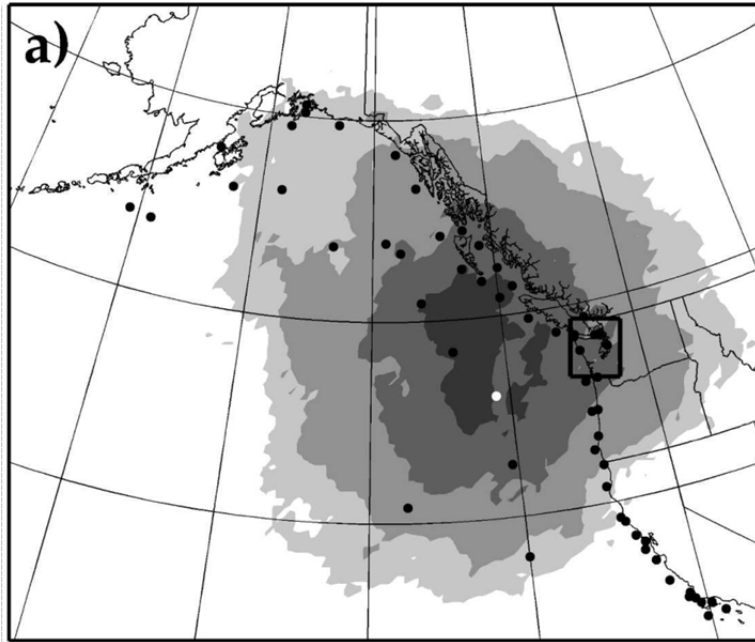


Figure 2. Results of the ESA performed by Hakim and Torn (2008) showing that the sensitivity of 24-hr precipitation in a box over western Washington State is most sensitive to changes in SLP in the darkest regions west of the box (From Hakim and Torn 2008).

The effectiveness and usefulness of ensemble-based sensitivity analyses are still being explored especially as operational ensemble systems are becoming increasingly popular. Ancell and Hakim (2007) determined that ensemble sensitivities are comparable to adjoint sensitivities in synoptic wintertime flow, and that an ESA offers a straightforward and inexpensive approach to sensitivity analysis, observation targeting and observation thinning. ESAs have been used successfully to diagnose predictors of forecast error in synoptic storms (Hakim and Torn 2008), extratropical transition (Torn and Hakim 2009), and developing hurricanes (Torn 2010). However, their effectiveness for high-resolution mesoscale forecasts in complex terrain has not been thoroughly explored and is the driving purpose behind this research.

THIS PAGE INENTIONALLY LEFT BLANK

### III. DATA AND METHODOLOGY

#### A. ESA CALCULATION

The ensemble sensitivity technique used in this research project was first outlined by Ancell and Hakim (2007) and further explored by Hakim and Torn (2008). The sensitivity of a forecast metric  $J$  to an initial (analysis)  $i^{th}$  state variable  $x_i$  can be approximated by the following equation using an ensemble system:

$$\frac{\partial J}{\partial x_i} = \frac{\text{cov}(J, x_i)}{\text{var}(x_i)}$$

where  $\text{cov}$  denotes the covariance between the two arguments and  $\text{var}$  is the variance (Ancell and Hakim 2007). The equation simply represents linear regression.

MATLAB was the primary programming tool used to perform the ESA calculations. In order to apply a confidence interval test to account for sampling error the equation was slightly manipulated to include the correlation coefficient,  $r$ . The correlation coefficient determines the strength of the relationship, a unit-less measure and is defined as:

$$r_{J,x_i} = \frac{\sigma_{J,x_i}^2}{\sigma_J(\sigma_x)_i} \text{ or } \frac{\text{cov}(J, x_i)}{\sigma_J(\sigma_x)_i}$$

where  $\sigma_J$  and  $\sigma_x$  are the standard deviation of  $J$  and  $x_i$ . Solving for  $\text{cov}(J, x_i)$  we get the following equation:

$$\text{cov}(J, x_i) = r_{J,x_i} \sigma_J (\sigma_x)_i$$

which is then substituted back into the original sensitivity formula leading to:

$$\frac{\partial J}{\partial x_i} = \frac{r_{J,x_i} \sigma_J (\sigma_x)_i}{(\sigma_x)^2_i}$$

and after cancellation:

$$\frac{\partial J}{\partial x_i} = \frac{r_{J,x_i} \sigma_J}{(\sigma_x)_i} \text{ or } \frac{\text{corr}(J, x_i) \sigma_J}{(\sigma_x)_i}$$

where  $\text{corr}(J, x_i)$  represents the correlation between  $J$  and  $x_i$ . The equation is kept in this format since we are concerned how  $J$  is sensitive to changes in  $x_i$ .

In the present analysis,  $dJ/dx_i$  sensitivities are found for  $x_i$  using  $\mathbf{x}$ , where  $\mathbf{x}$  is a column state vector containing first layer u, v-component winds. As described later,  $J$  is the water vapor mixing ratio,  $Q_v$ , in our forecast region of interest.

## B. ADDRESSING STATISTICAL SAMPLING ERROR

Sampling error is introduced into the ESA given that the ensemble sensitivity is estimated from a finite sample. We address the sampling error by testing for statistical significance. The null hypothesis will simply be that there is no significant correlation between the initial state variable and the forecast metric with 95% confidence. The null hypothesis will be rejected if the absolute value of the correlation coefficient is greater than its 95% confidence bounds as estimated from the ensemble data (Torn and Hakim 2008).

Probability values (p-values),  $p[J, x_i]$  associated with each correlation coefficient,  $r[J, x_i]$  were computed and used in the interval test. The p-value is the probability of getting a correlation as large as the observed value by random chance when the true correlation is zero (Wilks 2006). P-values were computed in MATLAB by transforming the correlation to create a t-statistic having  $n-2$  degrees of freedom. These values are then used for testing the null hypothesis of no significant correlation. When using a 95% confidence interval and if  $p[J, x_i]$  is small (less than 0.05), then we consider the  $r[J, x_i]$  to be significant and we can reject the null hypothesis (Wilks 2006).

To estimate the sampling error associated with the sensitivities we calculated the upper and lower bounds for a 95% confidence interval for each correlation coefficient. The confidence bounds are based on asymptotic normal distribution of:

$$0.5 * \log \frac{(1+r)}{(1-r)}$$

with an approximate variance equal to:

$$\frac{1}{n-3}.$$

## C. MODEL SETUP

The ensemble system uses the Advanced Research version 3.2.1 of the WRF (ARW; Skamarock et al. 2008) configured at different forecast lengths that all end at 0600 UTC 23 January 2009. The WRF is a next-generation mesoscale numerical prediction system designed to serve both operational and research needs (Skamarock et al. 2008).

### 1. Nesting Configuration

The ensemble system uses an Arakawa-C staggered grid and telescoping nested lateral boundary conditions (Skamarock et al. 2008). Each domain in the model contains 60 vertical  $\eta$ -levels with the model top being 100 hPa. The outermost grid domain uses 36-km horizontal grid spacing, the middle domain uses 12-km horizontal grid spacing and the inner domain uses 4-km grid spacing. Figure 3 displays the three grid domains used in the forecast system. The innermost domain, centered on the Salt Lake City (SLC) Region has 222 x 183 grid points covering an 888 km x 732 km area. Figure 4 displays the innermost grid with the terrain plotted at 4-km horizontal resolution. The star denotes the SLC region.

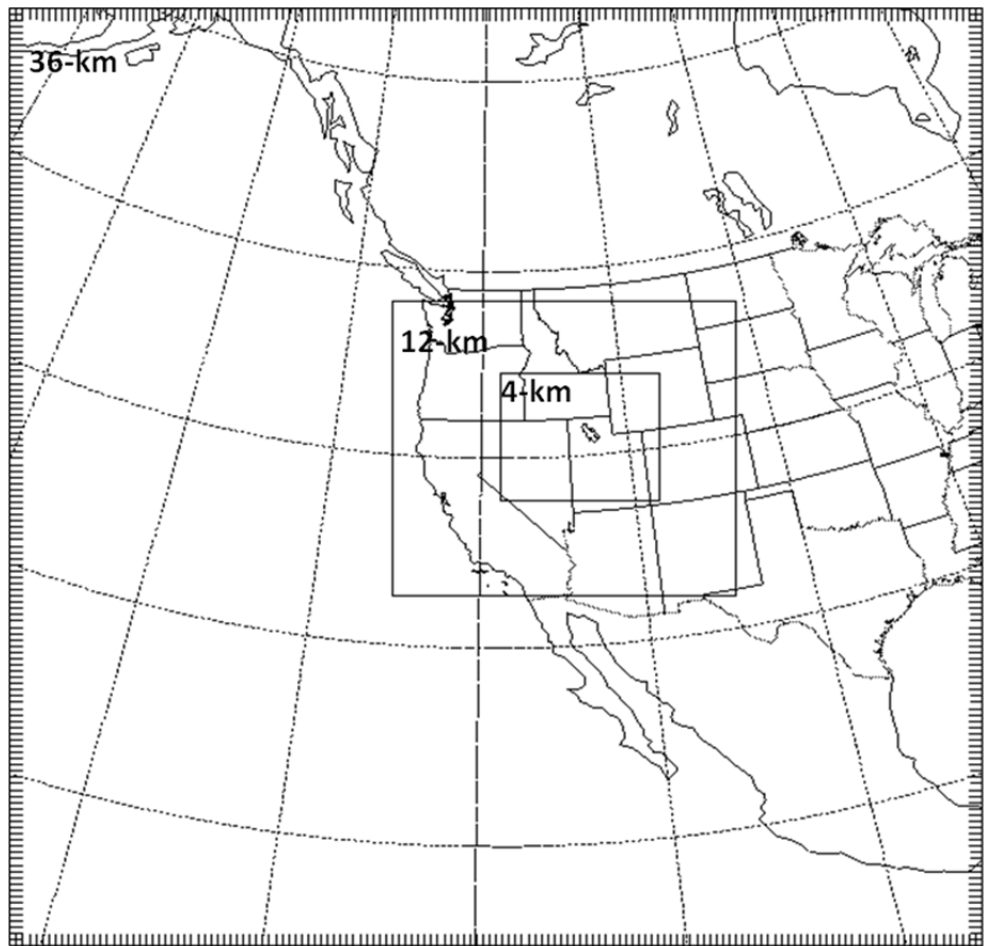


Figure 3. Nesting configuration used in the experiments. The outermost grid domain uses 36-km horizontal grid spacing, the middle domain uses 12-km horizontal grid spacing and the innermost domain uses 4 km horizontal grid spacing.

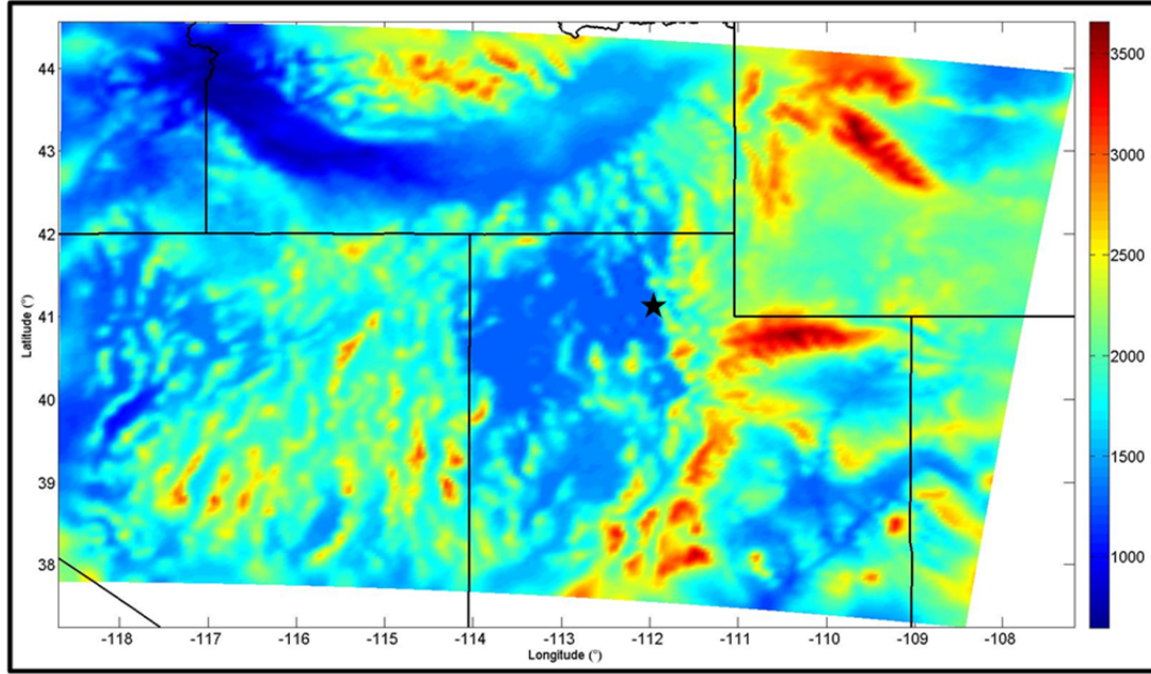


Figure 4. Innermost grid with 4 km resolution terrain (m). The star represents the SLC Region.

## 2. Vertical Coordinate System

The ensemble system uses a terrain-following hydrostatic-pressure vertical coordinate system denoted as  $\eta$  where the base is at the model's ground (Skamarock et al. 2008). Figure 7 displays an example of the coordinate system. Table 2 displays the approximate above ground level (AGL) height for the first two  $\eta$ -levels of the ensemble system. The model parameters for the first two levels were the main levels used in this project. These levels were chosen since the primary focus was a shallow mesoscale surface fog event with the majority of the column's water vapor falling within the first two model levels.

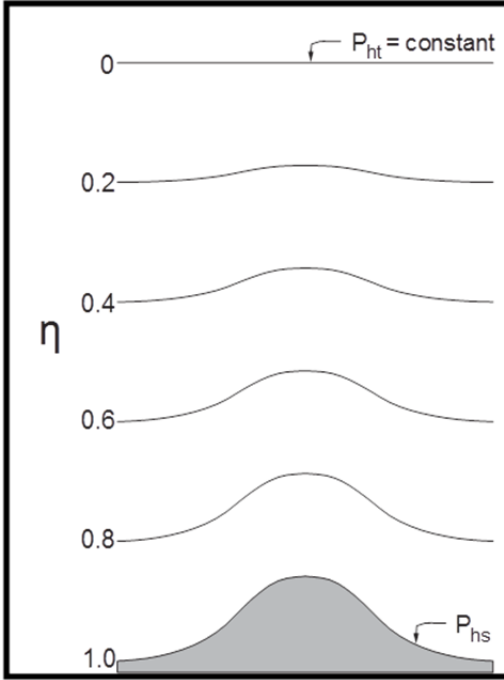


Figure 5. ARW Vertical coordinate system  
(From Skamarock et al. 2008).

Eta Level	AGL Height (m)
1	20
2	58

Table 1. The approximate above ground level (AGL) height for first two  $\eta$ -levels.

### 3. Physics

The forecasting system incorporates various physics processes within the model which are shown in Table 1. This physics suite used in the ensemble system is the same as AFWA uses operationally in their deterministic WRF forecast. The model uses the Noah land surface model (Ek et al. 2003) and the Yonsei University planetary boundary (YSU PBL) scheme (Hong et al. 2006). The WRF Single-Moment 5-Class Microphysics Scheme (WSM5 Hong et al. 2004) was used for the microphysics, which allows for mixed-phase processes and super-cooled water. The Kain-Fritsch cumulus parameterization (Kain and Fritsch 1990) was used on the outermost and middle domains

but was turned off in the innermost 4 km nested grid. The 4 km grid is generally the accepted point at which convective parameterization can be turned off. The rapid radiative transfer model (RRTM; Mlawer et al. 1997) was used for the longwave radiation scheme and the Dudhia shortwave scheme (Dudhia 1989) was used for the shortwave parameterization.

Land Surface	PBL	Microphysics	Cumulus	Longwave	Shortwave
Noah	YSU	WSM5	Kain-Fritsch	RRTM	Dudhia

Table 2. Physics processes used in the WRF system.

#### 4. Data Assimilation Process

The project started with a single “truth” WRF 10-day simulation that ran from 19–29 January 2009. Every 3 hrs the WRF soil was set to North America Regional Reanalysis (NARR), to ensure that the soil state (and lower boundary forcing) did not drift too far from reality. Synthetic observations were produced by “observing” the truth run in columns meant to mimic a network of 100 rawinsonde ascents every three hours. Observations were randomly located throughout the domain, but fixed in time. Since ESA depends on the observations assimilated we wanted to mimic the data sparse regions of southwest Asia. For this reason, we intentionally use a sparse observation network in the data assimilation process.

An ensemble was produced by assimilating those synthetic observations with the Data Assimilation Research Testbed (DART). DART, developed and maintained at the National Center for Atmospheric Research (NCAR) is an open-source community resource that provides well-documented software tools for data assimilation education, research and development (Anderson et al. 2009). Initialization of the ensemble spread at 0000 UTC 19 January is completed by adding spatially consistent, but random, perturbations drawn from the static WRF-Var error covariance field. Assimilations proceed every three hours, and by the experiment period beginning 0600 UTC 23 January, the ensemble initial conditions are independent from the random perturbations and instead reflect the assimilated synthetic observations. To ensure that uncertainty

continues to enter the domain, perturbations applied to lateral boundary conditions were also drawn from the WRF-Var static covariance, following Torn, Hakim and Snyder (2006). Figure 5 visually outlines the assimilation cycling.

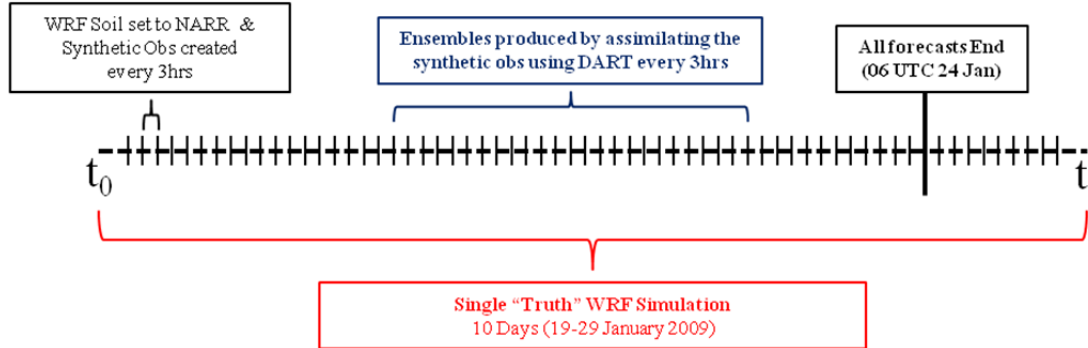


Figure 6. Assimilation Cycling.

Assimilating every three hours allowed the creation of numerous forecasts with different analyses that all end at the same time. This allows overlapping forecasts for quantifying how the model changes as a function of lead time. Figure 6 summarizes the different forecast times generated for this research project, and shows how the forecasts overlap. All runs end at 0600 UTC 24 January 2009 but were designed to encompass the fog event that started at the airport just before 0000 UTC 24 January 2009. Note the low-level wind shift that occurred in the model at 1700 UTC 23 January labeled with the red dashed line. This low-level wind shift became a factor limiting which model runs could be used to create meaningful sensitivities and will be discussed further in later sections.

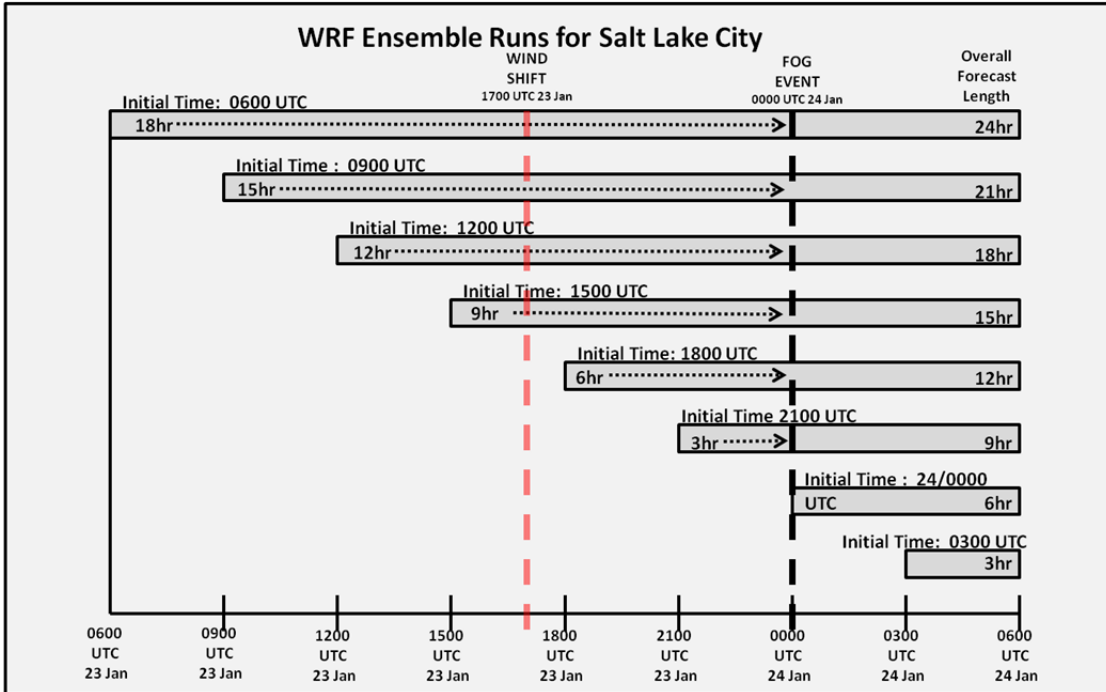


Figure 7. The WRF ensemble runs used for the project showing how overlapping forecasts can be used to determine how the model changes with a function of lead time. The figure also shows when the low-level wind shift occurred in the model. All runs end at 0600 UTC 24 January 2009 with the main focus on the fog event starting at the airport at 0000 UTC 24 January 2009.

#### D. OVERVIEW: SALT LAKE BASIN, UTAH

The main focus of this research is the complex terrain in the Intermountain West, studying the Salt Lake Basin in Utah with a focal point at the SLC International Airport. The SLC International Airport, located at  $40.79^{\circ}$  north latitude and  $-111.97^{\circ}$  west longitude is approximately three miles northwest of the city and falls in the Salt Lake valley. The elevation of the airfield is 1,288 meters (4227 ft) and the average elevation of the Salt Lake Basin is 1,320 meters (4,327 ft). The mountainous peaks of the Wasatch Range span upwards to 2,900 meters (10,500 ft) 13 miles to the northeast of the airport. There is also a mountain range that starts 15 miles to the southwest of the airport and peaks at 3,300 meters (9,000 ft) 28 miles to the southwest.

The Great Salt Lake (GSL) is roughly eight miles to the north and northwest of the airport. The lake is generally shallow and during periods of excess rain or drought

the amount of water in the lake directly north of the airport can fluctuate dramatically. Note that Figure 8 highlights the complex terrain and the lake directly around the airport. At the time the image was taken the lake was full. The topographical features displayed in this image can influence the local weather at the airport.



Figure 8. Image showing the proximity of the GSL and the terrain surrounding the SLC International Airport (After Google Maps).

The Salt Lake Basin was chosen because its elevation, topographical features, latitude and weather have similarities to the regions of complex terrain in southwest Asia. More importantly, the SLC region offers wintertime weather that is similar to the weather in the mountains in Afghanistan, Pakistan and Kyrgyzstan. Additionally, reanalysis observational data is more readily available in the CONUS opposed to the data sparse regions of southwest Asia, which allows for us to conduct research using WRF ensemble

system in a more straightforward manner. Large-scale synoptic systems frequent both Utah and southwest Asia in the winter offering a combination of snow, rain and fog that can cripple aviation operations. Wintertime fog is one of the most challenging forecast problems for the Salt Lake City National Weather Service (Slemmer 2000) and these similar forecast problems occur in the complex terrain of southwest Asia.

Jonathan Slemmer (2004), a forecaster for the SLC National Weather Service (NWS) office, documented a case study examining dense fog and its impacts to aviation at the SLC International Airport. He defined dense fog as reported visibility equal to or less than 1/4 SM without precipitation. This 30-year dense fog climatology study showed that the highest occurrence of dense fog typically occurs in the wintertime when solar radiation is at its minimum. His climatological research revealed that dense fog occurred approximately 58 hours per winter season and that most fog occurrences lasted for less than four consecutive hours. He determined that dense fog in the basin is most common in January and December when insolation is the weakest and the greatest frequency of fog occurs when the temperature ranges between 23–27°F. Slemmer found that when the winds are greater than 3 kts the dense fog normally occurs with a wind direction from the southeast or northwest. Figure 9 displays the number of fog-event occurrences as a function of wind direction and shows that fog events with wind directions from the northwest and southeast are most common at the airport due to the local mountain-valley circulations. In addition, Slemmer concluded that winds from the northwest tend to advect low-level air masses with higher relative humidity so the probability of fog occurrence is greater with this wind direction (2004).

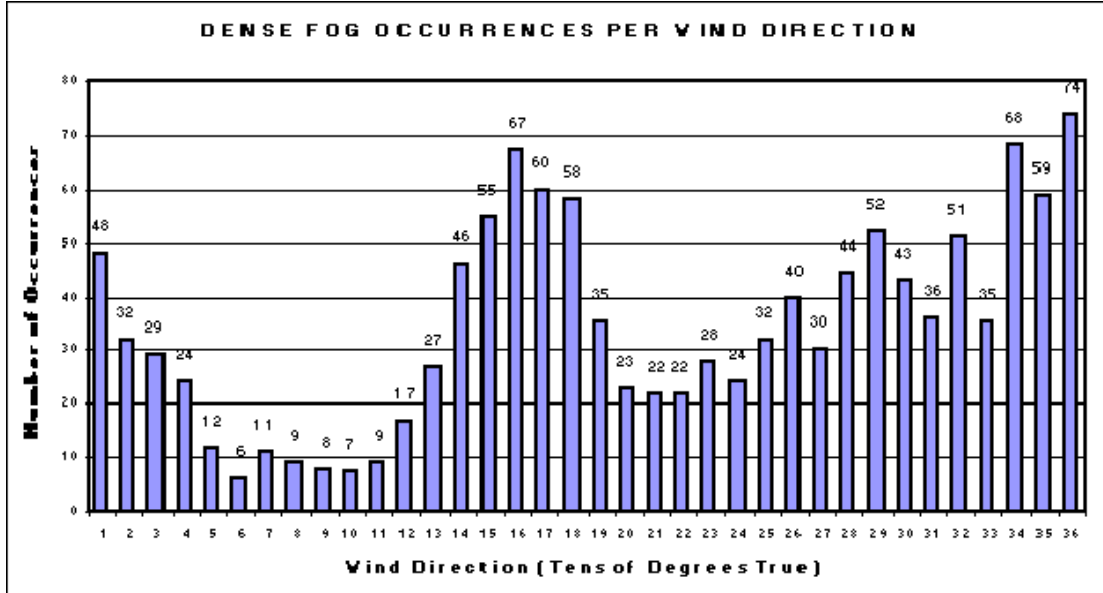


Figure 9. Dense fog occurrences as a function of wind direction at SLC International Airport (From Slemmer 2004).

David Hogan (1998), also a forecaster at the SLC NWS office studied how fog initiates in the Salt Lake Valley with respect to inversion height. He concluded that an inversion is a key element of fog development in the valley. He also determined that dense inversion related fog rarely forms or initiates when the depth of the inversion is greater than 3700 ft or when the lapse rate is less than 1.5°C per 1000 ft.

Not only is dense fog a problem during the winter in northern Utah but it is also a problem in the mountainous regions of southwest Asia. Operational climatic data summaries (OCDS) created and maintained by the 14th Weather Squadron, (the USAF's climatology center), are the primary datasets used to compare and contrast wintertime weather in northern Utah to southwest Asia bases located in complex terrain. Less than 200-ft ceilings and less than 1/2 SM visibility will be the criteria considered to be detrimental to both ground and air military operations in this region. Note in Table 3 that low ceilings and visibilities occur approximately twice as often at Manas Air Base, Kyrgyzstan when compared to SLC International Airport. This supports how fog and low ceilings hinder operations in this region and the importance of having accurate fog forecasts.

Percentage Frequency CIG/VIS Less Than 200/.5 SM					
Location	Nov	Dec	Jan	Feb	Total
SLC Int Airport, Utah	1	4	4	2	11
Manas Air Base, Kyrgyzstan	5	6	6	4	21
Bagram Air Base, Afghanistan	0	1	1	1	3
Kabul Airport, Afghanistan	0	2	2	2	6
Hours CIG/VIS Less Than 200/.5 SM					
Location	Nov	Dec	Jan	Feb	Total
SLC Int Airport, Utah	7.2	29.8	29.8	13.4	80.2
Manas Air Base, Kyrgyzstan	36	44.6	44.6	26.9	152.1
Bagram Air Base, Afghanistan	0	7.4	7.4	6.72	21.5
Kabul Airport, Afghanistan	0	14.9	14.9	13.4	43.2

Table 3. Climatology prepared from OCDS for the SLC International Airport, Manas Air Base, Bagram Air Base and the Kabul Airport

## E. SYNOPTIC SITUATION

The study period is characterized by an upper-level low over the western Rockies. SLC International Airport and the entire Salt Lake City Basin had periods of dense fog, rain and snow. More specifically, this study focuses on the nine hour period from 2300 UTC 24 January 2009 to 0800 UTC 24 January 2009 when a dense blanket of fog covered the airport. Jason Bergreen from the Salt Lake Tribune reported that the dense fog forced at least 22 airplanes to divert SLC international airport when one of its four runways closed (2009). The fog severely restricted ground operations at the airport which led to numerous delays and cancelations. The SLC NWS issued a dense fog warning lasting into the early morning until visibilities finally increased (Bergreen 2009). Throughout the 24-hr period of 0800 UTC 23 January to 0800 UTC 24 January, SLC recorded 0.22 inches of rain and 10 hours of heavy fog where visibilities were recorded at 1/4 SM or less.

### 1. Soundings

The upper air soundings from the airport indicate that a cool moist air mass was in place during the time period with a strong low-level radiation inversion present during the night. Figures 10–12 show the three soundings from 1200 UTC 23 January to 1200 UTC 24 January from the airport. The strong radiationally-forced inversion layer at the

surface apparent on the 1200 UTC 23 January sounding is shallow and approximately 40 hPa thick. The 0000 UTC 24 January sounding suggests that the low-levels had completely mixed by this time with the strong heating that occurred in the afternoon. It is reasonable to assume that the air mass had not changed and a strong low-level inversion quickly reformed after sunset setting up the meteorological conditions needed for a fog event. The 1200 UTC 24 January SLC sounding from the next morning, displayed in Figure 12, exemplifies the low-level morning inversion that was present a few hours after the fog event ended.

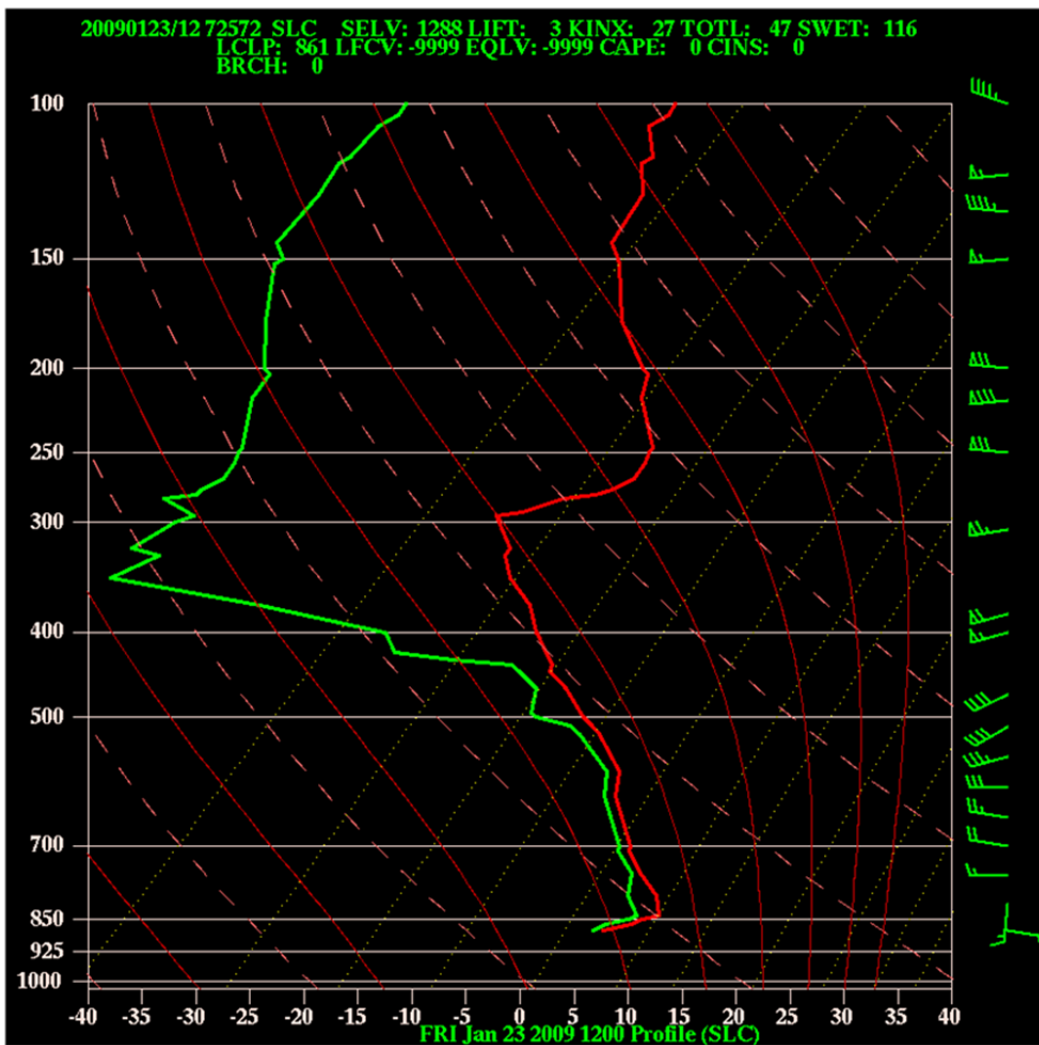


Figure 10. 1200 UTC 23 January 2009 SLC profile showing the strong low-level inversion that was present the morning before the fog event.

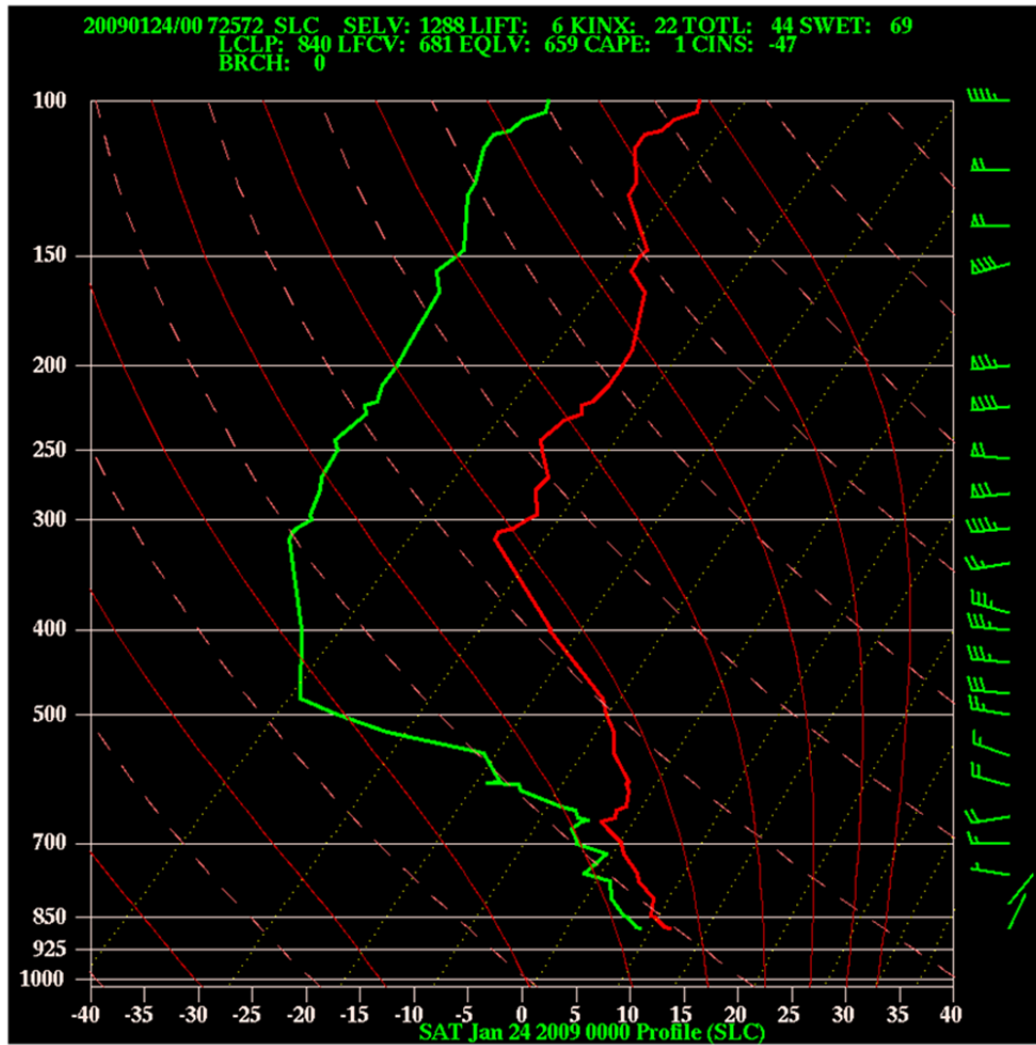


Figure 11. 0000 UTC 24 January 2009 SLC profile showing the inversion had mixed out with the strong diurnal heating that occurred in the afternoon.

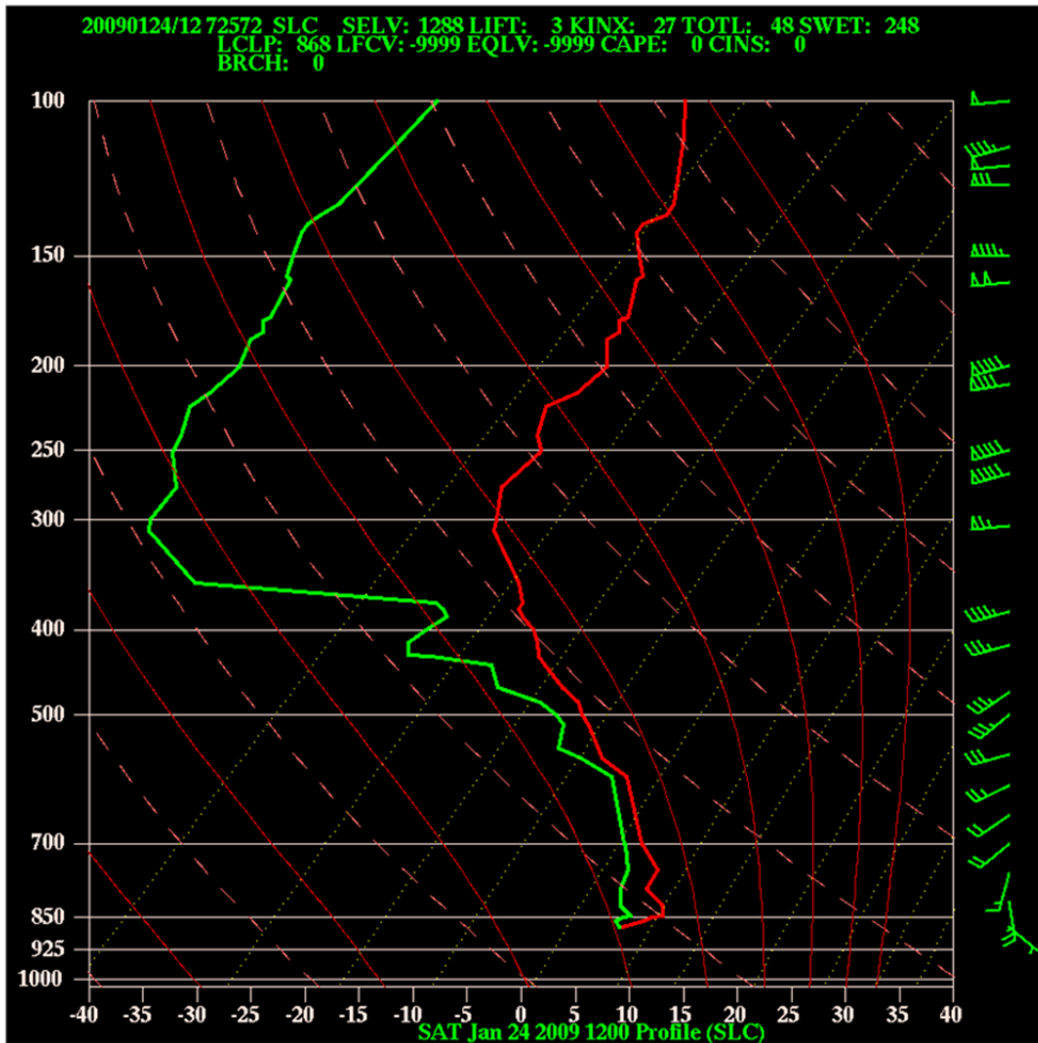


Figure 12. 1200 UTC 24 January 2009 SLC profile from the morning after the fog event showing a strong radiational inversion at the surface.

## 2. Overview

The following is a detailed description of the weather conditions that occurred at the airport during the day of the fog event. Temperatures at the airport were relatively mild throughout the day on 23 January 2009 with a low of 33°F at 1500 UTC and a high of 49°F at 2300 UTC. Compared to climatology these temperatures were approximately 10°F above normal for both the high and low temperatures, making it the second warmest day in January 2009. Surface winds were generally light throughout the day and wind speeds remained under 6 kts. Wind directions at the airport were northerly in the

morning, southerly around noon, northerly by the evening and finally switched back around to southerly after midnight. Light rain occurred in the morning, and then stopped in the early afternoon. During this time, cloud ceilings remained fairly low and ranged from 500 ft to 2500 ft. Visibilities varied between 1/4–1 1/4 SM (with mist) during the periods of intermittent rain, but increased to about 3 SM after the rain stopped at 2100 UTC (1400L). The low stratus deck thinned as the rain diminished and an 8000 ft broken ceiling was now observed from the airport. Temperatures increased rapidly as a result of solar insolation at the surface. At 2320 UTC (1620L) the winds changed to the north-northwest and visibilities quickly dropped below 1/4 SM as heavy fog blanketed the airport. Temperatures dropped 10°F in less than one hour due to the arrival of the cold moist air mass. Visibilities remained below 1/4 SM until 1000 UTC 24 January (0300L) when the winds switched back around to the southeast and the fog quickly dissipated. Over the following three days the only visibility restrictions that were recorded were in times of light to moderate snow but these visibilities remained above 1/2 SM.

Further examination indicates that a strong temperature gradient between the land and the lake most likely formed due to the abnormally warm surface temperatures. A lake breeze could have developed as a result of the differential heating between the air over the lake and the land surrounding the lake. Lake Breezes are frequent in the vicinity of the Great Salt Lake and are most common in the months of April through October (Zumpre and Horel 2006) but can still occur in the winter. If a lake breeze did develop in the afternoon it may have aided in the advection of the moisture off the lake and into the SLC region.

A University of Utah team working on the Persistent Cold-Air Pool Study (PCAPS) field campaign captured a wintertime lake breeze that may have been similar to the lake breeze that potentially formed during the fog event. This lake breeze was captured in December 2010 during a glider flight when a strong increase in surface winds was observed advecting off the lake. The surface temperatures quickly dropped and the relative humidity values increased rapidly. The lake breeze penetrated deep into the Salt

Lake Valley bringing with it cold moist air, which helped to strengthen the low-level inversion that was already in place (Galli 2010).

### **3. Physical Interpretation**

The following characteristics of the fog event are derived on limited archived weather data and personal forecasting experience. A photograph that was taken during the evening in the mountains surrounding the valley portrays the shallowness of the fog event and allows a thickness estimation of less than 200 meters. The mid-level broken layer of clouds reported in the KSLC observation is also seen in the photograph.

We concluded that the fog that occurred at the airport was radiation fog that formed over the lake and advected into the region. The light rain that occurred throughout the day provided ample moisture in the low levels. Visibilities due to mist and haze remained fairly low throughout most of the day but increased to 3 SM in the late afternoon with the heating. However, around 2320 UTC, the winds changed to the north and then to the northwest and the visibilities quickly dropped. Cold and saturated air that originated over the GSL advected over the airport. Surface temperatures dropped immediately with the arrival of the fog. The visibilities decreased from 3 SM to 0 SM in less than an hour, suggesting that the fog advected into the area.

The air traffic controllers in the tower first reported visibilities of 3/4 SM while surface visibility remained at 3 SM. This suggests that the fog was initially suspended off the ground and also supports that the fog advected into the area. However, within minutes, the surface visibility dropped to 1/16 SM and by 0000 UTC 24 January the visibility decreased to 0 SM. The fog thickened as temperatures decreased further after sunset at 0032 UTC on 24 January and remained thick until the winds switched to the south and drier air advected back into the region.

The winds that forced the advection of fog off the lake and over the airport was most likely a combination of the overall synoptic pattern, mountain and valley drainage and a possible afternoon lake breeze. An ESA of the situation could narrow the possibilities in the low-level wind that caused the fog to advect off the lake.

## **F. DETERMINISTIC MODEL COMPARISON**

The fog was a localized and mesoscale event, and could not be accurately depicted using medium and global resolution models. Post-analysis of the event using archived operational forecast models suggests the models' inaccuracy and inability to forecast the event. The Global Forecast System (GFS) was unable to depict an increase in low-level moisture in the SLC region and failed to depict the wind shift that occurred at the airport. Even a mesoscale model like the AFWA mesoscale model (MM5) with 15-km horizontal grid spacing was unable to forecast the event. The AFWA MM5 vaguely suggested an influx of low-level moisture but more importantly did not have the northerly wind shift that advected the moisture off the lake. The NOAA/NCEP 13 km Rapid Update Cycle (RUC) runs every hour out to 18 hours and performs data assimilation (DA) during every update. The RUC failed to forecast the onset of the increase in low-level moisture but did accurately depict the wind shift that occurred at the airport. After analyzing the available deterministic models it can be concluded that this particular fog event with such fine scale features would most likely be best depicted and accurately forecasted using a model with much higher resolution. In addition, a high resolution ensemble system could minimize the forecast uncertainty and increase the predictability of this localized mesoscale fog event in complex terrain.

## **G. AFWA'S MEPS NON-PRECIPITATION VISIBILITY ALGORITHM**

AFWA's probability algorithm that is used in the MEPS products outputs the probability of the visibility being at or below the given threshold ( $\leq 5\text{SM}$ ,  $\leq 3\text{SM}$ , or  $\leq 1\text{SM}$ ). The algorithm is divided into two components—the first is visibility restrictions due to precipitation and the second is visibility restriction only from fog and haze. The algorithm for forecasting visibility restrictions due solely to fog and haze uses linear equations where the probability of visibility less than or equal to a certain threshold is regressed into relative humidity (RH), wind speed (WS), and precipitable water (PWAT). PWAT is calculated by using the surface pressure and the water vapor mixing ratio ( $Q_v$ ). For the purpose of this research,  $Q_v$  will be used as the primary forecast parameter in the

ESA since it is the main parameter that drives PWAT. This also alleviates any errors that arise when calculating PWAT since it is not typically recorded into the model output file.

## **H. PARAMETERS**

It was determined through this project that the art of obtaining meaningful and robust sensitivities from a mesoscale ESA is choosing the correct  $J$  and  $x_i$ . The parameters used in this study were chosen after many trial and error tests using different model parameters schemes for both  $J$  and  $x_i$ . For this project,  $J$  will be the average ensemble  $Q_v$  in a 2x2x2 box (8-km x 8-km) located over the SLC airport summed over the first two model levels (~55 meters). The analysis state,  $x_i$ , is the u or v-wind components on the lowest model layer (~20 meters). These model parameters, which are discussed further in the next section, led to the most meaningful and useful sensitivities for the 23–24 January fog event.

## IV. RESULTS

### A. WRF ENSEMBLE PREDICTIONS

Model values at horizontal grid column located at  $x = 137$ ,  $y = 88$  are used to represent conditions at the SLC International Airport. This grid point was used because it's similarity in surface features and topography due to its proximity to the airport. Grid point  $x = 137$ ,  $y = 88$  is approximately 0.6 miles (1 km) to the northeast from the middle of the SLC airport's runway.

#### 1. MOISTURE

This study requires that the ensemble system predicts a realistic event. The timing of the fog advection is not the critical piece in the performance of the ESA. However, having an ensemble system that forecasts an increase in low-level moisture is a requirement to get meaningful sensitivities. The WRF mesoscale ensemble system predicted this mesoscale fog event in the Salt Lake Valley with much higher accuracy when compared to the available operational deterministic models discussed earlier. This is surprising given that it was not initialized with real observations and shows that it was a local event and not subject to strong dynamical forcing from larger scales. Overall, the ensembles accurately depict the dramatic influx of moisture throughout the region but all runs are approximately 3–6 hours too early on the timing when compared to the actual observations at the airport. Figure 13 shows a chart of the ensemble mean of 2-meter  $Q_v$  at the airport for a 24-hr forecast period compared to the actual  $Q_v$  computed from the airport observations. The actual  $Q_v$  remains moderately high when compared to the forecasted  $Q_v$  as light rain fell most of the morning but spiked with the arrival of the fog after 2100 UTC. The ensemble mean of  $Q_v$  for both simulations spikes after 1800 UTC suggesting the model's arrival of the moist air appears to be 3–6 hours off. Since the focus of this project is obtaining the sensitivities of the forecast the timing error is not particularly critical to the effectiveness of the ESA. For the purpose of this research the fact that the ensemble system does simulate a significant increase in low-level moisture is the most essential component in performing the sensitivity analysis.

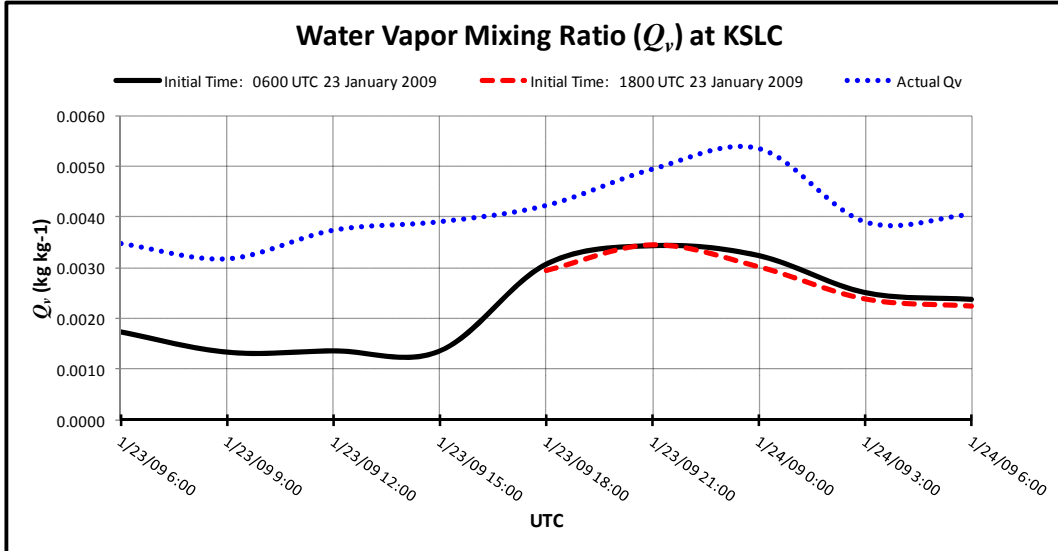


Figure 13. Forecasted 2-meter  $Q_v$  at the airport versus actual  $Q_v$  from the observations at the airport. The black solid line represents the forecast initialized at 0600 UTC 23 January and the red dashed line represents the forecast initialized at 1800 UTC 23 January. The  $Q_v$  recorded at the airport is represented by the blue dashed line. All forecasts end at 0600 UTC 24 January.

Using the ensemble initialized at 0600 UTC 23 January (24-hr forecast) and the ensemble mean (EM) of the  $Q_v$  for the lowest model level displayed in Figure 14 can give a basic understanding of how the cold, shallow and moist air mass that is originally confined to the lake advects off the lake and into the SLC Region. The star denotes the SLC International Airport. Early in the period the moisture is mainly confined to the lake. The 3-hr forecast valid at 0900 UTC outlines the moisture directly over the lake. At 1800 UTC the moisture begins advecting from over the lake to approximately 13 miles north of the airport through regions of lowest terrain surrounding the lake. By the 18-hr forecast valid 0000 UTC 24 January the moisture has further advected from over the lake and has impinged on the front range of the Wasatch Mountains. By the 21-hr forecast valid 24 January 0300UTC the model winds switch back around to more of a southerly direction. This allows for some drier air to be advected back into the SLC region and by 24 January 0600 UTC the model forecast suggests the moisture has mostly dissipated over the airport.

The forecast timing of the advection of the drier air back into the SLC valley is approximately three hours too soon when compared to what actually occurred at the airport. Visibilities at the airport quickly increased from 1/8 SM to 2 SM after 24 January 0900 UTC (0200L) as a steady southeasterly wind advected drier and warmer air into the valley. The last two panels in Figure 14 suggest the drier air being mixed back in throughout the valley.

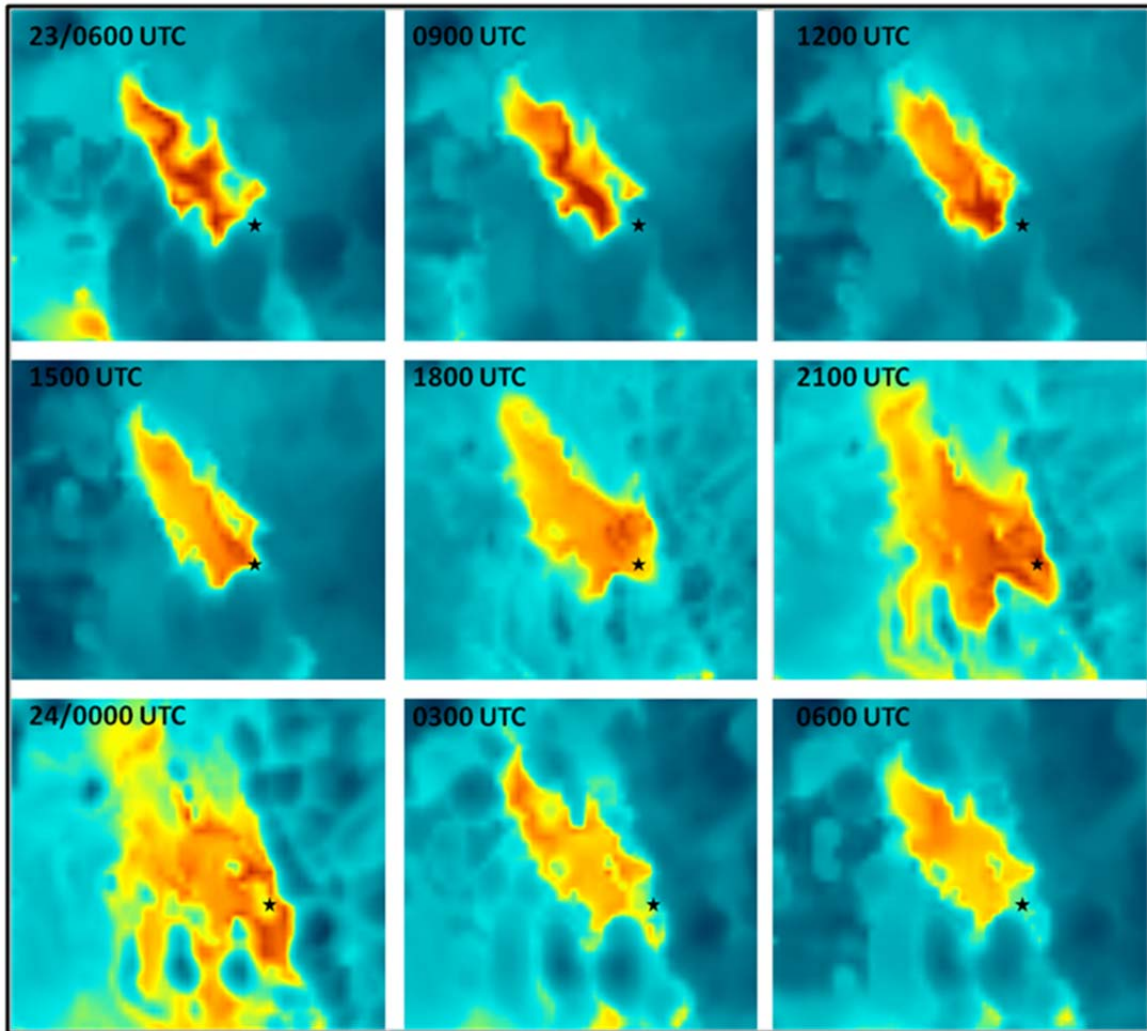


Figure 14. 0-24hr EM  $Q_v$  for the lowest model level from the ensemble initialized at 0600 UTC 23 January 2009. The brightest yellow colors indicate the highest  $Q_v$  values.

Overall, the WRF ensemble system did a good job forecasting the moisture during the fog event but the timing was off. The model advects in the moisture approximately 3–6 hours early and advects the drier air into the region three hours early at the end of the event. However, the fact that the ensemble system simulated this mesoscale fog event is essential in determining meaningful sensitivities of forecasted fog in complex terrain.

## 2. WINDS

Figure 15 is the ensemble mean of the u-component winds at the airport for the first  $\eta$ -level, approximately 20 meters, for two different model runs. The solid black line is the ensemble initialized at 0600 UTC 23 January (24 hr forecast) while the red dashed line represents the ensemble initialized at 1800 UTC 23 January (12 hr forecast). The 24-hr ensemble forecasts negative winds early in the period but forecasts a wind shift between 1200–1800 UTC. This wind shift will be a key factor in the sensitivity analysis. After the wind shift the u-component winds remain positive through the end of the period. The 12 hr ensemble forecasts positive u-component winds early in the period then become mostly calm to slightly negative around 24 January 0300UTC and remain the same through the end of the period. Using only the u-component winds allows us to conclude that the 20-meter winds have an easterly component early in the period and switch to a more westerly component between 1500–1800 UTC.

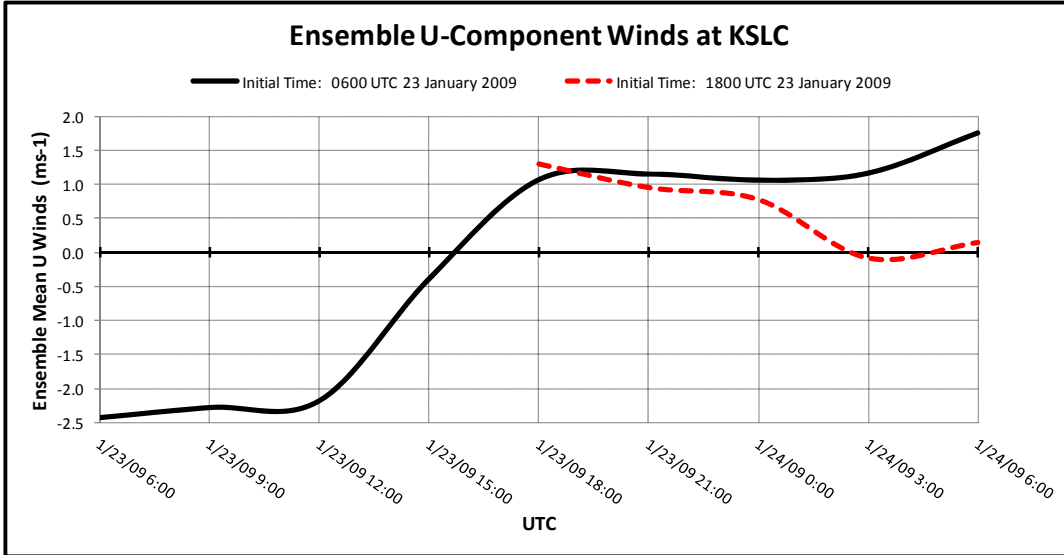


Figure 15. Ensemble u-component winds at SLC international airport at 20 meters. The black solid line represents the forecast initialized at 0600 UTC 23 January and the red dashed line represents the forecast initialized at 1800 UTC 23 January. All forecasts end at 0600 UTC 24 January.

Figure 16 is the ensemble mean of the v-component winds at the airport for the first  $\eta$ -level for two different model runs. The v-component winds vary in approximately the same magnitude as the u-component winds. The solid black line is the model run initialized at 0600 UTC 23 January (24 hr forecast) while the red dashed line is initialized at 1800 UTC 23 January (12 hr forecast). The model initialized at 0600 UTC 23 January forecasts positive winds early in the period and become negative between 1500 and 1800 UTC. The winds remain negative for both model runs until approximately 0300 UTC 24 January when they become just positive. The wind shift that occurs between 1500 and 2100 UTC aligns well with the shift in u-component winds at the same time.

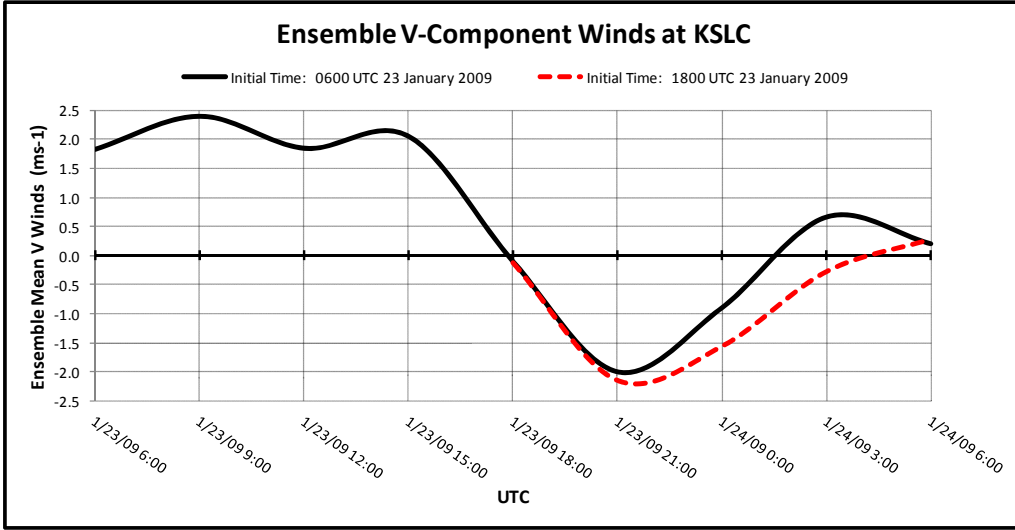


Figure 16. Ensemble v-component winds at SLC International Airport at 20 meters. The black solid line represents the forecast initialized at 0600 UTC 23 January and the red dashed line represents the forecast initialized at 1800 UTC 23 January. All forecasts end at 0600 UTC 24 January.

The surface wind data was recorded from airport's automated observing system at a height of 10 meters and can be equally compared to the 10-meter model winds. The 10-meter wind direction and speed are displayed in Figures 17 and 18 were computed using both components of the 10-meter wind and are compared to the actual wind speed and direction taken from the airport. The actual winds recorded at the airport are generally light ( $<3 \text{ m s}^{-1}$ ) for the entire period and most likely do not truly represents the wind direction throughout the SLC region due to the complex terrain.

When compared to the actual surface winds, the model does a good job with the overall trend of the wind direction. However, the model forecasts the wind shift 3–6 hours early compared to what actually occurred at the airport between 2100 23 January and 0000 UTC 24 January. This timing error in the wind shift corresponds well with the timing error of the model's arrival of the moisture at the airport as discussed earlier. The model does forecast a switch in the winds back to the south at the end of the period and aligns well with the general shift back to the southerly direction that occurred at the airport. However, this shift appears to be approximately three hours too early.

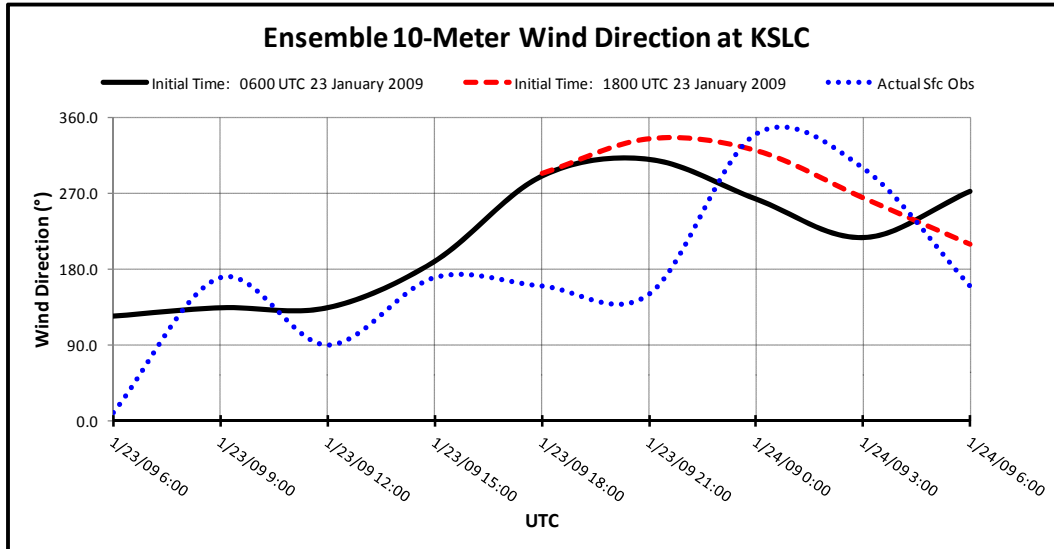


Figure 17. Ensemble 10-meter wind direction compared to the actual wind direction at SLC International Airport. The black solid line represents the forecast initialized at 0600 UTC 23 January and the red dashed line represents the forecast initialized at 1800 UTC 23 January. All forecasts end at 0600 UTC 24 January. The blue dashed line represents the actual surface wind direction recorded at the airport.

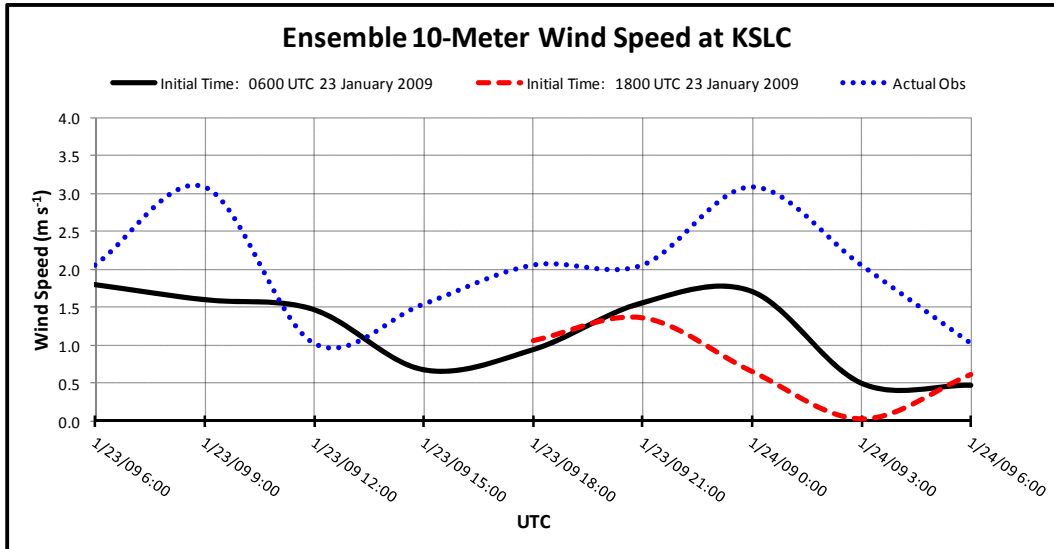


Figure 18. Ensemble 10-meter wind speed compared to the actual surface wind speed at SLC International Airport. The black solid line represents forecast initialized at 0600 UTC 23 January and the red dashed line represents the forecast initialized at 1800 UTC 23 January. All forecasts end at 0600 UTC 24 January. The blue dashed line represents the actual surface wind speed recorded at the airport.

The 1800 UTC 23 January analysis EM wind direction at 20 meters throughout the entire domain is plotted in Figure 19. The small box southeast of the lake is the location of the airport. Notice how the winds are northeasterly in the region northwest of the lake and north-northwesterly over the lake.

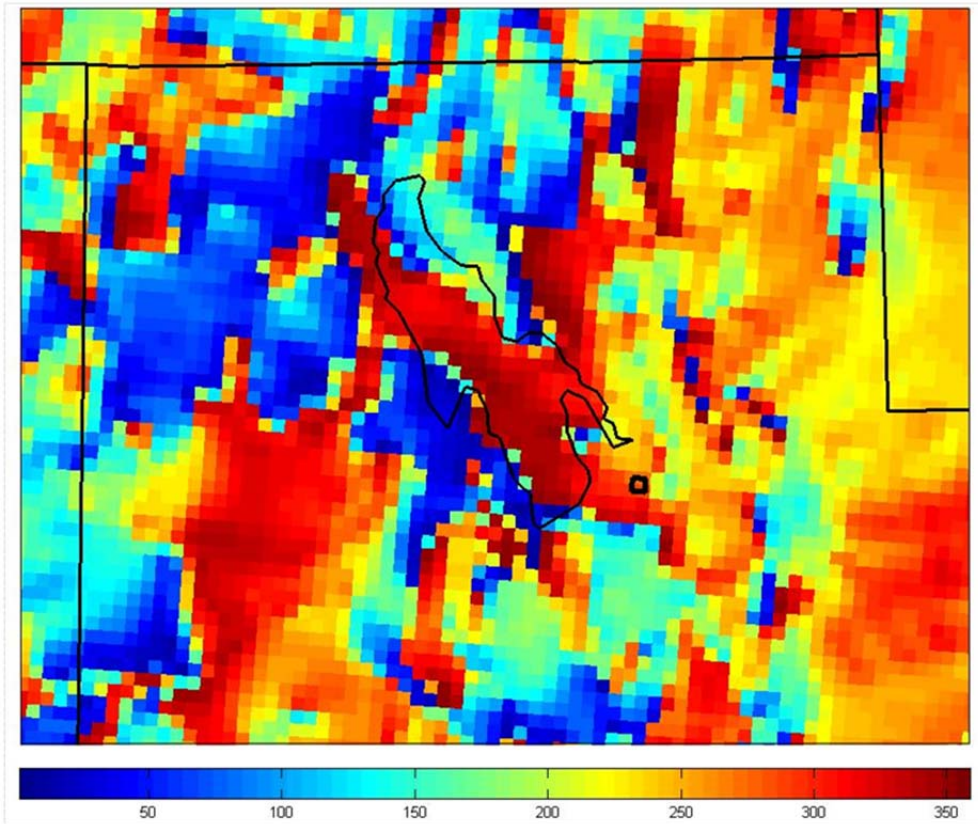


Figure 19. 1800 UTC 23 January 2009 analysis low-level wind direction at 20 meters. The chart is an EM of analyses for all 96-members. The colors correspond to the wind directions labeled at the bottom of the chart.

## B. CONCEPTUAL MODEL

Figure 20 depicts a schematic interpretation of the 1800 UTC 23 January low-level analysis wind using the directions in Figure 19 and the known local climatology. Only the winds that could have directly influenced the moisture advection into the airport six hours later are shown. It is our best estimate that the stronger climatological northeasterly winds through the large valley of southern Idaho have the strongest

influence on the winds in the Salt Lake Basin during this event. These winds are forced down the valleys north of the Salt Lake and into the Salt Lake Basin.

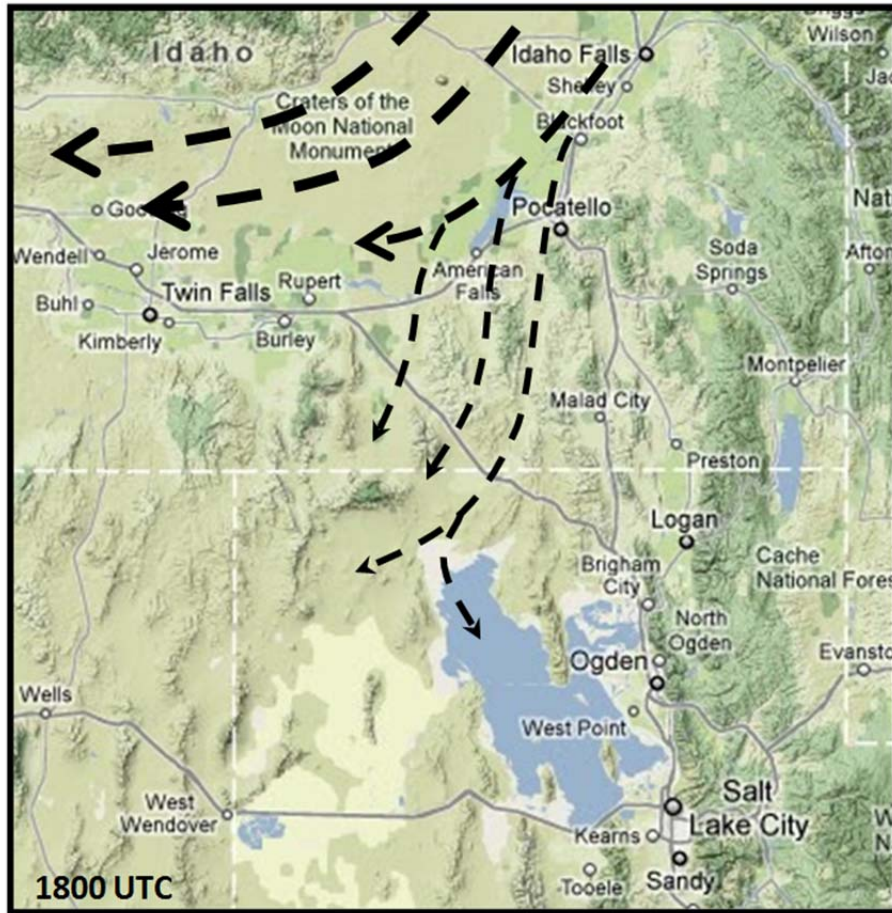


Figure 20. Schematic interpretation of the 1800 UTC 23 January low-level wind flow that influenced the advection of moisture off the lake and into the SLC Basin (After Google Maps).

Figure 21 is a closer schematic of the 1800 UTC analysis winds of just the Salt Lake Basin. The low-level winds are mainly northeasterly to the north-northwest of the lake and channel in toward the lake through the Curlew and Hansel valleys. As the low-level wind encounters the lake it travels the extent of the lake and exits the lake in the southeast through the regions of some of the lowest terrain. This area of lowest terrain is located 13 miles to the north of the airport and has an elevation that is roughly 15 ft less than the airport. This is also the region where a potential lake breeze developed due to the

strong differential heating between the land and the lake. This lake breeze could have aided the advection of moisture off the lake. After the wind pushes off the lake it turns as it reaches the base of the Wasatch Mountains. Some of the wind turns and pushes to the southwest towards the airport and some to the northwest.

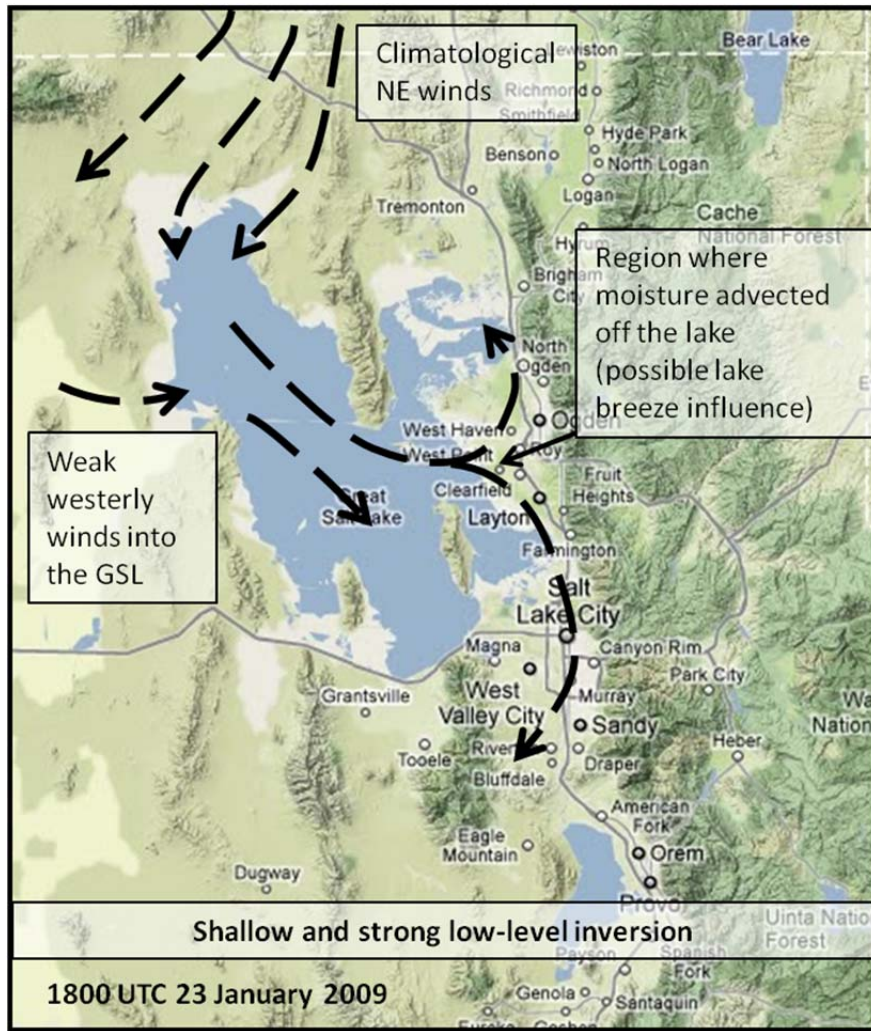


Figure 21. Closer schematic interpretation of the 1800 UTC 23 January low-level wind flow that influenced the advection of moisture off the lake and into the SLC Basin (After Google Maps).

A conceptual sensitivity field can be constructed using the 1800 UTC analysis u-component winds as the analysis state vector ( $\mathbf{x}$ ) and  $Q_v$  at the airport six hours later as the forecast metric ( $J$ ). Using the analysis u-component winds and the fact that the low-level moisture increased dramatically in a box over the airport at 0000 UTC 24 January

we can conceptually expect to have the sensitivity field shown in Figure 22. Since  $Q_v$  is always a positive variable the sign of the sensitivities depends on the sign of the component of the wind. We can expect to have negative sensitivities displayed in the blue regions where there are negative (easterly) u-component winds and positive sensitivities in the red regions where we have positive (westerly) u-component winds.

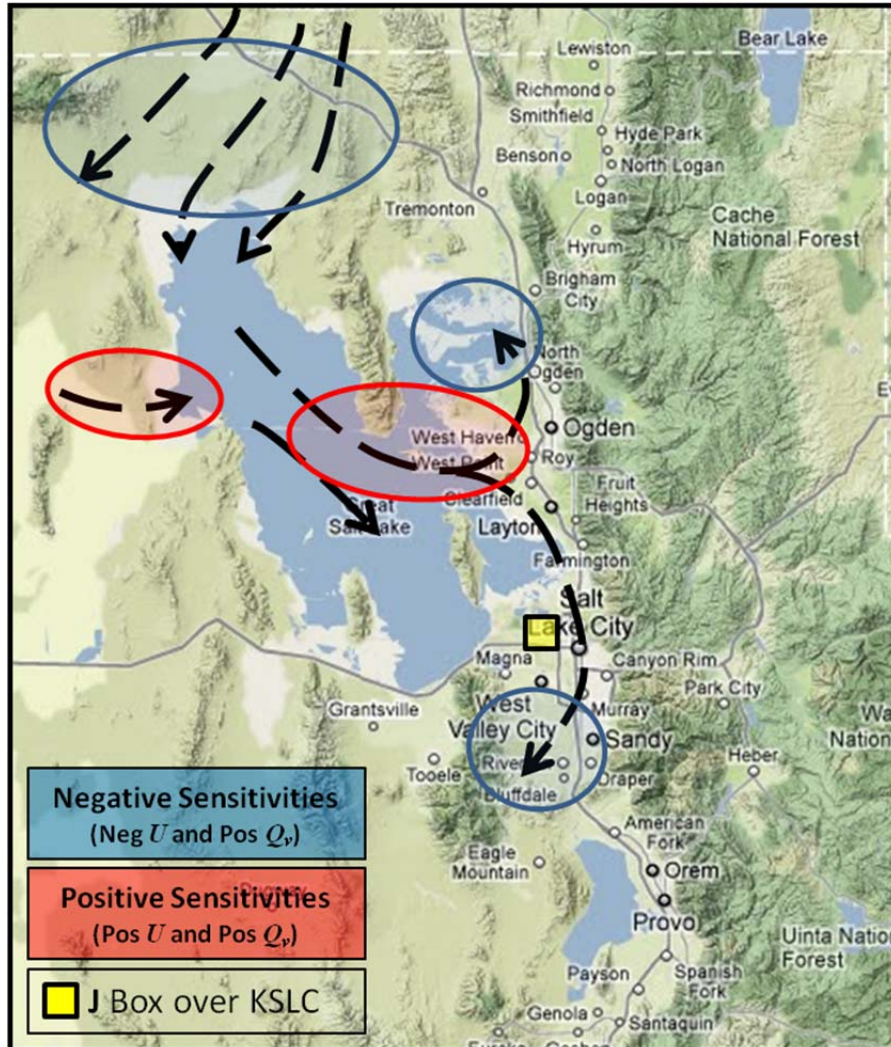


Figure 22. Conceptual sensitivity field using 1800 UTC 23 January 2009 analysis u-component winds as the analysis state variable ( $x$ ) and  $Q_v$  at 0000 UTC 24 January 2009 as the forecast metric (J) for the box centered over the SLC airport (After Google Maps).

Using the 1800 UTC 23 January analysis v-component winds as  $x$  and  $Q_v$  six hours later at the airport as J we can expect to have the sensitivities shown in Figure 23.

Since  $Q_v$  is always a positive variable the sign of the sensitivities depends on the sign of the component of the wind. We can expect to have negative sensitivities displayed in the blue regions where there are negative (northerly) v-component winds and positive sensitivities in the red regions where we have positive v-component (southerly) winds.

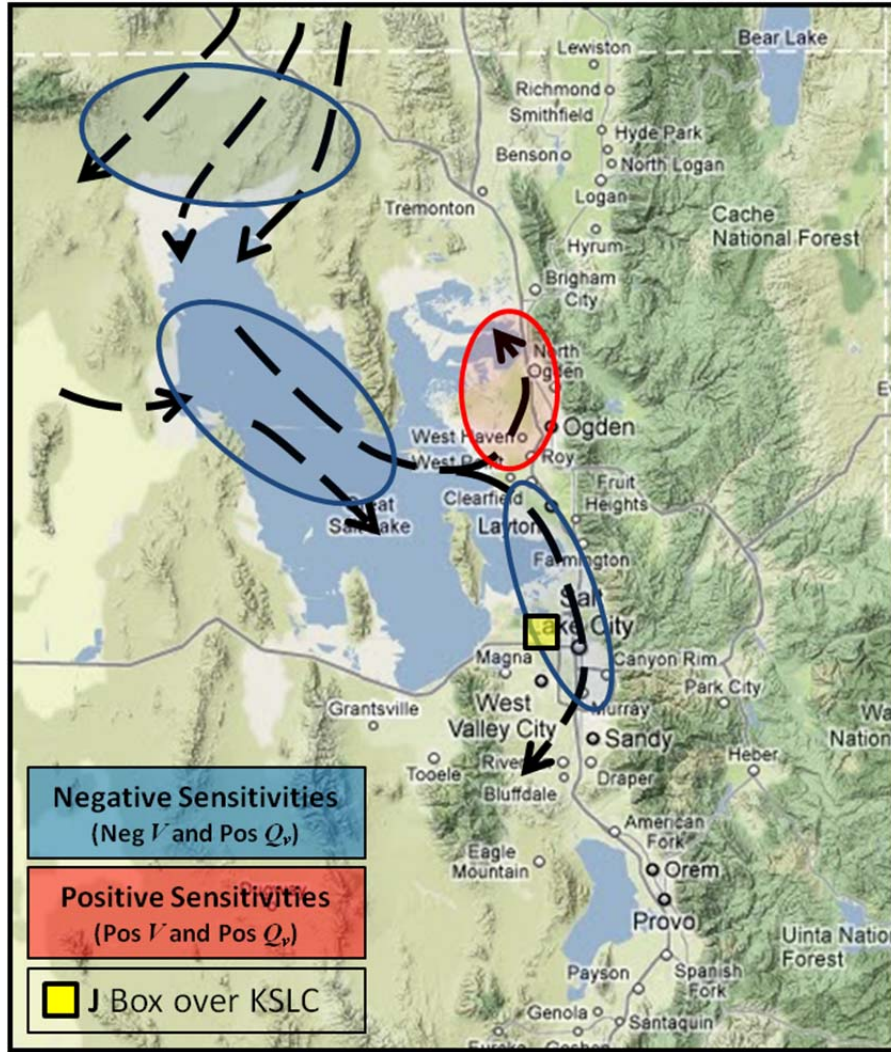


Figure 23. Conceptual sensitivity field using 1800 UTC 23 January 2009 analysis v-component winds as the analysis state variable ( $x$ ) and  $Q_v$  at 0000 UTC 24 January 2009 as the forecast metric ( $J$ ) for the box centered over the SLC International Airport (After Google Maps).

### C. QUANTITATIVE ESA RESULTS

The quantitative results were obtained using the ESA calculation discussed in section 3.A. The u and v-component winds at the lowest model level ( $\sim 20$  m) were used as  $\mathbf{x}$ . The lowest model level was used because it is determined that the wind near the surface was the most important factor in advecting the low-level moisture toward the airport. Other analysis state variables were experimented with in the project including wind speed, wind direction, temperature, 10-meter u-component winds, 10-meter v-component winds and 2-meter temperature but the best results achieved were from the first model layer u and v-component winds. The water vapor mixing ratio,  $Q_v$  was chosen as  $J$  because of its significance in the AWFA's fog algorithm. Through experimentation it was determined that summing  $Q_v$  over the first two  $\eta$ -levels led to the most useful and robust sensitivities. This was likely due to the shallowness of the fog and the fact that the majority of the column's  $Q_v$  was located within the first two  $\eta$ -levels. Other  $J$  parameters tried in the experimentation included temperature, 2-meter temperature, RH, and PWAT but  $Q_v$  led to the best results and the most useful sensitivities for this fog event.

Confidence on sensitivities was computed using a 95% confidence interval as discussed in section 3.B to address sampling error. All sensitivities failing this interval were masked and displayed as white space in the images. Using a wind component for  $\mathbf{x}$  and  $Q_v$  for  $J$  leads to  $dJ/d\mathbf{x}$  sensitivities in units of water vapor ( $\text{kg kg}^{-1}$ ) per unit standard deviation of wind ( $\text{m s}^{-1}$ ). This states that every time either the analysis u-component or v-component wind is changed by  $\pm 1\sigma_{\mathbf{x}}$  at a particular location, the forecast metric changes by a specified amount of water vapor in the  $J$  box. The strength of the sensitivities is essentially driven by two factors, the correlation coefficient and  $\sigma_{\mathbf{x}}$ . For example, a strong correlation coefficient combined with a small  $\sigma_{\mathbf{x}}$  will lead to strong sensitivities.

## 1. ESA Results

### a. *U-Component Winds*

Using the 1800 UTC 23 January analysis u-component winds and forecasted  $Q_v$  valid six hours later at 0000 UTC 24 January we quantitatively obtained the sensitivities in Figure 24. To provide orientation the GSL is outlined in black and J was taken from a 2x2x2 grid cell (8-km x 8-km box) centered over the airport. Units displayed here are  $\text{kg kg}^{-1}$  per  $\text{m s}^{-1}$ . To determine how much  $Q_v$  would change at the airport the units must be in  $\text{kg kg}^{-1}$  and this was calculated separately. The white space in the image is where the sensitivities are masked because the statistical significance of the linear regression is less than the 95% confidence level. The 1800 UTC analysis  $\sigma_u$  values for the u-winds throughout the 4-km domain were  $0.02\text{-}0.31 \text{ m s}^{-1}$  and represent the variation in light surface winds.

Sensitivities fall very much in line with our conceptual model presented earlier. The region of strong positive sensitivities approximately 13 miles to the north of the airport labeled as region 1 is where the low-level moisture advected off the lake and into the SLC region. The positive correlations indicate that strong low-level flow off the lake through this region will lead to increased moisture at the airport. Quantitatively, the sensitivities predict that a  $\pm 0.09 \text{ m s}^{-1}$  ( $1\sigma_u$ ) in the initial u-component wind in this region will result in a  $\pm 2.197 \times 10^{-5} \text{ kg kg}^{-1}$  change in the 6-hr  $Q_v$  forecast at the airport.

The negative sensitivities north and south of the positive region, labeled as region 2, are areas where the u-component low-level winds are negative. This is where the wind pushes off the lake into the front range of the Wasatch Mountains. The mountains turn the flow to the north and the south and add in an easterly component. The easterly component leads to negative sensitivities that predict a  $\pm 0.08 \text{ m s}^{-1}$  ( $1\sigma_u$ ) change in the analysis here will result in a forecasted  $\mp 1.506 \times 10^{-5} \text{ kg kg}^{-1}$  change in the water vapor mixing ratio six hours later at the airport.

The negative sensitivities to the northwest of the lake, labeled as region 3, are also an important area of sensitivities. The maximum region of negative sensitivities northwest of the lake predict that  $\pm 0.07 \text{ m s}^{-1}$  ( $1\sigma_u$ ) change in the u-component low-level

winds here will lead to a  $\mp 1.556 \times 10^{-5}$  kg kg $^{-1}$  change in the 6-hr water vapor mixing ratio forecast at the airport. It can be assumed that this is the region where a northeast wind that pushes out of the Curlew and Hansel valleys can channel over the lake and can advect off the lake and over the airport.

Region 4 is the final area of sensitivities that are considered to be important to the 6-hr forecast of  $Q_v$  at the airport. In this region a  $\pm 0.16$  m s $^{-1}$  ( $1\sigma_u$ ) change in the low-level u-component winds here is expected to produce a  $\pm 1.111 \times 10^{-5}$  kg kg $^{-1}$  change in the 6-hr  $Q_v$  forecast at the airport. This suggests that a westerly low-level wind immediately west of the lake can influence the amount of  $Q_v$  obtained at the airport.

All other regions are sensitivities where we cannot draw the physical link between analysis u-component winds and changes in the 6-hr  $Q_v$  at the airport. For example, the strong positive sensitivities in the Wasatch Mountains labeled as region 5 are where the winds are on a magnitude of 3-4 times larger than anywhere else in the valley and are only stronger due to the higher elevations. This leads to areas of strong sensitivities but will be ignored for this project simply because we are unable to draw the physical link between sensitivities and the change in  $Q_v$  at the airport. Sensitivities far from the airport may have a physical link to the  $Q_v$  at the airport but it is hard to determine this connection. Sampling error will cause the ESA to overestimate the sensitivities throughout the domain leading to sensitivities that do not have direct physical connection. A function applied within the ESA, to restrict the spatial extent of the regressions underlying the ESA, may help eliminate the sensitivities that meet the interval test but do not have a direct link to J.

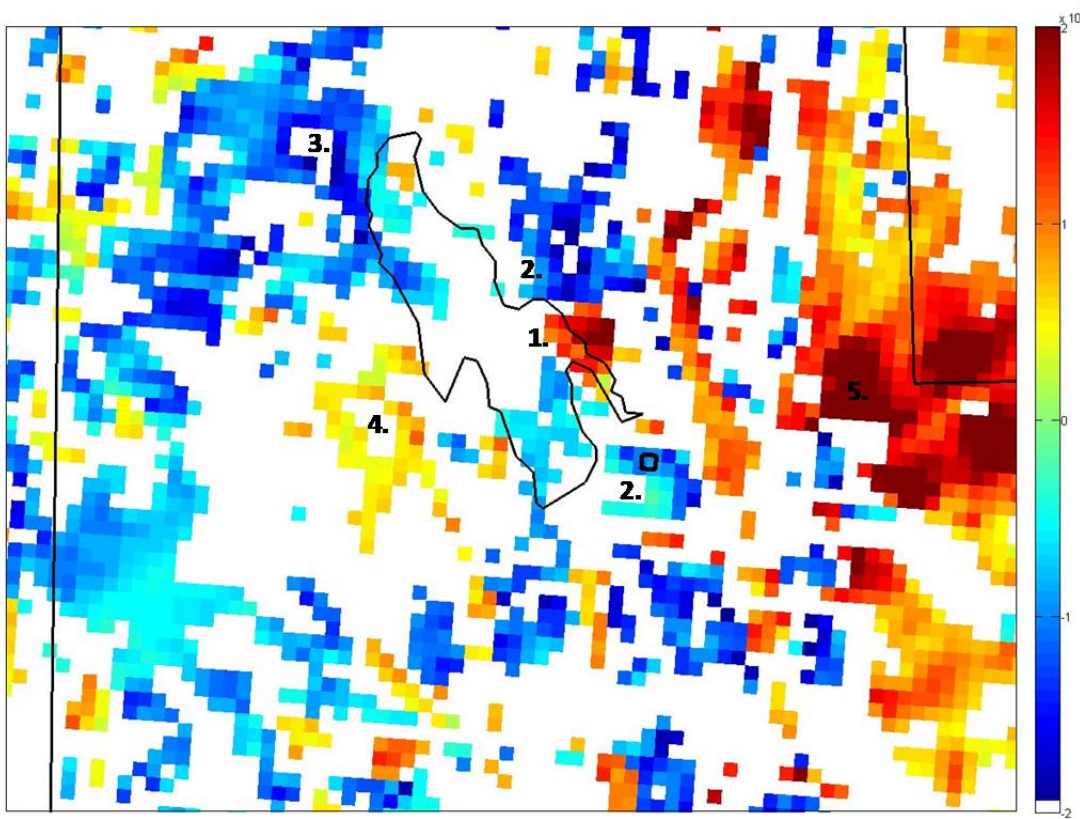


Figure 24. Sensitivities ( $dJ/dx$ ) using 1800 UTC 23 January u-component analysis winds ( $ms^{-1}$ ) (x) and forecasted  $Q_v$  (J) ( $kg\ kg^{-1}$ ) valid at 0000 UTC 24 January. Units are  $kg\ kg^{-1}$  per  $m\ s^{-1}$ .

The overall quantitative ESA results using the u-component winds are comparable to the conceptual model presented earlier. This result leads us to conclude that the linearity assumptions in the ESA may be valid. Linearity tests performed on the sensitivity-analysis predictions will help support the linear assumptions and will be discussed further.

#### *b. V-Component Winds*

Figure 25 is the quantitative results of the ESA using the 1800 UTC 23 January analysis first model-level v-component winds and forecasted  $Q_v$  valid six hours later at 0000 UTC 24 January. Overall, the quantitative results using the v-component winds align with the conceptual model but without the detail that was obtained using the u-component winds. The  $\sigma_v$  for the v-component winds throughout the 4-km domain

were 0.02-0.39 m s<sup>-1</sup> at the 1800 UTC analysis and represent the variation in the light winds. Region 1 represents an area of negative sensitivities that predicts a  $\pm 0.16$  m s<sup>-1</sup> ( $1\sigma_v$ ) change in v-component winds in this location will lead to  $\mp 1.785 \times 10^{-5}$  kg kg<sup>-1</sup> change in the 6-hr  $Q_v$  forecast at the airport. Conceptually this makes sense since northerly winds tend to advect moisture into the airport. Region 2 represents an area of positive sensitivities where a  $\pm 0.26$  m s<sup>-1</sup> ( $1\sigma_v$ ) change in v-component winds in this location will lead to  $\pm 1.676 \times 10^{-5}$  kg kg<sup>-1</sup> change in the 6-hr  $Q_v$  forecast at the airport. This is the area where the winds tend to turn back to a northerly direction after hitting the front range of the Wasatch Mountains. The negative sensitivities in regions 3 and 4 predict that  $\pm 0.16$  m s<sup>-1</sup> and  $\pm 0.20$  m s<sup>-1</sup> ( $1\sigma_v$ ) change will lead to a  $\mp 1.831 \times 10^{-5}$  kg kg<sup>-1</sup> and  $\mp 8.308 \times 10^{-6}$  kg kg<sup>-1</sup> change in  $Q_v$  six hours later at the airport and supports the concept that northerly winds over the lake influence the amount of moisture obtained at the airport.

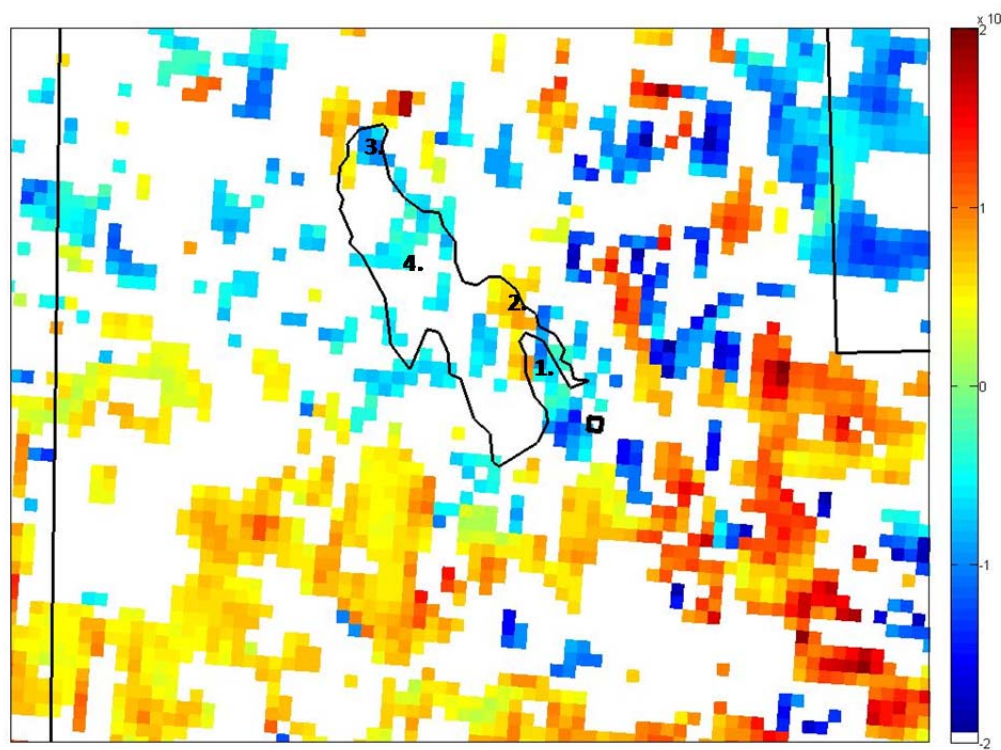


Figure 25. Sensitivities ( $dJ/dx$ ) using 1800 UTC 23 January v-component analysis winds (ms<sup>-1</sup>) (x) and forecasted  $Q_v$  (J) (kg kg<sup>-1</sup>) valid at 0000 UTC 24 January. Units are kg kg<sup>-1</sup> per m s<sup>-1</sup>.

Using the 1800 UTC 23 January 2009 analysis and a forecast six hours later, the u-component wind trended toward quantitative results that better matched the conceptual thinking when compared to the v-component winds. This leads to the conclusion that for this fog event the changes in the analysis u-component versus v-component winds appear to have a greater impact in the changes in  $Q_v$  forecasted at the airport.

## 2. Wind Shift

The 1800 UTC 23 January analysis is the earliest analysis that could be used to produce skillful and meaningful sensitivities. This is because of the 1700 UTC 23 January wind shift that occurred throughout the SLC Basin represented in Figures 15–17. Using analyses before the 1700 UTC wind shift led to a different trend in sensitivities compared to analyses after the wind shift. It was difficult to provide a direct physical link between these sensitivities and the exact changes that occurred in  $Q_v$  at the airport. Figure 26 shows the sensitivities using 1500 UTC 23 January u-component winds for  $\mathbf{x}$  and  $Q_v$  at the airport valid at 0000 UTC 24 January, nine hours later for  $\mathbf{J}$ . The region of positive sensitivities to the west of the airport suggests that a westerly wind will advect moisture from the GSL over the airport. This makes conceptual sense but for this fog event that occurred at the airport the moisture advected from the north. To test the physical linearity of the sensitivities we perform linearity tests on the stronger u-sensitivities using analyses before and after the wind shift to clarify if these ESA approximations hold valid through a wind shift. Linearity tests to analyses before and after the wind shift are presented in section 4.D. These tests show the non-linearity of the ESA using the analysis before the wind shift and suggest that the strong relationship between forecasted  $Q_v$  and analysis u-component winds does not hold true when a wind shift occurs between the analysis and the forecast.

This was one disadvantage that was discovered using surface winds as  $\mathbf{J}$  in the ESA for this case study. The ESA approximations appear to be valid as long as there is no significant shift in the wind between the analysis and the forecast. For this particular event, the wind shift limited the length of the forecast in the ESA. In future mesoscale

ESAs it can be anticipated that a wind shift may occur when using surface wind and this should be considered when analyzing the results.

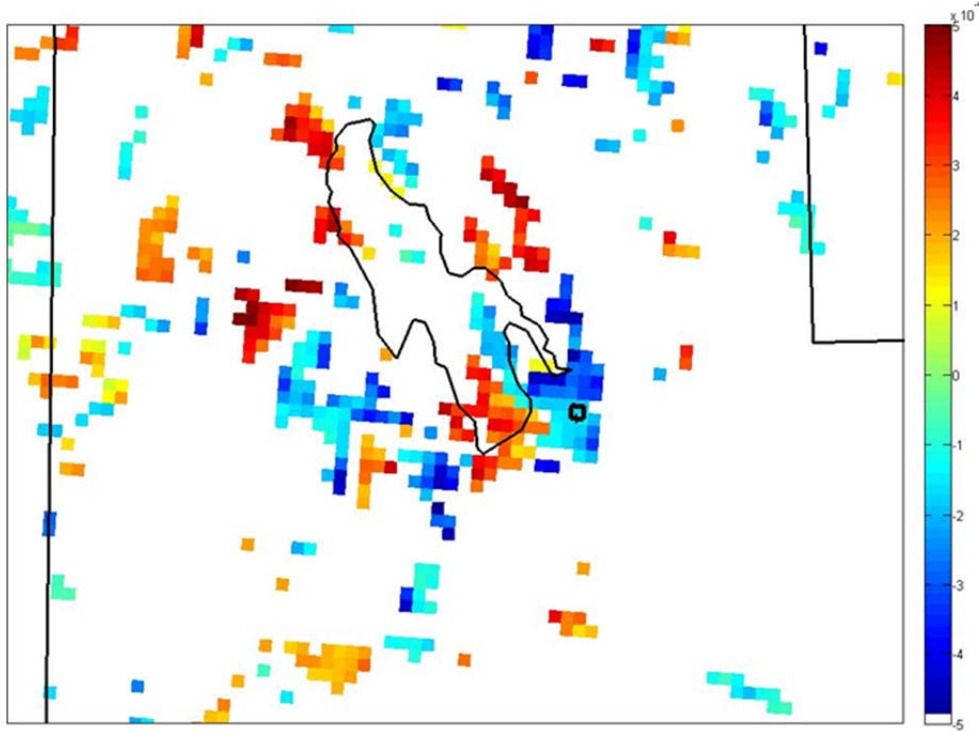


Figure 26. Sensitivities ( $dJ/dx$ ) using 1500 UTC 23 January u-component analysis winds ( $ms^{-1}$ ) (x) and forecasted  $Q_v$  (J) ( $kg\ kg^{-1}$ ) valid at 0000 UTC 24 Jan 2009. Units are  $kg\ kg^{-1}$  per  $m\ s^{-1}$ .

### 3. Statistical Linearity

To determine the length of the ESA approximations, the analysis must be pushed back in time to produce longer forecasts. However, the wind shift limited the length of the forecast using the 1800 UTC 23 January analysis and put limits on testing and determining the statistical linearity. To maneuver around this obstacle we decided to continue to use the 1800 UTC 23 January analysis but push the forecast further into the fog event. This would allow us to draw conclusions using a 9 hr and 12 hr forecast. To achieve this result, the forecasts valid 0300 UTC 24 January and the 0600 UTC 24 January were used for J instead of the forecast valid 0000 UTC 24 January.

### a. Nine-Hour Forecast

Figure 27 represents the results from the ESA using the 9-hr forecast ending at 0300 UTC 24 January. The sensitivities are similar to the 6-hr forecast suggesting that the statistical linearity of the analysis holds up through at least nine hours for this event using the u-component wind as  $\mathbf{x}$  and  $Q_v$  as  $J$ . The 9-hr forecast also interprets the area where the moisture is advecting off the lake, labeled as region 1 as an area of strong positive sensitivities. This region represents an area of positive sensitivities where a  $\pm 0.07 \text{ m s}^{-1}$  ( $1\sigma_u$ ) change in u-component winds will lead to  $\pm 1.309 \times 10^{-5} \text{ kg kg}^{-1}$  change in the 9-hr  $Q_v$  at the airport. The strong negative sensitivities northwest of the lake labeled as region 2 also show up using a 9-hr forecast. A  $\pm 0.06 \text{ m s}^{-1}$  ( $1\sigma_u$ ) change in the u-component analysis winds in the region northwest of the lake will lead to a  $\mp 1.305 \times 10^{-5} \text{ kg kg}^{-1}$  change in the 9-hr  $Q_v$  at the airport.

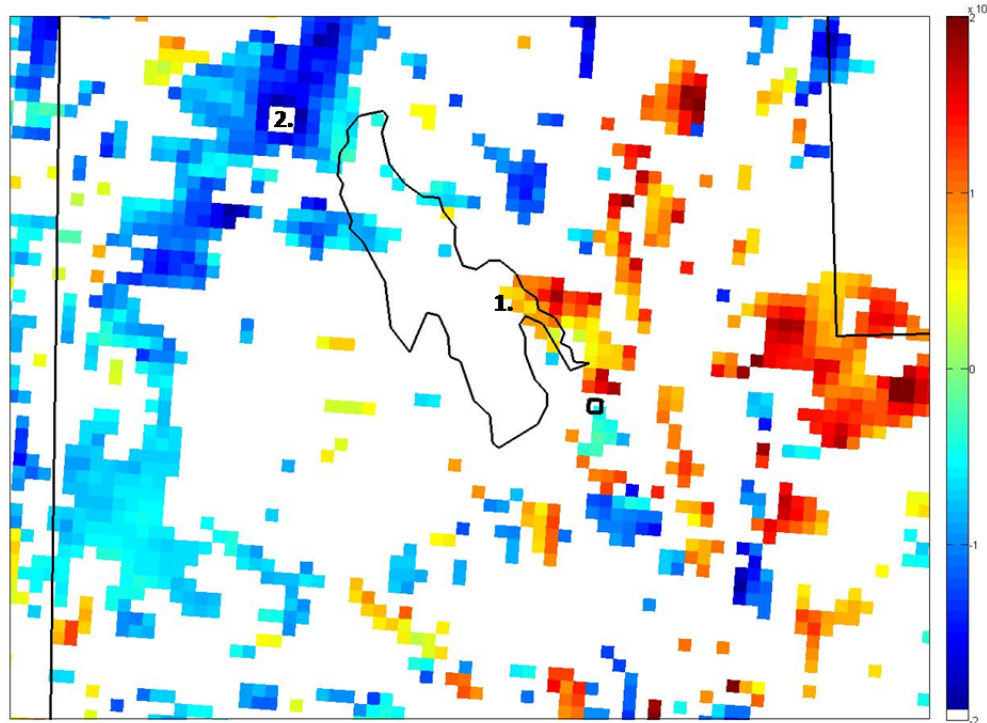


Figure 27. Sensitivities ( $dJ/dx$ ) using 1800 UTC 23 January u-component analysis winds ( $\text{ms}^{-1}$ ) ( $\mathbf{x}$ ) and forecasted  $Q_v$  ( $J$ ) ( $\text{kg kg}^{-1}$ ) valid at 0300 UTC 24 Jan 2009. Units are  $\text{kg kg}^{-1}$  per  $\text{m s}^{-1}$ .

### b. Twelve-Hour Forecast

Figure 28 is the sensitivities calculated using the 1800 UTC 23 January analysis and a forecast valid 12-hrs later. Most of the sensitivities failed the confidence interval test throughout the domain at this time and have been masked leaving only the positive sensitivities in region 1. This region is slightly south of where the plume of moisture was advecting off the lake and into the Salt Lake City region. Changing the u-component analysis winds by  $\pm 0.17 \text{ m s}^{-1}$  ( $1\sigma_u$ ) here will lead to a  $\pm \sigma 1.651 \times 10^{-5} \text{ kg kg}^{-1}$  change in  $Q_v$  over the airport 12-hrs later.

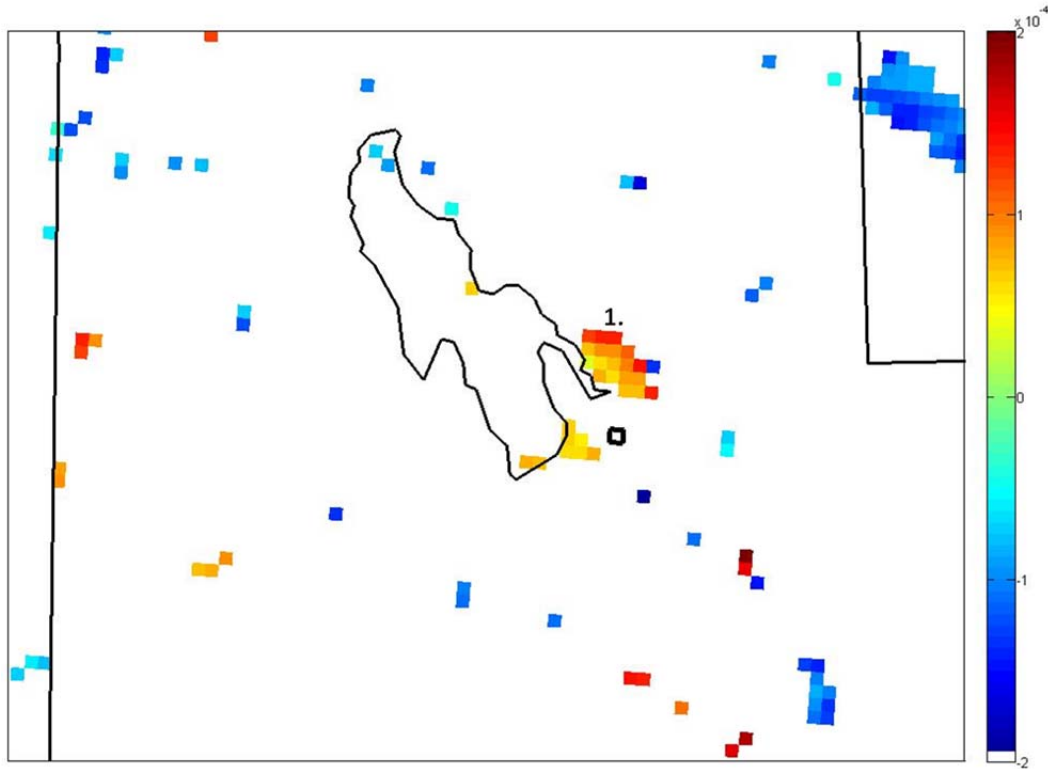


Figure 28. Sensitivities ( $dJ/dx$ ) using 1800 UTC 23 January u-component analysis winds ( $\text{ms}^{-1}$ ) (x) and forecasted  $Q_v$  (J) ( $\text{kg kg}^{-1}$ ) valid at 0300 UTC 24 Jan 2009. Units are  $\text{kg kg}^{-1}$  per  $\text{m s}^{-1}$ .

Since all model runs end at 0600 UTC 24 January the 12-hr forecast is the longest test of statistical linearity possible using the 1800 UTC 23 January analysis. At 12 hours most sensitivities have correlations with associated p-values of  $>0.05$  that fail the interval test. However, some of the strongest sensitivities still remained valid at this time period

leading to the assumption that for this particular fog event, mesoscale ensemble sensitivities can be approximated out to roughly 12 hours for the strongest regions of sensitivities using 4 km horizontal grid spacing with 96 members. This allows conclusions to be drawn approximating that the statistical linearity holds up though this time. This conclusion is a generality and to obtain a more accurate estimated time length more case studies would be required and analyzed.

#### 4. Linear Correlation

Figures 29–31 are scatterplots for all 96-members showing the 1800 UTC 23 January u-component analysis values,  $x_i$  and its associated forecasted  $Q_v$ , J for a particular sensitivity region. The scatterplots can be visually interpreted and allow easy examination of features in the data such as trends, clustering and changes in spread (Wilks 2006). The correlation coefficient, labeled as  $r$  in the plot indicates the strength of the linear relationship between two variables (Wilks 2006). The sensitivity value computed at the same location  $dJ/dx_i$  is also shown. All sensitivities and correlations displayed in the scatterplots are taken from the strongest area of sensitivities in the region where the low-level moisture was advecting off the lake approximately 13 miles north of the airport. The latitude and longitude of the exact location where  $x_i$  was taken from is shown in the x-axis of the table.

Figure 29 is the 6 hr forecast and its scatterplot visually suggests a tight spread in the values with a good positive trend at 41.1°N, -112.2°E. The associated coefficient value of 0.62 quantitatively indicates a strong linear correlation and there are few outliers indicating a good linear relationship. Figure 30 is the 9-hr forecast at 41.1°N, -112.1°E and its scatterplot visually suggests added spread in the plot and a weaker linear correlation. The coefficient value of 0.34 quantitatively supports this weaker correlation estimation. Figure 31 is the 12-hr forecast at 41.1°N, -112.0°E and its scatterplot shows even more spread in the variables. This equates to slightly weaker positive linear correlation with an associated coefficient value of 0.27.

The scatterplots and associated correlation coefficients indicate that the 6-hr forecast has the strongest linear correlation for the region where the moisture was advecting off the lake. The 9 hr and 12 hr forecasts visually show increased spread in the plots and equates to weaker coefficient values. It can be concluded that the 6-hr forecast using the 1800 UTC 23 January analysis leads to best the ESA results supported by the strong linear correlation values.

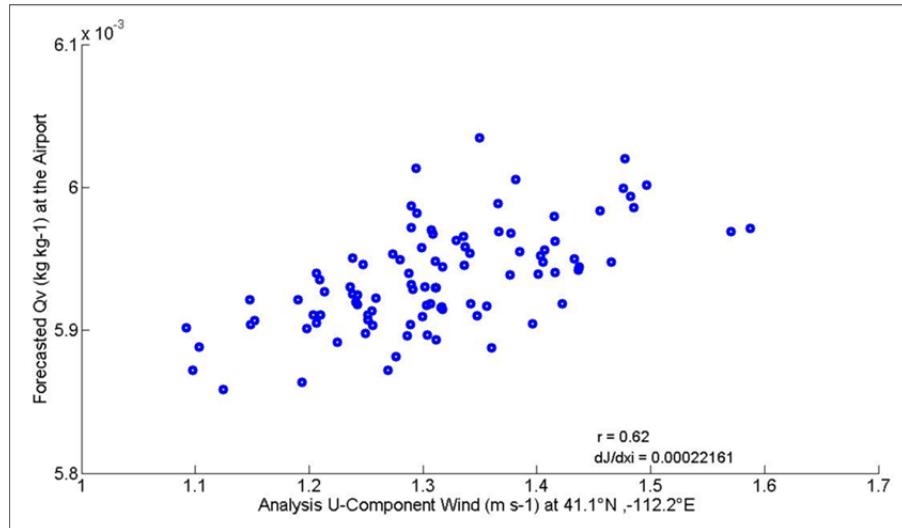


Figure 29. Scatterplot of 1800 UTC 23 January analysis u-component winds and forecasted  $Q_v$  at the airport at 0000 UTC 24 January

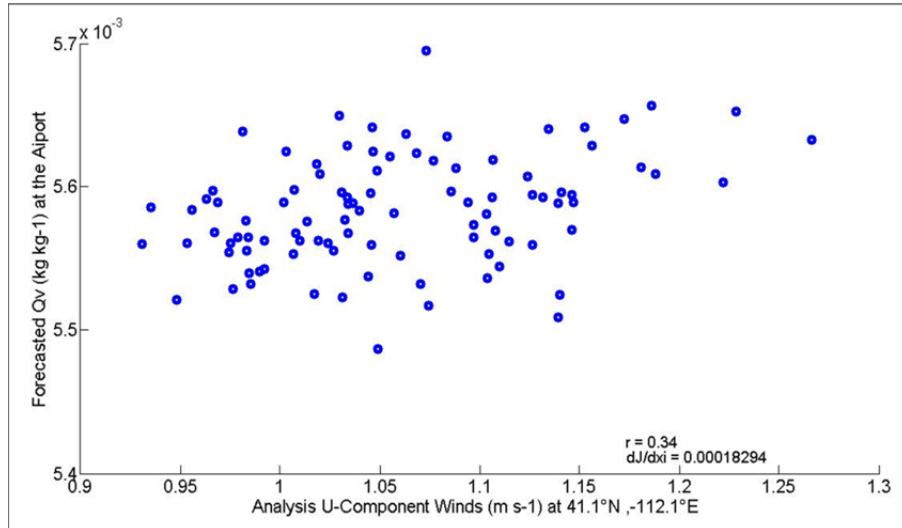


Figure 30. Scatterplot of 1800 UTC 23 January analysis u-component winds and forecasted  $Q_v$  at the airport at 0300 UTC 24 January

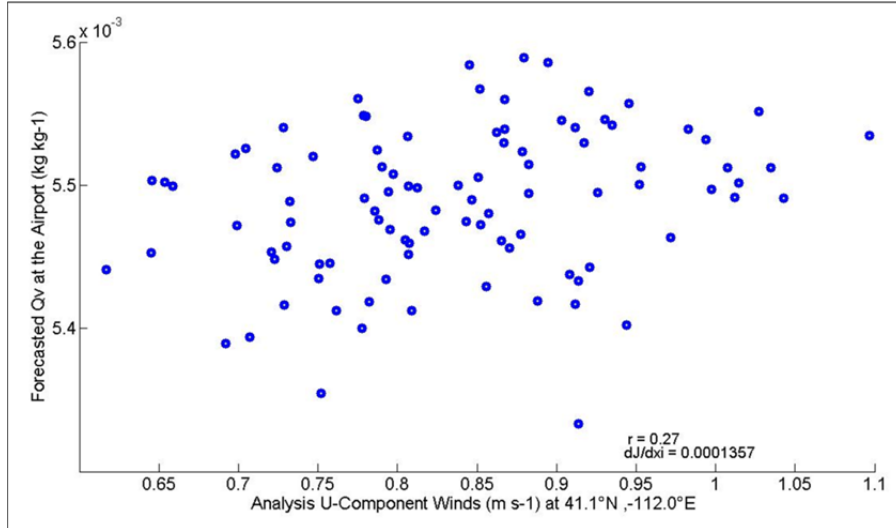


Figure 31. Scatterplot of 1800 UTC 23 January analysis u-component winds and forecasted  $Q_v$  at the airport at 0600 UTC 24 January

## D. TESTING THE LINEARITY

### 1. Testing the 1800 UTC 23 January Sensitivity-Analysis Predictions

An additional piece of determining the validity of the linear assumption of the ESA included testing the linearity of the sensitivity-analysis predictions. In order to test the sensitivity-analysis predictions a series of tests were performed that made perturbations to the analysis and then were integrated forward to determine the changes to the  $Q_v$  at the airport. This can be interpreted as testing the statistical linearity over the sensitivity interval. Using results from the ESA, point locations of strong and meaningful sensitivities at individual grid points were identified. To test the 1800 UTC 23 January analysis predictions using the 6-hr forecast, perturbations of  $-3\sigma_u$ ,  $-2\sigma_u$ ,  $-1\sigma_u$ ,  $+1\sigma_u$ ,  $+2\sigma_u$  and  $+3\sigma_u$  were made to  $u$  at grid point  $x = 133$ ,  $y = 97$  ( $41.1^\circ\text{N}$ ,  $-112.2^\circ\text{E}$ ), the location where the moisture advected off the lake. At  $41.1^\circ\text{N}$ ,  $-112.2^\circ\text{E}$ ,  $1\sigma_u$  equals  $0.09 \text{ m s}^{-1}$ . In order to ensure a balanced analysis after the perturbations were made at the first  $\eta$ -level, a series of linear regression equations were applied to all model variables at all vertical and horizontal grid points. The initial perturbation of the mean field is a linear regression of a single point perturbation on the model field using the ensemble analysis statistics. Following Reinecke (2008) and Torn and Hakim (2009) the ensemble-mean perturbation to each  $i^{th}$  analysis state variable can be written as:

$$x_i^p = x_i^a + \frac{\text{cov}(x_i^a, x_s^a)}{\sigma_{x_s}^2} \sigma_{x_s} \alpha$$

$x_i^a$  = analysis variable (member of ensemble)

$x_s^a$  = analysis variable at a sensitivity point

where the analysis-error covariance matrix,  $x^a$  is added to the linear regression of the analysis-error covariance matrix and the scalar perturbation made at the individual grid point for all  $i$ -state variables. The perturbation amplitude to  $\sigma_s$  is represented by  $\alpha$  and for this project  $\alpha$  can equal -3, -2, -1, 1, 2 or 3. Figure 32 shows,  $x^p - x^a$ , the results of the  $+0.09 \text{ m s}^{-1}$  perturbation of u-component winds at  $41.1^\circ\text{N}$ ,  $-112.2^\circ\text{E}$  at the first  $\eta$ -level after being regressed into model to make a new set of initial conditions. What is shown in the figure is essentially the new analysis minus the original analysis, at the first  $\eta$ -level. The region of strong positive perturbations in the eastern region of the lake is the grid point where  $u$  was perturbed by  $+0.09 \text{ m s}^{-1}$ . The strongest perturbation shown in the figure is not the actual grid point perturbed but a grid point to the west where the  $u$ -wind was strengthened more by the regression. In addition, the regression perturbs the winds in other locations including strengthening the northeast winds in the region northwest of the lake. Also, the easterly winds were strengthened south of the airport as the wind pushed down the front range of the Wasatch Mountains and ejected back to the west. After drawing conclusions based on these locations of perturbations with respect to the location of the original perturbation it is determined that these regressed perturbations make conceptual sense and are quantitatively supported by the results from the ESA.

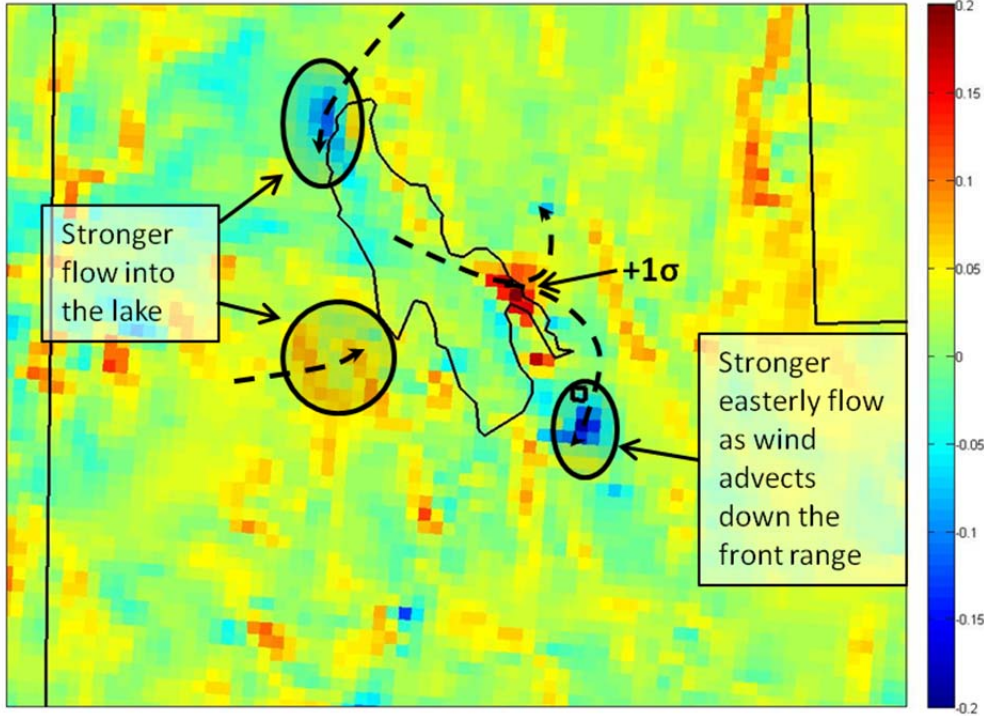


Figure 32. The  $+1\sigma$  perturbation applied at  $41.1^{\circ}\text{N}$ ,  $-112.2^{\circ}\text{E}$  at the first  $\eta$ -level in  $\text{m s}^{-1}$  after being regressed throughout the model.

Perturbing u-winds by  $+1\sigma$  at  $41.1^{\circ}\text{N}$ ,  $-112.2^{\circ}\text{E}$  at the first  $\eta$ -level causes some interesting features when looked at the regressed perturbations vertically. Figure 33 displays the vertical changes to the u-component wind throughout all  $\eta$ -levels when a  $+1\sigma$  perturbation is made at the surface and regressed throughout all levels of the analysis. Note how the perturbation becomes negative between the third and fourth  $\eta$ -level then switches back to positive at the fifth  $\eta$ -level suggesting that stronger u-component winds at the surface equate to weaker u-component winds directly above. This represents a strengthened low-level inversion and shown in Figure 34 where temperature perturbations are plotted through vertical. Note in Figure 34 where the regression actually leads to cooler temperatures at the surface and warmer temperatures at the levels directly above. A strengthened inversion translates to stronger flow off the lake and more moisture at the airport.

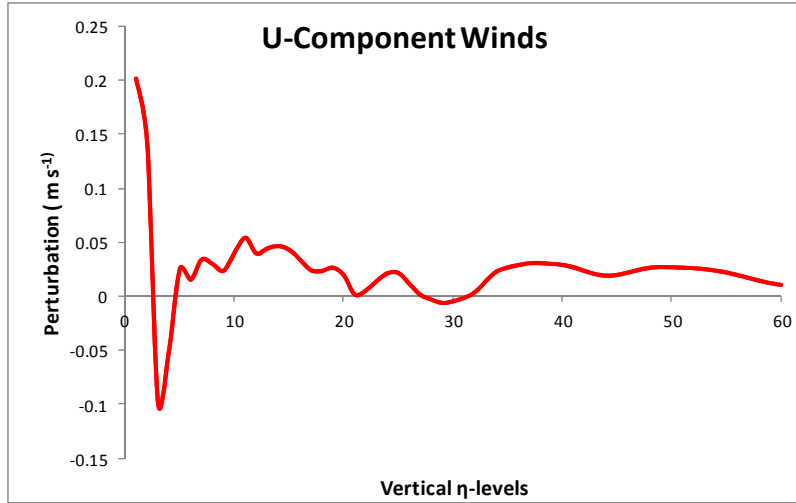


Figure 33. Changes to the u-component wind ( $\text{m s}^{-1}$ ) throughout the vertical at  $41.1^\circ\text{N}$ ,  $-112.2^\circ\text{E}$  after regressing a  $+1\sigma$  perturbation at the surface.

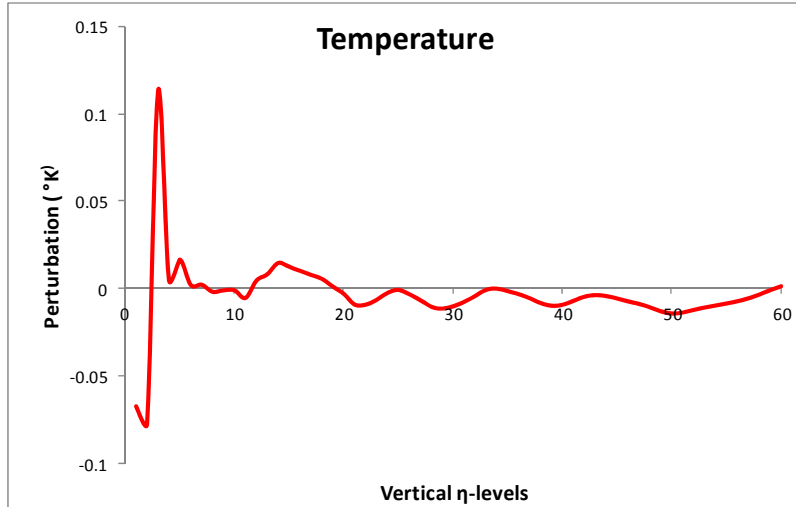


Figure 34. Changes to temperature throughout the vertical at  $41.1^\circ\text{N}$ ,  $-112.2^\circ\text{E}$  after regressing a  $+1\sigma$  perturbation in the u-component winds at the surface. The profile suggests a strengthened inversion.

After regression the new perturbed analyses are integrated forward and new “perturbed” ensemble runs are created. Using the new perturbed 1800 UTC 23 January analyses and the forecast valid at 0000 UTC 24 January a new  $Q_v$  value was calculated for the J box at the airport for each new perturbed forecast. The new  $Q_v$  value was then

compared to the predicted value determined by the original ESA results. To determine the value of  $Q_v$  predicted by the ESA the sensitivities must be in units of  $\text{kg kg}^{-1}$ . It is determined that making a  $0.09 \text{ m s}^{-1}$  change in the analysis u-component winds at  $41.1^\circ\text{N}$ ,  $-112.2^\circ\text{E}$  leads to a  $2.197 \times 10^{-5} \text{ kg kg}^{-1}$  change in  $Q_v$  in the J box over the airport 6 hrs later. This predicted change is then multiplied by  $\alpha$  to get the new predicted  $Q_v$  values for each perturbation magnitude. The values are then compared to the actual values from the new perturbed model runs.

To examine the validity of the ESA, the predicted values are plotted against the actual values. Figure 35 visually displays the linearity of the prediction where the diagonal line represents a perfectly linear response. The ESA predicted response does accurately capture the sign of the actual perturbed response but the magnitudes of the response are over estimated. The actual perturbed responses that fall below the line indicate that the magnitude of the WRF response is less than the prediction. The opposite is true for  $\alpha$ -perturbations that fall above the line. For  $\alpha$ -perturbations  $< 2$  the actual change is less than the predicted change and for  $\alpha$ -perturbations  $> 2$  the actual change is more than the predicted change. When compared to the line the actual values are fairly linear but become increasingly non-linear after  $\alpha$ -values  $-2$  and  $+2$ . Additionally, the positive and the negative perturbations are comparatively symmetric suggesting that the error growth dynamics for this mesoscale fog event are linear.

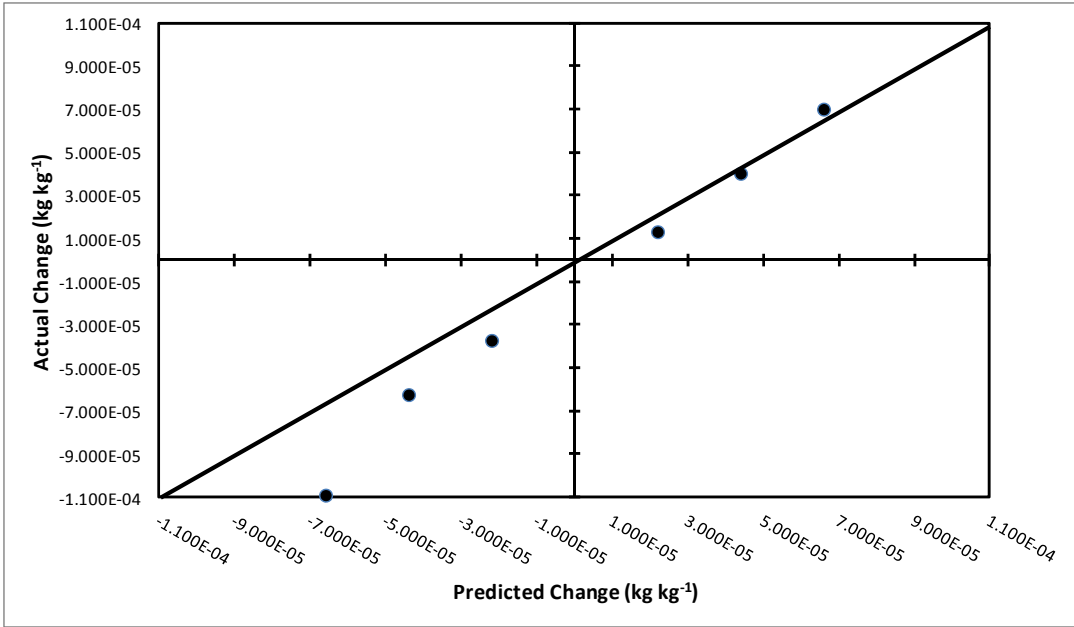


Figure 35. Actual change in  $Q_v$  versus predicted change in  $Q_v$  for each  $\alpha$ -value perturbation using the 1800 UTC 23 January analyses. The line represents a perfectly linear response.

Figure 36 also illustrates the results from the analysis-prediction tests. The dashed line is the predicted values determined by the results of the ESA and the solid line is a linear fit of the actual values. These values are plotted for each alpha value. Notice how the actual line is steeper than the predicted values suggesting that the actual values are over estimated for both the positive and negative perturbations.

A possible reason for the over-forecast is from the sampling error within the analysis. When estimating spatial covariances or perturbations and there is sampling error, the tendency is to over-estimate initial perturbations throughout the analysis. These larger perturbations are reflected in the over-prediction of the responses and can be better shown in Figure 36 with the steeper actual line. Perturbations are applied to the analysis to make a new perturbed analysis to be integrated forward. Due to ensemble statistics, regression spreads these perturbations throughout the entire analysis, even at very far distances. Even though the perturbations are linearly related, physically they may not be. Sample statistics will over-estimate the slope of the covariances regression line due to the

sampling error. This means when the actual runs are created the perturbations made are too large. To account for this over-prediction, covariance localization could be applied in the data assimilation process. Localization of the covariances will damp the perturbations to zero at some distance away from the original perturbation. This means that all perturbations at some distance will be smaller than the original perturbation and eventually the analysis will be unperturbed at a certain distance. This is to account for the fact that at further distances away from the original perturbation the effect of the sampling error gets worst. Localization of the covariances was not completed in this study and this would be the best reasoning for the over estimation of the  $Q_v$  values from new perturbed runs.

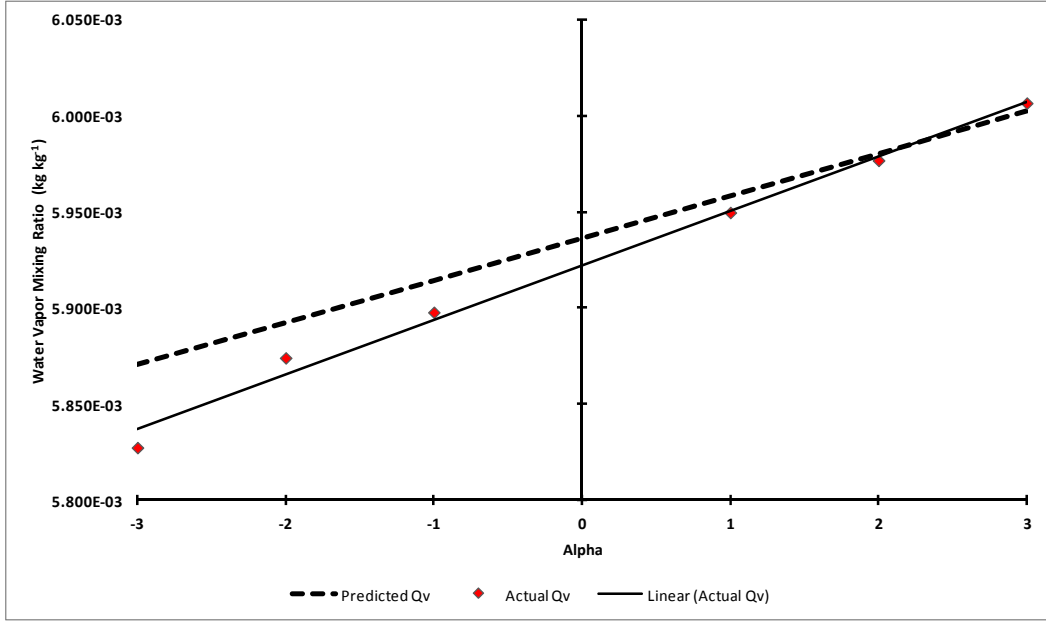


Figure 36. Plot of actual  $Q_v$  from the alpha perturbed ensembles (black line) versus the predicted  $Q_v$  taken from the ESA results (dashed line) for 1800 UTC 23 January. Units are  $\text{kg kg}^{-1}$ .

## 2. Testing the 1500 UTC 23 January Sensitivity-Analysis Predictions

The same series of sensitivity-analysis prediction tests were performed on the 1500 UTC 23 January analysis and a forecast valid nine hours later at 0000 UTC 24 January. The intent in performing these tests was to determine if the

linearity of the model dynamics would remain valid through the wind shift that occurred at 1700 UTC 23 January. The results of the linearity tests would help solidify the hypothesis that the ESA approximations do not hold true through the wind shift in surface winds for this fog event.

From sensitivities shown in Figure 26, perturbations of  $-3\sigma_u$ ,  $-2\sigma_u$ ,  $-1\sigma_u$ ,  $+1\sigma_u$ ,  $+2\sigma_u$  and  $+3\sigma_u$  were made to  $u$  at grid point  $x = 132$ ,  $y = 87$  ( $40.77^\circ\text{N}$ ,  $-112.23^\circ\text{E}$ ), the location of strong positive sensitivities directly to the west of the airport. At  $40.77^\circ\text{N}$ ,  $-112.23^\circ\text{E}$ ,  $1\sigma_u$  equals to  $0.12 \text{ m s}^{-1}$ . Results from the ESA show that perturbing  $u$  by  $+0.12 \text{ m s}^{-1}$  at this point equates to a forecasted change in  $Q_v$  of  $4.585 \times 10^{-5} \text{ kg kg}^{-1}$  9-hrs later at the airport.

To examine the validity of the ESA, the predicted values are plotted against the actual values. Figure 37 visually displays the linearity of the prediction where the diagonal line represents a perfectly linear response. Note the non-linearity in the responses for all perturbations. The actual perturbed responses that fall above the line indicate that the magnitude of the WRF response is more than the prediction. All responses are much greater than the predicted value except for  $-2\sigma_u$  perturbation. Figure 38 also illustrates the non-linearity in the results from the analysis-prediction tests. The black solid line represents a best fit of all the actual perturbed values highlighting the non-linearity in the results. In addition, note how all values except for the  $-2\sigma_u$  perturbation fall above the line indicating how the results are much greater than the predict values.

The sensitivity-analysis predictions for the 1500 UTC 23 January analysis can be considered non-linear after the linearity perturbation tests were performed. The wind shift that occurred at 1700 UTC 23 January fell between the analysis and the 0000 UTC 24 January forecast. It is determined that this wind shift caused the non-linearity in the dynamical responses once the perturbations were applied. This leads to the assumption that the linear relationships within this ESA do not hold up through a shift in the winds when using low-level winds as  $\mathbf{x}$  and  $Q_v$  for  $\mathbf{J}$ .

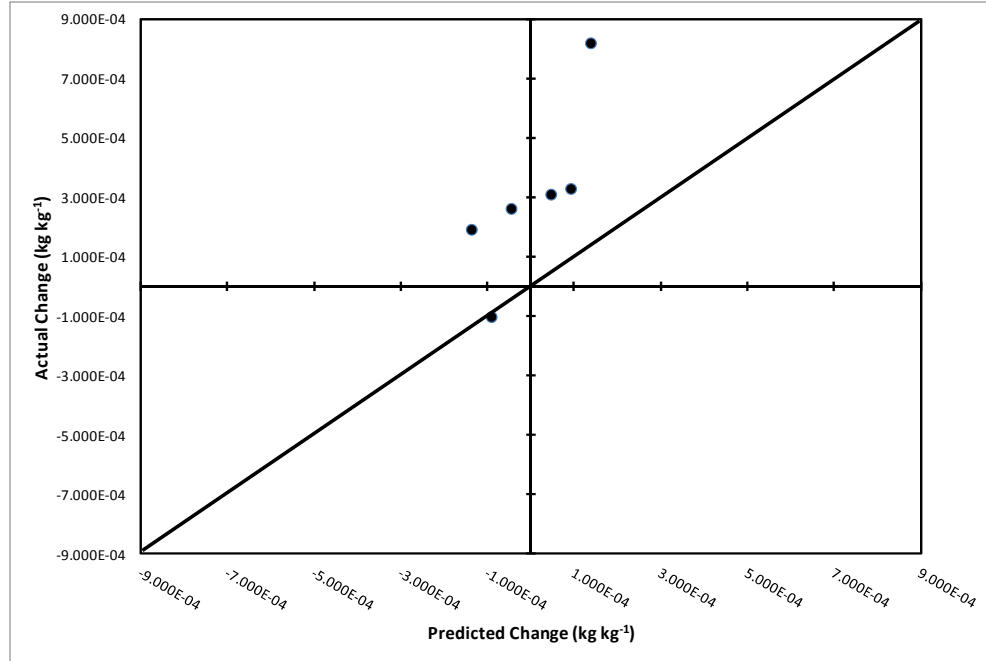


Figure 37. Actual change in  $Q_v$  versus predicted change in  $Q_v$  for each  $\alpha$ -value perturbation using the 1500 UTC 23 January analyses. The line represents a perfectly linear response. Units are  $\text{kg kg}^{-1}$ .

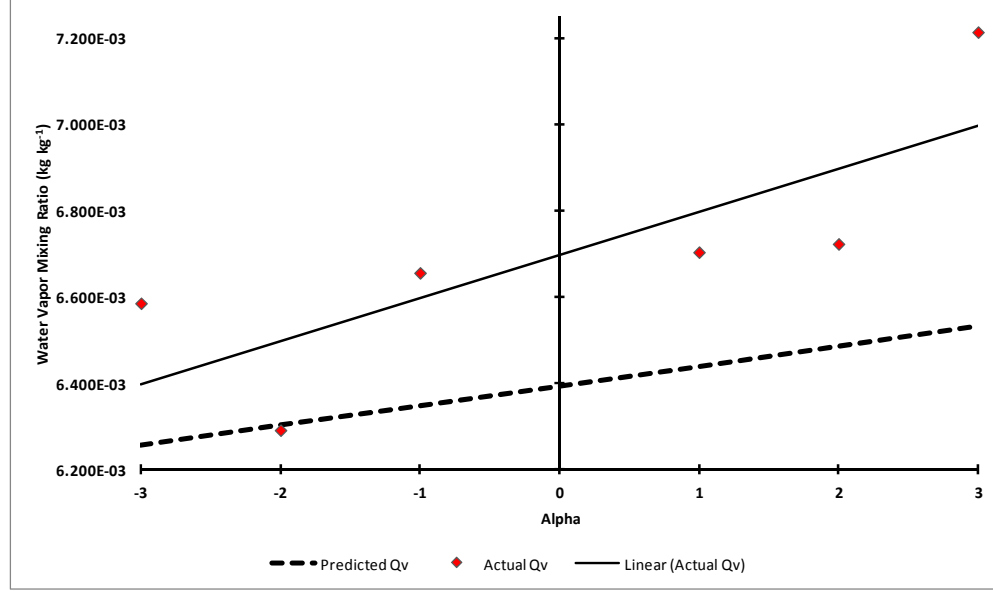


Figure 38. Plot of actual  $Q_v$  from the alpha perturbed ensembles (black line) versus the predicted  $Q_v$  taken from the ESA results (dashed line) for 1500 UTC 23 January. Units are  $\text{kg kg}^{-1}$ .

### 3. Sensitivity-Analysis Prediction conclusions

Results from the 1800 UTC 23 January analysis suggest that the model dynamics remain linear through small perturbations in the analysis. Once the perturbations become large,  $>\pm 2\sigma_u$  the results become non-linear. There was also inaccuracy in the actual magnitude when compared to the predicted values determined from the ESA. It can be assumed that these magnitude errors can arise by sampling error which leads to over estimation of the covariances throughout the analysis. Localization applied during data assimilation could account for the errors and lead to more accurate actual perturbed values.

Results from the 1500 UTC 23 January analysis suggest that the model responses do not remain linear through the perturbations in the analysis. This non-linearity in the results suggests that that linear ESA assumptions to do not hold true through the 1700 UTC 23 January wind shift that occurs between the analysis and the forecast. For this reason, the 1800 UTC 23 January analysis is the earliest analysis that can be used within the ESA.

### E. ENSEMBLE SIZE

An additional research objective for this project includes testing the ESA using a number of different ensemble sizes and drawing conclusions based on these convergence studies. The main goal is to approximate how many ensemble members are needed to accurately and robustly obtain useful sensitivities. Using the minimum number of ensembles in an ESA will reduce computation costs which is normally an essential factor in numerical modeling. In addition, narrowing the number of ensembles is a critical piece when determining if an ensemble system that is already operational can be used to produce useful sensitivities.

The number of members required can be estimated by rerunning the ESA using a reduced ensemble size. Conclusions can be drawn based on correlation/sensitivity values and associated sampling errors. Starting at 96-members the ESA was executed using a random selection for 90, 80, 70, 60, 50, 40, 30, 20, 15, 10 and 5 ensembles members.

However, to attain the most accurate results we would need to re-run DART each time with a fewer number of ensembles and then rerun the ESA. Due to time constraints for this project we were unable to create new model runs. The results discussed here could be further hardened with new models but for the purpose of this research we will consider these results as a lower bound. This means that the estimated number of ensembles needed to produce useful sensitivities will be considered a worst case scenario.

### **1. Testing the Positive Sensitivities at a Single Point**

Figure 39 is a series of images of the computed sensitivities as the ensemble size is reduced. The sensitivities were calculated using the 1800 UTC 23 January u-component winds for  $x_i$  and  $Q_v$  as J at the airport valid six hours later at 0000 UTC 24 January. Note how the sensitivities at “X” (41.1°N, -112.2°E), the region where the moisture advects off the lake, change as the members are reduced from 96 to 5. The positive sensitivities remain steady until the members are reduced to less than 30. At 10 members and below the sensitivities are completely masked as the correlations fail the 95% confidence interval test due to the small sampling size.

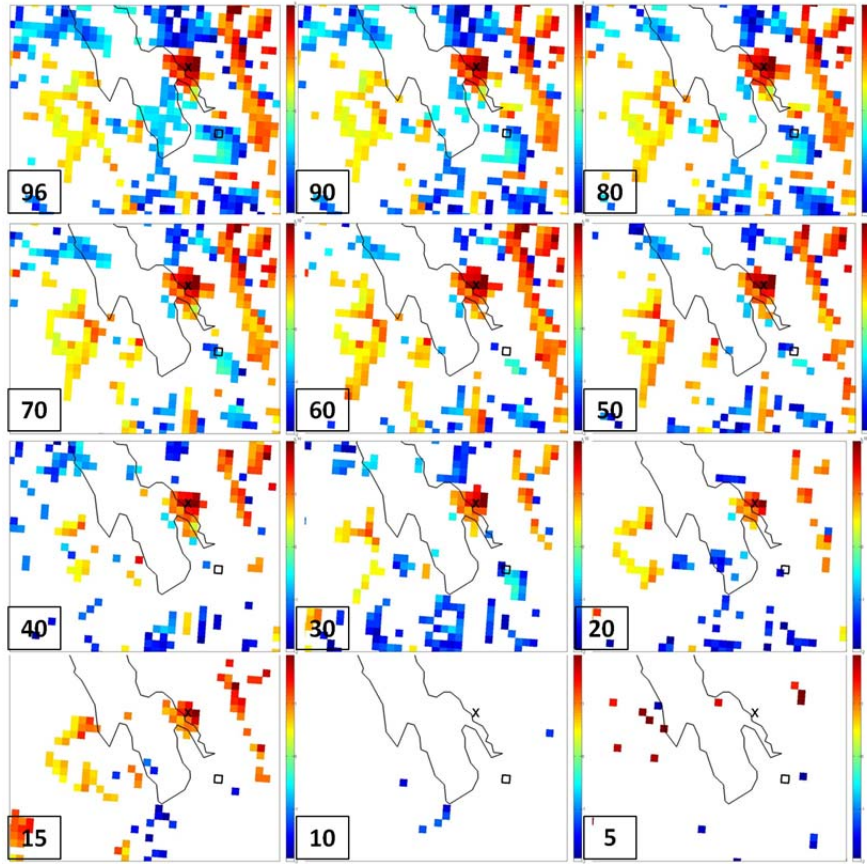


Figure 39. Change in 1800 UTC 23 January sensitivities at “X” as the number of ensembles are reduced from 96 to 5 members.

Figure 39 is the scatterplots associated with each of the images in Figure 39. The scatterplots although small in this paper are only needed to visually depict how the linearization and scattering of the variables change as the ensemble size is reduced. The x-axis represents the 1800 UTC 23 January analysis u-component winds at the “X” ( $41.1^{\circ}\text{N}$ ,  $-112.2^{\circ}\text{E}$ ), and it’s associated forecasted  $Q_v$  at the airport six hours later valid 0000 UTC 24 January is plotted on the y-axis. It can be estimated that as the ensemble size is reduced the sampling errors associated with the correlations must increase. This increased sampling error can be assumed and be easily portrayed once the ensemble size is reduced to 15 members or less due to the lack of data points.

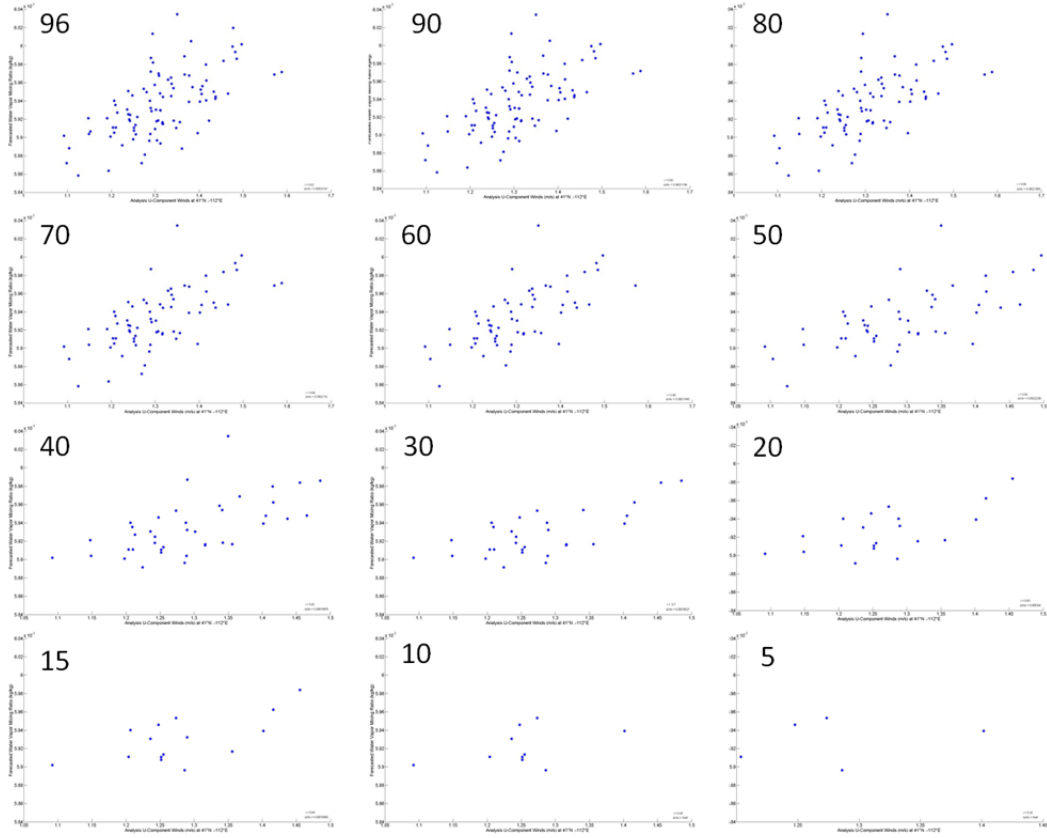


Figure 40. Scatterplots of analysis u-component winds and forecasted  $Q_v$  used in the ESA as the ensemble size is reduced from 96 down to 5 members. The x-axis represents the 1800 UTC 23 January analysis u-component winds at the “X” (41.1°N, -112.2°E) and its associated forecasted  $Q_v$  value six hours later valid 0000 UTC 24 January is plotted on the y-axis.

The upper and lower boundaries obtained from testing the correlation values using the 95% confidence interval test were used to represent the ESA sampling error. Large upper and lower bounds equate to large sampling error. Figure 41 is a chart of correlation values in red and associated sensitivity values in blue verses the number of ensembles at the individual point labeled as “X” (41.1°N, -112.2°E) in Figure 39. The green bars are the upper and lower boundaries of the 95% confidence interval representing the sampling error associated with each ensemble size. It can be concluded that for this particular event the correlation coefficient values, the sensitivities and the sampling error remain for the most part the same when reducing the ensemble size from

96 to 40 members. Once reduced to fewer than 40 members the sensitivities begin to decrease rapidly. The correlation values remain approximately the same through 15 members but the sampling error grows rapidly once the ensemble size is reduced to less than 30 members. Once the ensemble size is reduced to less than 15 the sampling errors became large and the sensitivities are masked due to associated p-values that are  $>0.05$ . For visual representation and comparison the sensitivity values were added to the chart. When reduced to less than 15 members the upper and lower bounds become large suggesting that the sampling errors are so large that the probabilities of getting a correlation as large as the observed value are almost the same as if it was random. At five members the upper and lower boundaries of the correlation confidence test range from 0.92 to -0.81, roughly meeting the limits of 1.0 to -1.0.

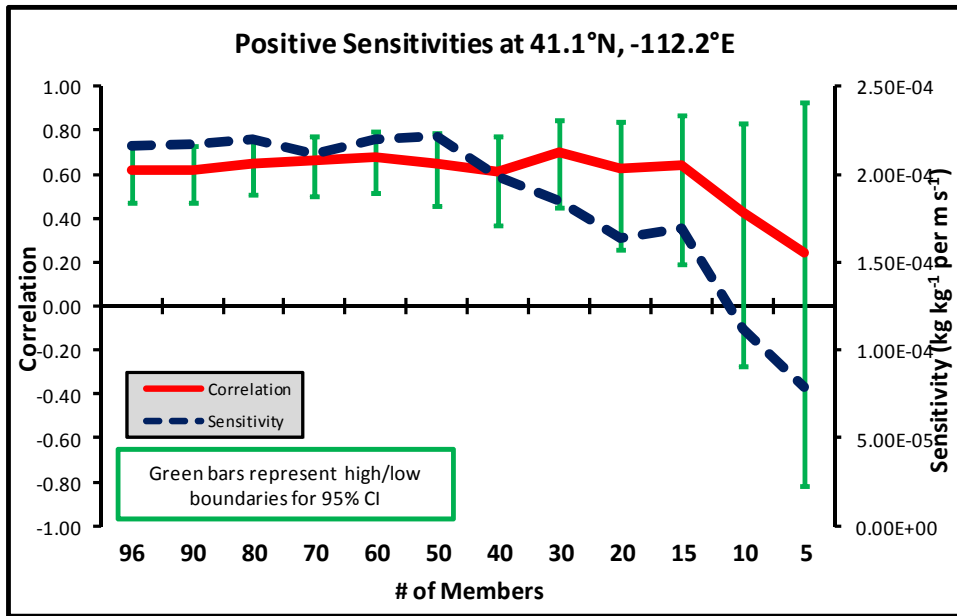


Figure 41. Chart of correlation in red and sensitivity in blue versus the number of ensemble members for a single point of positive sensitivities at 41.1°N, -112.2°E. The green bars are the high and low boundaries of the 95% confidence interval and represent the associated sampling error.

## 2. Testing the Negative Sensitivities at a Single Point

The same tests were performed for a single point ( $41.6^{\circ}\text{N}$ ,  $-113.2^{\circ}\text{E}$ ) of negative sensitivities for the region northwest of the GSL. This is the region where the northeast winds push down the valley and drain into the lake. Recalculating the sensitivities in this region after reducing the ensemble size leads to the results plotted in Figure 42. Since the correlations and the sensitivities are negative the plot is opposite but the results are similar to the positive sensitivities. The sampling errors remain fairly similar through 30 members but when reduced to fewer than 30 members sensitivities quickly decrease and the sampling errors increase. At 15 members, the p-values become too large and the correlations fail the interval test but for visualization purposes are still plotted in the chart. For the negative sensitivities northwest of the lake it can be concluded that fewer than 30 members are required to obtain useful and meaningful sensitivities.

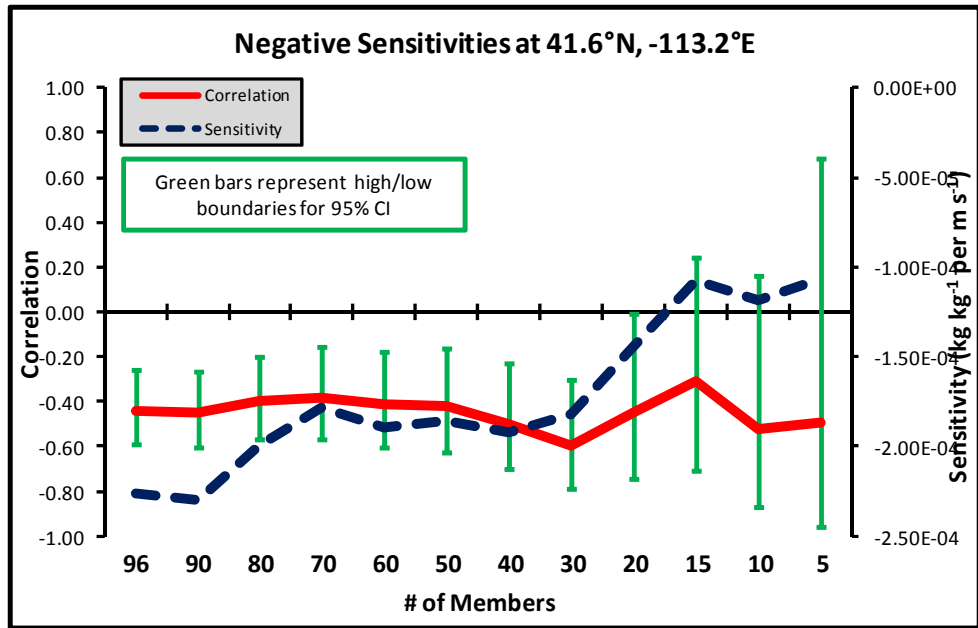


Figure 42. Chart of correlation in red and sensitivity in blue versus the number of ensemble members for a single point of negative sensitivities at  $41.6^{\circ}\text{N}$ ,  $-113.2^{\circ}\text{E}$ . The green bars are the high and low boundaries of the 95% confidence interval and represent the associated sampling error.

### **3. Ensemble Size Summary**

It can be summarized that for this particular fog event that 30 to 40 ensembles members is the minimum number of members needed to skillfully determine the sensitivity of forecasted fog. This number was determined by simply averaging the results from both tested regions. ESAs using fewer than 30 members lead to weaker sensitivities and large sampling errors. ESAs using fewer than 15 members have severe sampling errors and sensitivities that are masked due to the associated p-values being too large to meet the interval test. After discussion among the field it is believed that to achieve the most accurate results, DART would need to be re-run and new models created with fewer ensemble members. For the purpose of this research, 30 will be considered the lower bounds and the minimum members needed. Further research may indicate that even a smaller number of ensemble members can be used to produce useful and meaningful sensitivities. Note that the results presented here are for this particular case study only and the generality is still not entirely known.

THIS PAGE INTENTIONALLY LEFT BLANK

## V. CONCLUSIONS AND FUTURE WORK

This study evaluated mesoscale ensemble sensitivities in an area of complex terrain. Using a 96-member ensemble system at 4 km horizontal resolution an ESA was performed for a dense fog event that occurred at the SLC International Airport in January 2009. Post-analysis of the ESA revealed that the lowest model level wind analysis provided the most useful data to skillfully determine the sensitivity of forecasted fog in this mountainous region for this study. The sensitivities quantitatively matched our conceptual model thus providing useful feedback in the determination of the accuracy and usefulness of this ESA.

The 1800 UTC 23 January analysis paired with a forecast valid six hours later led to the most useful and meaningful sensitivities. It was determined that the low-level u-component winds versus the v-component winds had a greater impact in advecting the cold moist air off the GSL and into the city. The low-level winds led to sensitivity results that made physical sense but led to a definite drawback. A wind shift in the low-level winds that occurs between the analysis and the forecast will clearly lead to different sensitivities. For example, if a wind shift occurs between two analyses the sensitivities obtained using the same forecast valid time may appear very different. Testing an analysis before and after the wind shift proved that the ESA approximations become non-linear when a wind shift occurs between the analysis and the forecast when using low-level winds for  $\mathbf{x}$ . Finally, it can be concluded that a wind shift can alter the effectiveness of a mesoscale ESA for surface fog event and must be considered.

Climatology combined with a conceptual model reveals that winds from the northwest tend to advect moisture off the lake and into the SLC Basin. However, the ESA results from this particular fog event reveal that northeast winds located just to the northwest of the lake filter into the lake through the valleys. Eventually, the winds channel into the lake basin and eject out of the lake through the areas of low terrain approximately 13 miles north of the airport. There may be additional meteorological phenomena that contribute to the region of strong positive sensitivities in area where the

moisture advected off the lake. Afternoon temperatures became warm the three hours before the fog event leading to a strong temperature gradient between the land and the lake. A lake breeze could have developed as a result of the differential heating between the air over the lake and the land surrounding the lake and it has been determined that the ESA captured the location where it was most prevalent. There may be further meteorological phenomena that could have influenced the moisture advection off the lake including mountain and valley drainage into the lake.

The overall quantitative ESA results using the u-component winds are similar to the conceptual model presented earlier. These results may appear obvious but to have quantitative sensitivities that match what makes conceptual sense is significant and supports the speculation that a mesoscale ESA could be used to facilitate the prediction of fog in complex terrain.

The wind shift that occurred at 1700 UTC 23 January put statistical limits on the length of the forecasts used in the ESA. Since all forecast runs end at 0600 UTC 24 January this limited the time length of testing the statistical linearity out to approximately 12 hours for this particular case study. Without any longer forecasts it was estimated that for this fog event 12 hours is the approximate time length that the statistical equations remain valid at a 95% confidence interval. At the 12 hr forecast the majority of sensitivities have correlations with associated p-values of  $>0.05$  which fail the interval test. However, some of the strongest sensitivities still remained valid at this time period leading to the conclusion that for this particular fog event, the strongest mesoscale ensemble sensitivities can be approximated out to 12 hours.

To test the sensitivity-analysis predictions of the ESA a series of experiments were completed. A perturbation was applied to the region of maximum sensitivity to the original analysis and then regressed throughout all model states and grid points to come up with a new “perturbed” analysis. The analysis was then integrated forward in time and a new set of ensembles were created. Predicted  $Q_v$  determined from the ESA was then compared to the new actual values. Tests were performed on wind analyses before and after a wind shift. Using analyses before the wind shift led to perturbation dynamics

that were non-linear suggesting that the ESA approximations are not valid when a wind shift occurs between the analysis and the forecast. The tests on the analysis winds after the wind shift revealed that the model dynamics were linear but became increasingly non-linear with the larger perturbations through at least six hours. Additionally, the tests revealed that the ESA predicted response does accurately capture the signs of the actual responses but the overall magnitudes were over predicted. It is estimated that this over prediction is from the sampling error within the analysis and it is assumed that performing covariance localization on the new perturbed analysis would lead to better results. Even though the magnitudes of the responses were slightly off it still can be concluded that the ESA was a viable option in determining the sensitivities in this particular fog event.

In order to test the number of ensemble members required a series of tests were initiated that measured the correlations, sensitivities and the bounds of the 95% confidence interval for a single point of sensitivities. The sensitivities were recalculated for each reduction of the ensemble size from 96 to 5 members. It can be concluded that for this particular fog event at least 30–40 ensemble members are needed to accurately produce useful and meaningful mesoscale ensemble sensitivities. Mesoscale sensitivities calculated using fewer than 30 members led to increased sampling errors and weakened sensitivities and correlations. When using fewer than 15 members, the sampling errors became too large and the sensitivities failed the 95% confidence interval test. It is assumed that to achieve the most accurate results, DART would need to be re-run using a fewer number of ensembles. Then the ESA would be applied to these new models. For the purpose of this research, 30 ensembles will be considered the minimum number of ensemble needed but will serve as the lower bounds. Using the new models may prove that the actual number of members required is less. In addition, the results presented here are for this particular case study only and the generality is still not fully known.

## A. POTENTIAL NETWORK DESIGN

Using the methods presented in this project, we feel that a mesoscale ESA could be used to identify critical locations of sensitivities and these sensitivities could be used

in potential network design. Figure 43 identifies the regions of sensitivities that are determined to be the most influential in forecasting the amount of moisture received at the airport. Region 1 is the location where northeast winds in southern Idaho drain down the valleys and into the lake. The winds are funneled over the lake and advect out of the lake through regions of the lowest terrain. Region 2 is the location where the moisture that directly affects the airport advects off the lake. This advection of moisture could be caused by numerous meteorological phenomena but have been narrowed to two for this project. The first being the moisture needs a location to advect off the lake as constant wind flow is drained into the lake at region 1. It is determined that the moisture is so shallow that it can only advect through the regions of lowest terrain surrounding the lake. The second possible cause of the advection in this region could be due to a mesoscale feature such as a lake breeze. The moisture could have advected off the lake due to a combination of the both.

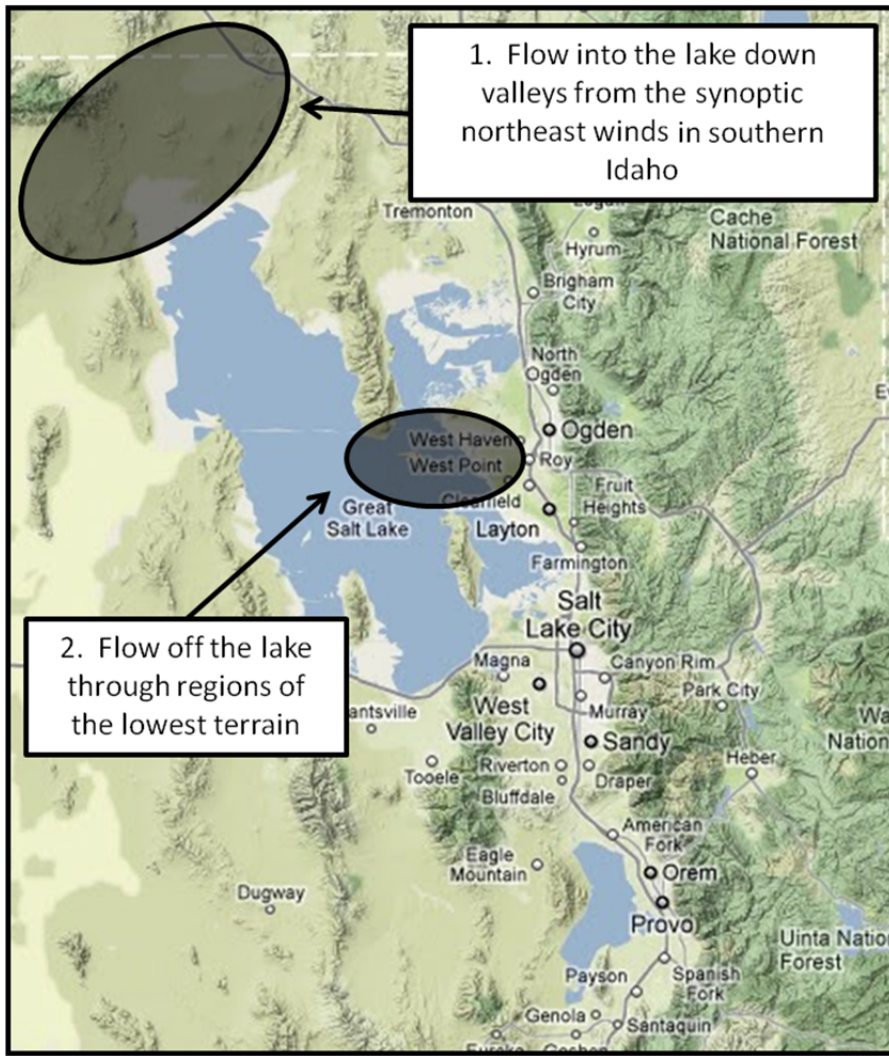


Figure 43. Locations of the strong sensitivities that are considered important in forecasting the amount of moisture received at the SLC International Airport (After Google Maps).

The ESA revealed that changes in the analysis u-component winds in these locations lead to the largest change in forecasted  $Q_v$  at the airport. This information could be used in determining locations for future observations to be used in the data assimilation process. The goal is to place observations where they will reduce forecast metric spread the most which in turn leads to overall reduced forecast error. The Utah MESONET already has a series of surface observations throughout the Salt Lake Basin.

Using the results from the ESA could prove beneficial allowing targeting of observations or observation thinning to be used in the data analysis process which could lead to improved forecasts.

We believe these same methods performed in this project could be used in a domain of complex terrain in southwest Asia. Performing an ESA for a particular region of complex terrain in SW Asia could identify areas of meaningful sensitivities that could be used in future network design. This could help lead to the long term goal of alleviating the uncertainty that goes into forecasting mesoscale features in complex terrain which would lead to more accurate operational forecasts.

## **B. USEFULNESS TO U.S. MILITARY**

Before starting this project, I personally had had little experience and knowledge of forecasting fog in the SLC Basin. This was beneficial because it allowed me to draw conclusions based on the sensitive regions of the forecast that were calculated in the ESA. An ESA performed in a mesoscale environment, especially in areas of complex terrain may be more beneficial to the U.S. military than just targeting observations or for potential observation design.

The U.S. military often operates in areas of complex terrain where both climatology and observation data is sparse or even nonexistent. Providing useful and accurate forecasts becomes difficult without this knowledge. This becomes even more difficult when forecasting certain phenomena like fog in the mountains. Executing a mesoscale ESA for an unknown region of operations may provide background information for the forecaster that could be used to improve operational forecasts. It may lead forecasters to focus their attention on areas where small changes in the analysis lead to large changes in a certain forecasted variables. For example, the results of the ESA from this SLC fog event allow us to draw conclusions on which locations affected the moisture that was advected in the airport the most. A series of mesoscale ESAs could be executed for a particular region to just gain knowledge of how the surrounding terrain

influences the forecast. This knowledge could be incorporated into references that may be used to help forecasters develop more useful and accurate operational forecasts for the military.

### **C. FUTURE WORK**

The results of the ESA using the u-component winds as  $\mathbf{x}$  and  $Q_v$  as  $J$  were a success for this case study. However, there is much that can be done to research and to better understand ensemble sensitivities in a mesoscale environment and how the U.S. military can integrate these results toward improved operations. Listed below are several areas of research that could provide additional insight into mesoscale ESAs and to further address some of the objectives and questions addressed in this project.

1. Using the same ESA methods, determine what other analysis state variables and forecast parameters lead to sensitivities that could be used to help improve fog forecasting in complex terrain. This could include looking harder for larger-scale predictors that may help determine what leads to the development and advection of the fog at longer forecast lengths.
2. Provide further research into testing the statistical linearity of the sensitivities obtained using the same  $\mathbf{x}$  and  $J$ . This would require finding additional case studies in which there was not a significant wind shift between the analysis and the forecast. Due to the constraint set by the wind shift it was determined that using 4 km horizontal grid spacing the linear statistics can be approximated out to 12 hrs. Using a case study without a wind shift would allow proper testing of the linear statistics and potential determination if the sensitivities can be accurately determined beyond 12 hrs.
3. Perform additional tests to further determine the number of ensembles needed to produce useful and robust sensitivities. This may require testing more regions of sensitivities for different case studies and testing at various time lengths. It has been assumed that to achieve the most accurate results would require making new model runs

by rerunning DART with fewer ensembles. This would most likely lead to results that correctly represent the error-covariances in the analyses and thus lead to sensitivities that best represent the new analyses.

4. Perform further sensitivity-analysis prediction tests on additional fog case studies to determine the length that the physical linear assumptions remain valid. Using a fog event without a wind shift between the analysis and the forecast would provide the most ideal linearity results. In addition, apply localization to the covariances in the analysis to determine if the predicted values are more accurate after accounting for sampling error.

5. This case study used synthetic observations in the ensembles. One of the next steps in future studies is to use an ensemble where a realistic network and real observations are used in the data assimilation process.

6. It has been determined that this method could be used in potential network design. A future project could use the same methods performed in this project to a domain in southwest Asia. Performing an ESA for a particular region of complex terrain in SW Asia could lead to useful sensitivities that could be used in future network design or to reduce the uncertainty of forecasting a certain meteorological variable.

## LIST OF REFERENCES

Afghanistan Environment, cited 2012: [Available online at <http://www.globalsecurity.org/military/world/afghanistan/cs-enviro.htm>.]

Ancell, B. and G.J. Hakim, 2007: Comparing adjoint- and ensemble-sensitivity analysis with applications to observation targeting. *Mon. Weather Rev.*, **135**, 4117–4134.

Anderson, J., T. Hoar, K. Raeder, H. Liu, N. Collins, R. Torn, and A. Avellano, 2009: The data assimilation research testbed. *BAMS*, **Sep**, 1283–1296.

Bergreen J., 2009: Fog closes one SLC airport runway. *The Salt Lake Tribune*, 23 January. [Available online at <http://archive.sltrib.com>.]

Dudia, J., 1989: Numerical study of convection observed during the winter monsoon experiment using a mesoscale two-dimensional model. *J. Atmos. Sci.*, **46**, 3077–3107.

Ek, M. B., K. E. Mitchell, Y. Lin, E. Rodgers, P. Grunmann, V. Koren, G. Gayno, and J. D. Tarpley, 2003: Implementation of Noah land surface model advances in the National Centers for Environmental Prediction operational mesoscale H Model. *J. Geophys. Res.*, **108**, 8851–8867.

Errico, R. M., 1997: What is an adjoint model? *American Meteorological Society*, **78**, 2577–2591

Galli, C. 2010: Lake breeze captured during glider flight, cited 2012. [Available online at <http://pcaps2010.blogspot.com/2010/12/lake-breeze-captured-during-glider.html>.]

Garcies, L. and V. Homar. 2009: Ensemble sensitivities of the real atmosphere: application to Mediterranean intense cyclones. *Tellus*, **61A**, 394–406.

Google, cited 2012: Google Maps [Available online at <http://maps.google.com>.]

Hacker, J.P., S.-Y. Ha, C. Snyder, K. Berner, F.A. Eckel, E. Kuchera, M. Pocernich, S. Rugg, J. Schramm, and X. Wang, 2011: The U.S. Air Force Weather Agency's mesoscale ensemble: Scientific description and performance results. *Tellus*, **63A**, 625–641.

Hakim, G. J. and R. D. Torn, 2006: Ensemble synoptic analysis. *Meteorological Monograph*, **33**, 147–162.

Hogan, D., cited 2012: Salt lake valley dense fog initiation study. [Available online at <http://www.wrh.noaa.gov/slc/projects/fogstud/fogstudy.htm>.]

Homan, P.B., 2007: Evaluation of high density surface observations in complex terrain and their contribution to the MM5 model. M.S. thesis, Dept. of Meteorology, Naval Postgraduate School, 79 pp.

Hong, S.-Y., J. Dudhia, and S.-H. Chen, 2004: A revised approach to ice microphysical processes for the bulk parameterization of clouds and precipitation, *Mon. Wea. Rev.*, **132**, 103–120.

Hong, S.-Y., Y. Noh, and J. Dudhia, 2006: A new vertical diffusion package with an explicit treatment of entrainment processes. *Mon Weather Review*, **134**, 2318–2341.

JAAWIN, cited 2012: AFW Ensemble prediction suite (prototype). [Available online <https://weather.afwa.af.mil/jaawin/index.jsp>.]

Kain, J.S., and J.M. Fritsch, 1990: A one-dimensional entraining/detraining plume model and its application in convective parameterization. *J. Atmos. Sci.*, **47**, 2784–2802.

Kalnay, E. 2009: *Atmospheric Modeling, Data Assimilation and Predictability*. 5th ed. Cambridge University Press, 341 pp.

Langland, R.H. and N. L. Baker, 2004: Estimation of observation impact using the NRL atmospheric variational data assimilation adjoint system. *Tellus*, **56A**, 189–201.

Liu, J. and E. Kalnay, 2008: Estimating observation impact without adjoint model in an ensemble Kalman filter. *Q. J. R. Meteorol. Soc.*, **134**, 1327–1335.

MATLAB. 2011: version 7.12.0.635 (2011a). The MathWorks Inc. [Available <http://www.mathworks.com/help/techdoc/>.]

Mlawer, E. J., S. J. Taubman, P. D. Brown, M. J. Iacono, and S. A. Clough, 1997: Radiative transfer for inhomogeneous atmospheres: RRTM, a validated correlated-k model for the longwave. *J. Geophys. Res.*, **102**, 16,663–16,682.

Reinecke, P. A. 2008: Mountain waves and downslope winds: forecasts, predictability, and data assimilation. Ph.D. dissertation, University of Washington, 131 pp.

Skamarock, W.C., J. B. Klemp, J. Dudhia, D. O. Gill, D. M. Barker, M. G. Duda, X. Huang, W. Wang, and J. G. Powers, 2008: A description of the advanced research WRF version 3. *NCAR Tech. Note*, NCAR/TN-475+STR, 113 pp.

Slemmer, J., 2004: Study of dense fog at the Salt Lake City International Airport and its impacts to aviation. *Western Region Technical Attachment*, **04-01**. [Available online at <http://www.wrh.noaa.gov/wrh/04TAs/0401/SLCFog.htm>.]

Torn, R. D., 2010: Ensemble-based sensitivity analysis applied to African easterly waves. *Weather Forecasting*, **25**, 61–78.

\_\_\_\_\_, G. J. Hakim and C. Snyder, 2006: Boundary conditions for limited-area ensemble Kalman filters. *Mon. Wea. Rev.*, **134**, 2490–2502.

\_\_\_\_\_, \_\_\_\_\_, 2008: Ensemble-based sensitivity analysis. *American Meteorological Society*, **Feb**, 663–677.

\_\_\_\_\_, \_\_\_\_\_, 2009: Initial condition sensitivity of Western-Pacific extratropical transitions determined using ensemble-based sensitivity analysis. *Mon. Wea. Rev.*, **137**, 3388-3406.

The Weather Research and Forecasting Model (WRF), cited 2012: WRF Model Users Page. [Available online at <http://wrf-model.org/users/users.php>.]

Zumpre, D. E., and J.D. Horel, 2006: Lake-breeze fronts in the Salt Lake valley. *American Meteorological Society*, **Feb**, 46, 196–211.

THIS PAGE INTENTIONALLY LEFT BLANK

## **INITIAL DISTRIBUTION LIST**

1. Defense Technical Information Center  
Ft. Belvoir, Virginia
2. Dudley Knox Library  
Naval Postgraduate School  
Monterey, California
3. Air Force Weather Technical Library (AFWTL)  
14th Weather Squadron  
Ashville, North Carolina